ABSTRACT

Title of dissertation: RADIO FREQUENCY SUPERCONDUCTING QUANTUM INTERFERENCE DEVICE META-ATOMS AND METAMATERIALS: EXPERIMENT, THEORY AND ANALYSIS

Daimeng Zhang, Doctor of Philosophy, 2016
Department of Electrical and Computer Engineering

Dissertation directed by: Professor Steven M. Anlage
Department of Physics

Metamamterials are 1D, 2D or 3D arrays of artificial atoms. The artificial atoms, called "meta-atoms", can be any component with tailorable electromagnetic properties, such as resonators, LC circuits, nano particles, and so on. By designing the properties of individual meta-atoms and the interaction created by putting them in a lattice, one can create a metamaterial with intriguing properties not found in nature. This thesis examines the meta-atoms based on radio frequency superconducting quantum interference devices (rf-SQUIDs); their tunability with dc magnetic field, rf magnetic field, and temperature are studied. The rf-SQUIDs are superconducting split ring resonators in which the usual capacitance is supplemented with a Josephson junction, which introduces strong nonlinearity in the rf properties. At relatively low rf magnetic field, a magnetic field tunability of the resonant frequency of up to 80 THz/gauss by dc magnetic field is observed, and a total frequency tunability of 100% is achieved.

The macroscopic quantum superconducting metamaterial also shows manipulable self-induced broadband transparency due to a qualitatively novel nonlinear mechanism that is different from conventional electromagnetically induced transparency (EIT) or its classical analogs. A near complete disappearance of resonant absorption under a range of applied rf flux is observed experimentally and explained theoretically. The transparency comes from the intrinsic bi-stability and can be tuned on/ off easily by altering rf and dc magnetic fields, temperature and history. Hysteretic *in situ* 100% tunability of transparency paves the way for auto-cloaking metamaterials, intensity dependent filters, and fast-tunable power limiters. An rf-SQUID metamaterial is shown to have qualitatively the same behavior as a single rf-SQUID with regards to dc flux, rf flux and temperature tuning.

The two-tone response of self-resonant rf-SQUID meta-atoms and metamaterials is then studied here via intermodulation (IM) measurement over a broad range of tone frequencies and tone powers. A sharp onset followed by a surprising strongly suppressed IM region near the resonance is observed. This behavior can be understood employing methods in nonlinear dynamics; the sharp onset, and the gap of IM, are due to sudden state jumps during a beat of the two-tone sum input signal. The theory predicts that the IM can be manipulated with tone power, center frequency, frequency difference between the two tones, and temperature. This quantitative understanding potentially allows for the design of rf-SQUID metamaterials with either very low or very high IM response.

RADIO FREQUENCY SUPERCONDUCTING QUANTUM INTERFERENCE DEVICE META-ATOMS AND METAMATERIALS : EXPERIMENT, THEORY AND ANALYSIS

by

Daimeng Zhang

Dissertation submitted to the Faculty of the Graduate School of the
University of Maryland, College Park in partial fulfillment
of the requirements for the degree of
Doctor of Philosophy
2016

Advisory Committee:
Professor Steven Anlage, Chair/Advisor
Professor Thomas Antonsen
Professor Thomas Murphy
Professor Jeremy Munday
Professor Christopher Lobb

Acknowledgments

I'd like to thank my advisor Steven Anlage for always being supportive and encouraging along the way. I benefit from him not only the step-by-step guidance on research, but also many things I treasure in life, including the time-management skills, the optimistic attitudes towards obstacles, and the kindness to people. I can feel my progress in every aspect under the influence of my advisor.

I would also like to express my gratitude to my committee members, Thomas Antonsen, Thomas Murphy, Jeremy Munday and Christopher Lobb, for their time, interest, and suggestions for my thesis.

I want to thank my labmate Melissa Trepanier. We worked closely on this project and made a lot of progress together. I am very lucky to have been collaborating with this talented girl.

I definitely also appreciate the support and help from my other labmates, Tamin Tai, Jen-Hao Yeh, John Abrahams, Stephen Remillard, Bo Xiao, Bakhrom Oripov, Seokjin Bae, Yuewen Tan, Ziyuan Fu, Min Zhou, Rahul Gogna, Biniyam Taddese, and Benhood Ghamsari. They create an harmonic and fun working environment so I always enjoy staying in the lab.

Our collaborators play important roles in this work. I would like to thank Oleg Mukhanov, Masoud Radparvar and Georgy Prokopenko in Hypres Inc. for their help with fabricating the samples, and stimulating ideas of potential applications; Thomas Antonsen and Edward Ott at University of Maryland for helpful discussions on the nonlinear dynamics techniques used in our project; Alexey Ustinov,

Philipp Jung, and Suzanne Butz at Karlsruhe Institute of Technology for sharing ideas with me on the improvement of experiment and simulation; Alexander Zhuravel at National Academy of Sciences of Ukraine for the laser scanning microscope measurements; Kaveh Delfanazari, Vassili Savinov, and Nikolay Zheludev at University of Southampton for help with the mm-wave experiment conducted there; Rangga Budoyo, Cody Ballar, and Frederick Wellstood for use of their extreme low temperature setups; Nikos Lazarides and George Tsironis at University of Crete for discussions on theoretical works; H. J. Paik and M. V. Moody for use of the pulsed tube refrigerator.

I want to also thank my friends for making my years at University of Maryland so interesting and colorful. Thank my family, especially my parents for caring about me far from a distance in China, and giving me useful advice at every stage in my life. Thank my boyfriend for taking great care of me and standing by my side all the time. Thank all the staff members in Physics Department, Electrical and Computer Engineering Department, and the Center for Nanophysics and Advanced Materials (CNAM).

This work is supported by the NSF-GOALI and OISE programs through grant #ECCS-1158644, and the Center for Nanophysics and Advanced Materials (CNAM). I thank them for funding this project so I have the chance to work on this wonderful topic, and with great people.

Table of Contents

Chapter 1: Introduction

1.1 Metamaterials and Superconducting Metamaterials

Metamaterials are artificially structured media that are designed to have unique electromagnetic properties which are not ordinarily found in nature. Metamaterials are composed of 1D, 2D, or 3D arrangements of artificial atoms the same way the natural materials are composed of atoms. Those artificial atoms, also known as meta-atoms, can be any element that has tailorable electromagnetic properties. The most common meta-atoms are resonators, LC circuits, nano-particles and so on. A schematic of a 2D metamaterial is shown in Fig. 1.1.

When the electromagnetic waves of a wavelength λ shine on the metamaterial with a lattice constant a, and $\lambda \gg a$, the waves see the metamaterial as a single effective medium instead of discrete elements. The electromagnetic properties of a metamaterial arise from both the structure of individual meta-atoms and the interactions between these elements, resulting in interesting collective behavior.

One of the most intriguing properties of a metamaterial is the capability of negative index of refraction $n < 0$ [1] [2] [3]. It requires the metamaterial having both a negative permeability μ and a negative permittivity ϵ. Natural materials such as some ferrites reveal a negative permeability when responding to magnetic

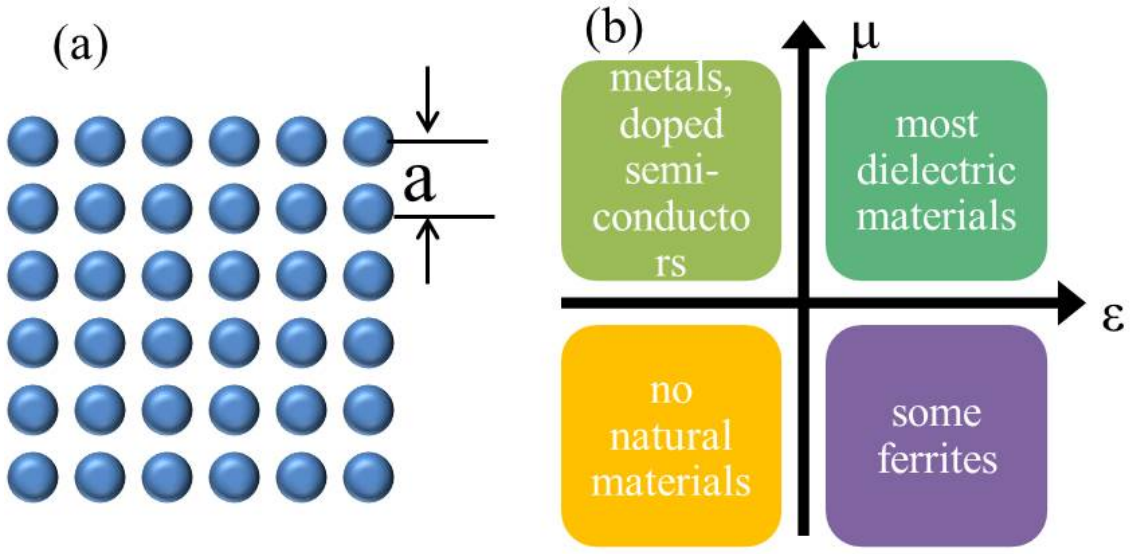

Figure 1.1: (a) An example of a 2D metamaterial made of meta-atoms (blue circles) with a lattice constant a. (b) Materials with different values of permeability μ and permittivity ϵ.

field. Metals respond to the external electric fields with a negative permittivity below their plasma frequency. However, a material with both negative permeability and permittivity is not found in nature.

A metamaterial with a negative refraction index can enable many novel applications. A straightforward consequence of the negative refraction index is a negative refraction angle for a light ray propagating through a planar interface between positive and negative index media. As a light ray injects from a n_1 ($n_1 > 0$) medium to a n_2 medium with incidence angle θ_1 ($0° < \theta_1 < 90°$), the refraction angle θ_2 satisfies (Fig. 1.2 (a)) :

$$\frac{\sin\theta_1}{\sin\theta_2} = \frac{n_2}{n_1}$$

according to Snell's Law. If $n_2 < 0$, the refraction angle θ_2 is also negative, and the

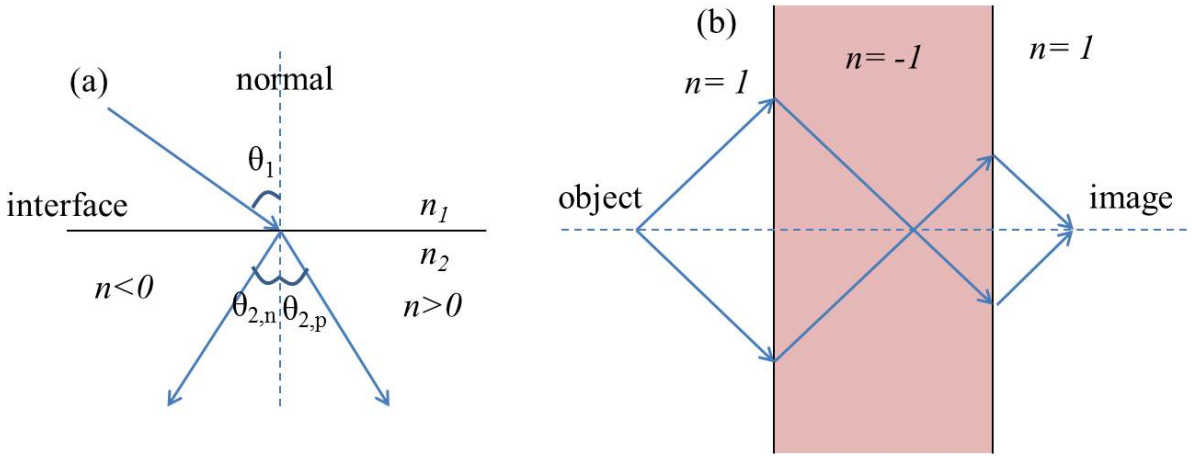

Figure 1.2: (a) The refraction at the interface between two media. The incident light ray is in a medium of positive refraction index. (b) A flat lens built with a medium with a refraction index of $n = -1$.

light ray bends backward after the interface, as plotted in Fig. 1.2. One can build a flat lens utilizing the negative index property, especially if $n_2 = -n_1$, as shown in Fig. 1.2. All light rays from the object on one side can be focused and imaged at the other side of the flat lens.

The refraction index is of a material is

$$n = \sqrt{\mu_r \epsilon_r}$$

where μ_r and ϵ_r are the relative permeability and permittivity, respectively. The permeability and the permittivity are usually complex numbers because of the loss in a material. We can write $\mu_r = |\mu_r| e^{\alpha_1}$, $\epsilon_r = |\epsilon_r| e^{\alpha_2}$ as complex numbers ($0° < \alpha_1, \alpha_2 < 180°$), and the refraction index becomes

$$n = \sqrt{|\mu_r \epsilon_r|} e^{(\alpha_1 + \alpha_2)/2}.$$

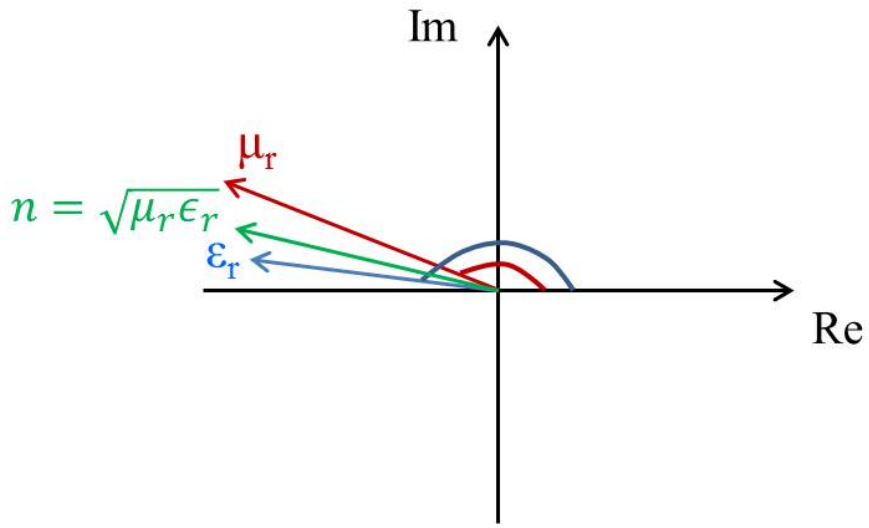

Figure 1.3: The relative permeability μ_r (red), the relative permittivity ϵ_r (blue), and the corresponding refraction index n (green) in the complex plane.

This relationship is plotted in the complex plane in Fig. 1.3. In order to get a negative real part of the refraction index, the real parts of μ_r and ϵ_r must be negative at the same time. An attractive case is a metamaterial with a refraction index $n = -1$ for the lowest reflection at the interface of the metamaterial and air.

A metamaterial which couples to magnetic field in an eletromagnetic wave is usually called a magnetic metamaterial, while an electric metamaterial mainly interacts with the electric field. One approach to achieve negative refraction index is to combine a magnetic metamaterial with a negative permeability and an electric metamaterial with a negative permittivity.

A common form of a magnetic meta-atom is a conducting loop resonator, which is diamagnetic according to Lenz's law. The real part of the effective relative

permeability of a metamaterial made with magnetic meta-atom can be written as

$$\mu_r = 1 - \frac{F\omega^2}{\omega^2 - \omega_0^2}$$

where F is the filling factor of the meta-atoms inside the effective medium, ω is the drive frequency of the magnetic field, and ω_0 is the resonant frequency. This implies that as the drive frequency approaches the resonant frequency, the effective permeability can become negative. A well-studied magnetic meta-atom is a split-ring resonator (SRR), where the inductance and the capacitance come from the loop and the gap, respectively.

The effective relative permittivity of a metallic medium is related to its plasma frequency ω_p

$$\epsilon_r = 1 - \frac{\omega_p^2}{\omega^2}$$

where ω denotes the frequency of the electric field. Metals naturally have a negative permittivity even in the visible because their plasma frequency is usually in the ultraviolet frequency range, much higher than microwaves and visible light. Since the ultra-violet plasma frequency is much higher than a typical drive frequency, the metals generally have a very large negative permittivity.

The idea of an engineered electric metamaterial aims at bringing down the plasma frequency to achieve a negative permittivity with a magnitude around unity at the frequency of interest. One way is to build a sub-wavelength metal-wire array, which effectively decreases the electron concentration in the medium thus

contributing to a lower plasma frequency [4].

A negative refraction index metamaterial has been realized experimentally by combining a SRR metamaterial with a metal-wire metamaterial [3]. The resonant frequency of the SRR meta-atoms and the plasma frequency of the metal-wire metamaterial are designed to be at around the same frequency in the microwave frequency range.

Other than the negative refraction index, a wide variety of properties and applications have been pursued using metamaterials, including super-resolution imaging [5] [6], cloaking [7] [8], transformation optics [9] [10], and perfect absorption [11].

Many traditional metamaterials work only in a narrow range of frequencies. The properties cannot be modified after the metamaterial has been fabricated. It is therefore desirable to make them tunable and reconfigurable even after fabrication [12]. Being able to tune the electromagnetic response over a wide range, and on short time scales, is highly desirable for applications such as software-defined radio [13], tunable antennas [14], and filters for digital rf receivers [15].

Adding nonlinear elements, such as diodes [16], into metamaterials facilitates tunability, design flexibility, and self-induced nonlinear responses [14, 17], giving rise to developments in metamaterial-based amplifiers [18, 19] , filters [20–22] and antennas [23–25]. However, loss also arises from those nonlinear components.

Low attenuation is required for a metamaterial as the electromagnetic waves pass through it. Even small amounts of loss suppresses features such as evanescent wave amplification [26] and negative refraction [26–31]. For example, the enhanced loss in metamaterials approaching the plasmonic limit has imposed a se-

vere limitation on visible-wavelength metamaterials composed of noble metal meta-atoms [32–35].

Another issue with many metamaterials is that the meta-atom sizes often approach the scale of the wavelength to minimize losses [24, 36]. A consequence is that the electromagnetic properties of the collection of meta-atoms cannot be interpreted as those of an effective medium. This has been an issue both in the visible and in the microwave regime.

Superconducting metamaterials are low-loss, even when the meta-atoms are built with very small size, thus solving the attenuation problem while staying in the sub-wavelength regime [14,37,38]. Moreover, superconducting metamaterials are intrinsically nonlinear and tunable [14, 37, 38]. Many temperature tunable properties in superconducting metamaterials have been explored based on the temperature dependence of the superfluid density and thus the kinetic inductance [39–45]. However, temperature tuning is generally too slow (on the scale of 10μs [46]) for a real-time applications, due to large thermal inertia of the superconducting meta-atoms.

Superconducting metamaterials can be tuned by magnetic fields in a much shorter time scale. Both dc and rf magnetic fields have been employed to tune the properties of superconducting SRRs [47, 48], mainly through enhancing the inductance either by the additional magnetic flux in the thin-film superconductors [47], or by increased rf currents in the SRRs [47,49–53]. High rf power is also found to introduce switchable electromagnetically-induced transparency behavior in a superconducting resonator [45]. However, the insertion of magnetic flux is often accompanied by additional dissipation. The tuning range is also limited.

The introduction of Josephson junction into superconducting meta-atoms offers high speed, low dissipation and large tunability. Metamaterials employing the Josephson effect will be discussed in the next section.

1.2 Superconducting Meta-Atoms Employing the Josephson Effect

The superconducting electrons in a superconductor can be described by a macroscopic phase-coherent complex quantum pseudowave-function Ψ. The local density of superconducting electrons n_s is related to $\Psi = \sqrt{n_s}e^{i\theta}$ where θ denotes the time and position-dependent phase of the wavefunction [54,55]. The phase coherence of this wavefunction results from the underlying microscopic BCS (Bardeen, Cooper, Schrieffer) wavefunction describing the Cooper pairing of all electrons in the metal.

A Josephson junction is two superconductors connected by a weak link, often a very thin insulating barrier (Fig. 1.4), such that the Cooper pairs described by the wavefunction can tunnel through the barrier [56] [54]. The current I through the junction, and the voltage V across the junction, both depend on the gauge-invariant phase difference $\delta(t)$ between the macroscopic quantun wavefunctions $|\Psi_1|e^{i\theta_1}$ and $|\Psi_2|e^{i\theta_2}$ of the two superconductors

$$\delta(t) = \theta_1(t) - \theta_2(t) - \frac{2\pi}{\Phi_0}\int_1^2 \vec{A}(\vec{r},t)\cdot d\vec{l}, \tag{1.1}$$

where $\vec{A}(\vec{r},t)$ is the magnetic vector potential, $\Phi_0 = \frac{h}{2e} \cong 2.07 \times 10^{-15}$ Tm^2 is the flux quantum (h is Planck's constant and e is the electronic charge). The integral is from superconductor 1 to superconductor 2.

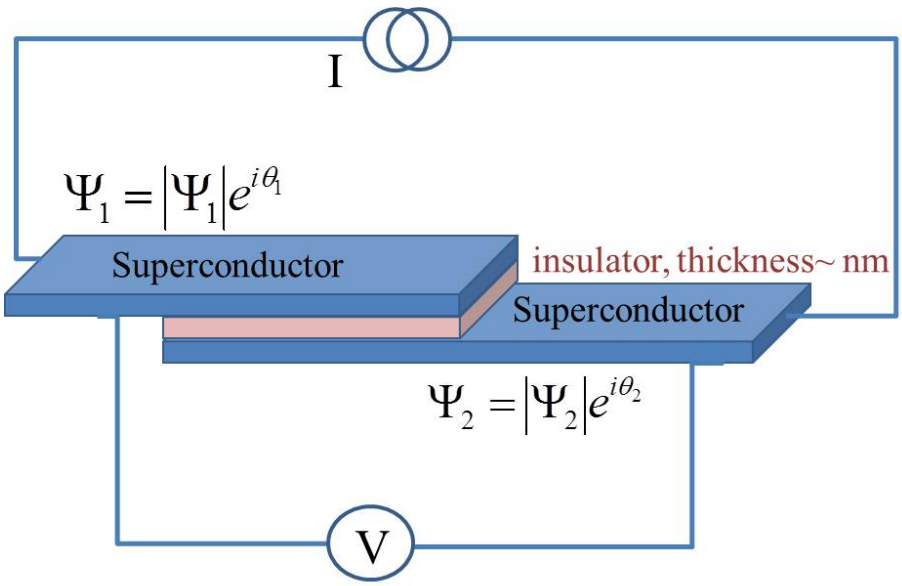

Figure 1.4: The schematic of a Josephson junction, a thin layer of insulator sandwiched between two superconductors.

The gauge-invariant phase difference $\delta(t)$ causes a dc superconducting current I through the junction even in the absence of a dc voltage, according to the dc Josephson effect,

$$I = I_c \sin \delta(t), \tag{1.2}$$

where I_c is the critical current - the maximum superconducting current a Josephson junction can support. The critical current depends on the area of the junction, as well as the critical current density which increases as the temperature reduces [54].

When the gauge-invariant phase δ varies with time, the variation gives rise to a voltage V across the junction (the ac Josephson effect):

$$\frac{d\delta}{dt} = \frac{2\pi}{\Phi_0} V, \tag{1.3}$$

The voltage further causes an ac superconducting current in the tunneling barrier.

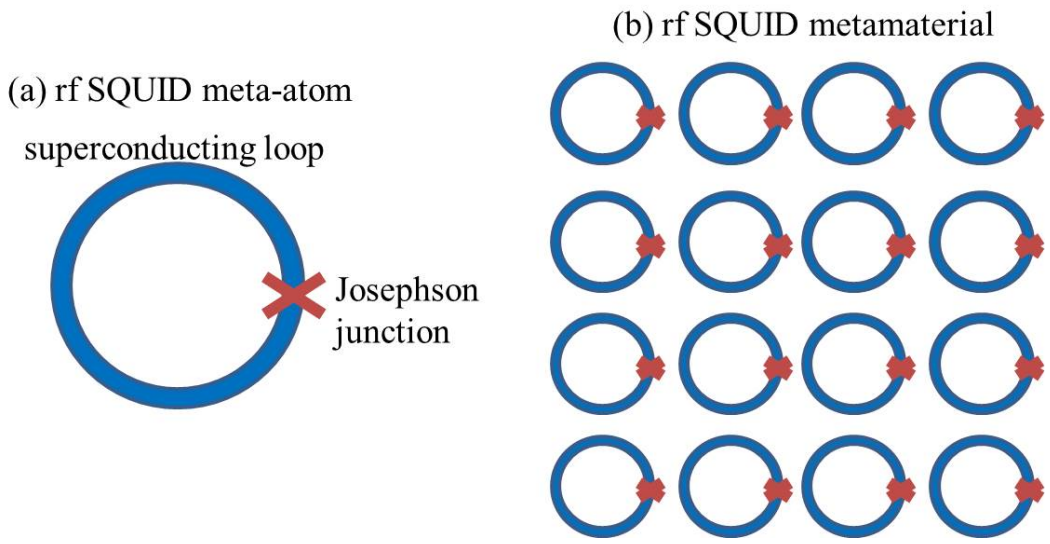

Figure 1.5: Schematic of (a) a single rf-SQUID meta-atom, and (b) a 2D rf-SQUID metamaterial made of identical rf-SQUID meta-atoms.

The dynamics and properties of a metamaterial incorporating Josephson junctions can thus be modulated by the gauge-invariant phase difference δ across the junction [55] according to Eqs. (1.2) and (1.3).

In this thesis I will focus on tuning the gauge-invariance phase difference δ using the dc and rf magnetic fields in a magnetic meta-atom made of a single Josephson junction interfered with a superconducting loop (Fig. 1.5 (a)), commonly known as a radio-frequency Superconducting QUantum Interference Device (rf-SQUID). A 2D metamaterial composed of identical rf-SQUID meta-atoms is shown in Fig. 1.5 (b). The meta-atoms combine fluxoid quantization and Josephson effects, thus are highly tunable and nonlinear.

The fluxoid quantization effect in a superconducting ring comes directly from the phase factor of the macroscopic wavefunction $\Psi = |\Psi|e^{i\theta}$ describing the superconductor. The single-valueness of Ψ requires that the phase difference $\Delta\theta = 2n\pi$

(n is an integer) after going around a ring and return to the same location on any path. This quantization condition requires that the fluxnoid Φ' in a superconducting loop is also quantized as $n\Phi_0$. The total flux Φ in the superconducting loop is equal to the fluxnoid Φ' if the ring thickness is larger than the penetration depth of the superconductor. Thus, the total magnetic flux in the superconducting loop is limited to $\Phi = n\Phi_0$ where n is an integer.

In an rf-SQUID, the closed superconducting loop is interfered with a Josephson junction, and the flux quantization condition becomes [54]

$$\Phi/\Phi_0 = \delta/(2\pi) + n. \tag{1.4}$$

Equation (1.4), plus Eqs. (1.2) and (1.3) suggest that the voltage across the junction, and the current through the junction can by dramatically modulated by the magnetic flux, and the response is nonlinear, and on the scale of $\Phi_0 = 2.07 \times 10^{-15}$ Tm^2. Extremely small magnetic flux is capable of tuning the properties of an rf-SQUID meta-atom.

Rf-SQUID metamaterials combine the advantages of superconducting electronics and nonlinear metamaterials [14, 37, 38]. An rf-SQUID is the macroscopic quantum version of a split ring resonator (SRR) with the gap capacitance in the SRR replaced by a nonlinear Josephson junction. Basically, an rf-SQUID is a nonlinear resonator with a manipulable resonant frequency and absorption that depend on the dc and rf flux amplitudes, the temperature, and the drive signal history. The properties of rf-SQUID metamaterials have been studied intensively [14, 37, 38, 57–59],

including the dc magnetic flux tunable resonant frequency [60–62], rf magnetic flux tunable resonance strength [63, 64], and nonlinear dynamics in coupled rf-SQUID meta-atoms [65–69].

Note that we are in the limit where the lattice constant a is much less than the input wavelength ($\lambda/a \approx 80$) such that the electro-magnetic wave sees the whole metamaterial as an effective medium, as opposed to the other limit for photonic crystals where the size and the lattice constant of the elements in an array are comparable to the wavelength, giving rise to band-gap structures depending on the periodicity and shape of the lattice.

Previous work reveals that rf-SQUID meta-atoms and metamaterials have a resonant frequency tunability of up to 80THz/gauss by varying the dc magnetic flux when the driving rf flux amplitude is low [60–62]. I studied the bistability of rf-SQUID meta-atoms and metamaterials driven by intermediate rf flux amplitudes. The bistability results in a lower resonant frequency and a nearly full disappearance of resonant absorption (transparency). Such broadband transparency can be switched on and off via drive frequency, signal amplitude, or dc flux hysteresis [64]. These properties offer a range of previously unattainable functionalities because the rf-SQUID acts effectively as a three-terminal device. New applications include filters and wide-band power limiters for direct-digitizing rf receivers [70], gain-modulated antennas [71], rf pulse shaping for qubit manipulation, and tunable intensity-limiting filters.

As data streams containing multi-frequency signals pass through these nonlinear components, they may generate intermodulation (IM) products via frequency

mixing [72]. The same issue appears in intrinsically nonlinear superconducting electronics. The IM between two input frequencies f_1 and f_2 leads to products at frequencies $pf_1 \pm qf_2$ (p and q are integers), forming side bands and additional noise that could diminish the performance of superconducting devices [73–85]. On the other hand, IM generation can be used as a diagnostic to determine various types of defects in superconductors [86–89], to study unconventional superconductors [86,87,89–98], and to amplify microwave signals [85,99,100], even at the quantum limit in Josephson parametric amplifiers [101,102] and Josephson metamaterials [18]. Therefore, IM is of research interest in wireless communication, nonlinear metamaterials, as well as in superconducting electronics/materials and quantum information processing. Extensive measurement and theory have been devoted to IM in these fields [75,83,103–111]. The IM response of rf-SQUID meta-atoms and metamaterial will thus be studied in this thesis.

In the following parts of the thesis, a detailed model of rf-SQUID meta-atoms and metamaterials will be discussed (Chap. 2), followed by a description of our experimental setup and the designs of the rf-SQUID metamaterials in Chap. 3. Experimental results and nonlinear simulation results on the transmission and tunable resonance of the SQUID meta-atoms (metamaterials) will be presented in Chap. 4. In Chap. 5, several analytical models are used to explain the experimental and simulation phenomena. Chapter 6 focuses on the two-tone excitation of rf-SQUID meta-atoms and metamaterials. A two time-scale analysis is used to understand the unique two-tone response observed in experiment. Finally, a summary and some future works are presented in Chap. 7.

Chapter 2: Modeling of rf-SQUIDs

Radio Frequency SQUIDs are the macroscopic quantum version of the commonly employed Split Ring Resonator (SRRs) in the metamaterial community in that the gap capacitor in the SRR is replaced with a nonlinear Josephson junction (JJ).

The Josephson junction enables various applications in superconducting circuits as well as quantum computing using superconducting qubits. The uniqueness of the JJ comes from the macroscopic quantum gauge-invariant phase difference across the junction δ, which determines the current through the junction $I = I_c \sin\delta$. Moreover the time-dependence of the phase difference is related to the voltage over the junction $V = (\hbar/2e)d\delta/dt$. I_c is the critical current (maximum current that can flow through the junction in the zero-resistance state) of the junction, which is determined by the area and quality of the junction. $\hbar$ is the Planck's constant divided by 2π. We model an rf-SQUID as a Resistively and Capacitively Shunted Josephson Junction (RCSJ-model) coupled to the superconducting loop inductance (see Fig. 2.1).

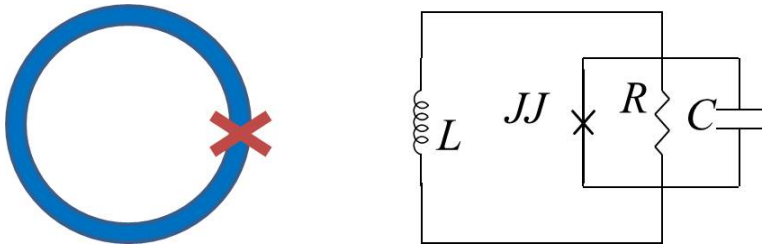

Figure 2.1: Circuit diagram of the rf-SQUID modeled as an RCSJ coupled to loop inductance L.

In an rf-SQUID, δ is related to the total magnetic flux via

$$\delta = 2\pi\Phi_{tot}/\Phi_0 + 2n\pi, \tag{2.1}$$

where n is an integer, $\Phi_0 = 2.07 \times 10^{-15}$ Tm^2 is the quantum magnetic flux. The voltage across the junction results from a change in the magnetic flux Φ_{tot}, and can be written as

$$V = \frac{\Phi_0}{2\pi}\frac{d\delta}{dt}.$$

Here we can take n to be 0 without loss of generality as shifting δ by 2π leaves the current I and the voltage V unchanged [56].

The total magnetic flux through the loop Φ_{tot} is determined by the applied flux,

$$\Phi_{tot} = \Phi_a - LI.$$

Here Φ_a is the applied magnetic flux, I is the total current through the loop, which flows through the parallel combination of the junction, shunt resistance R and capacitance C in the RCSJ model. One can rewrite this relation in terms of phases,

and obtain the dimensionless equation

$$\delta = \phi_a - \frac{2\pi LI}{\Phi_0} = \phi_a - \beta_{rf} I/I_c, \tag{2.2}$$

where $\phi_a = 2\pi\Phi_a/\Phi_0$ is the dimensionless applied flux, usually made up of a dc flux ϕ_{dc} and an rf flux ϕ_{rf}. The quantity $\beta_{rf} = 2\pi LI_c/\Phi_0$ determines the relationship between the applied flux and the Josephson phase. Note here that some researchers employ the notation β_L instead of β_{rf}. Another quantity $\beta = \beta_{rf}/2\pi$ is also frequently used in works related to SQUIDs.

2.1 Small RF Flux Approximation

When the applied rf flux ϕ_{rf} is extremely small, the time dependent part of δ should oscillate very weakly, *i.e.*, $d\delta/dt \to 0$. Several approximations can be made to simplify the model.

2.1.1 Effective Josephson Inductance

If the driving rf flux is very small, we can define an effective inductance for the Josephson junction by requiring $V = L_{JJ} dI/dt$ [56], with

$$L_{JJ} = \frac{\Phi_0}{2\pi I_c \cos\delta}. \tag{2.3}$$

We get a nonlinear inductance which is inversely related to $\cos\delta$ where $\Phi_0 = h/2e = 2.068 \times 10^{-15}$ Wb is the magnetic flux quantum, a combination of fundamental

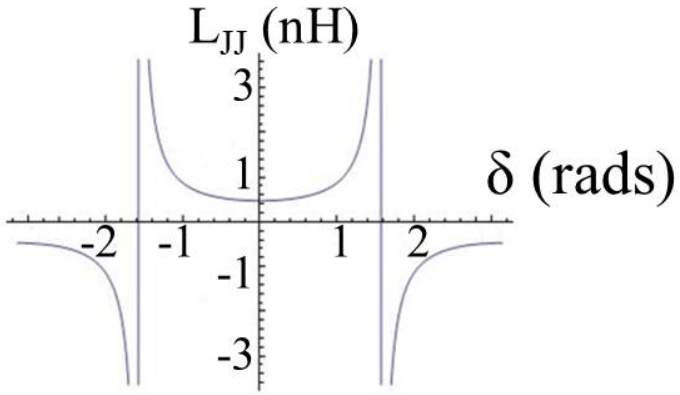

Figure 2.2: The Josephson inductance L_{JJ} as a function of the gauge invariant phase δ. The critical current I_c here is taken as 0.8 μA, a typical value in our SQUID design.

physical constants: the Planck constant h and the electron charge e. Note that the quantity $\beta_{rf} = 2\pi LI_c/\Phi_0 = L/|L_{JJ}|_{min}$ introduced earlier in Eq. 2.2 is also the ratio of the loop inductance L to the minimum absolute value of the Josephson inductance in the SQUID.

Figure 2.2 is a plot of L_{JJ} versus δ according to Eq. 2.3. The inductance is tuned by δ through both positive and negative values: $L_{JJ} \leq -\Phi_0/(2\pi I_c)$ or $L_{JJ} \geq \Phi_0/(2\pi I_c)$. Once the gauge-invariant phase δ across the junction is modulated, the self-resonant frequency of an rf-SQUID would be tuned through L_{JJ} according to equation (2.4).

The resonant frequency of the lumped RLC circuit for an rf-SQUID is written as

$$f_0 = \frac{1}{2\pi\sqrt{\left(\frac{1}{L} + \frac{1}{L_{JJ}}\right)^{-1} C}}, \tag{2.4}$$

2.1.2 Stationary State

When $\phi_{rf} \to 0$ and $d\delta/dt \to 0$, the SQUID is in a stationary state. The applied flux is equal to the dc flux, and the current through the junction just $I = I_c \sin\delta$. Equation (2.2) becomes

$$\delta = \phi_{dc} - \beta_{rf} \sin\delta. \tag{2.5}$$

The $\sin\delta$ nonlinearity brings in interesting behavior for solutions of Eq. (2.5). In particular, the question of whether the $\delta - \phi_{dc}$ function is single-valued or multi-valued depends on the value of β_{rf}. The critical value is $\beta_{rf} = 1$. Figure 2.3 shows the solution to Eq. (2.5) as the β_{rf} is below (red curve), equal (black curve), and above unity (blue curve).

If $\beta_{rf} < 1$, the function is single-valued: For one dc flux value there is only one stable solution for δ. Note also that all the curves for $\beta_{rf} < 1$ have crossings at dc flux Φ_{dc} at integer numbers and half integer numbers of quantum flux. At these crossings $\delta = \phi_{dc} = m\pi/2$ and m is an integer.

For β_{rf} above unity however, each dc flux value corresponds to multiple possible solutions for δ; some of the solutions are not stable (dashed segments of the blue line in Fig. 2.3). The value of δ under certain dc flux is hysteretic, depending on the history and the scanning direction of dc magnetic field. The hysteresis in dc flux may introduce chaotic behavior in SQUIDs when the rf flux amplitude is not negligible [112]. So in our work we design our SQUIDs to be non-hysteretic in terms of the dc flux, i.e., $\beta_{rf} < 1$.

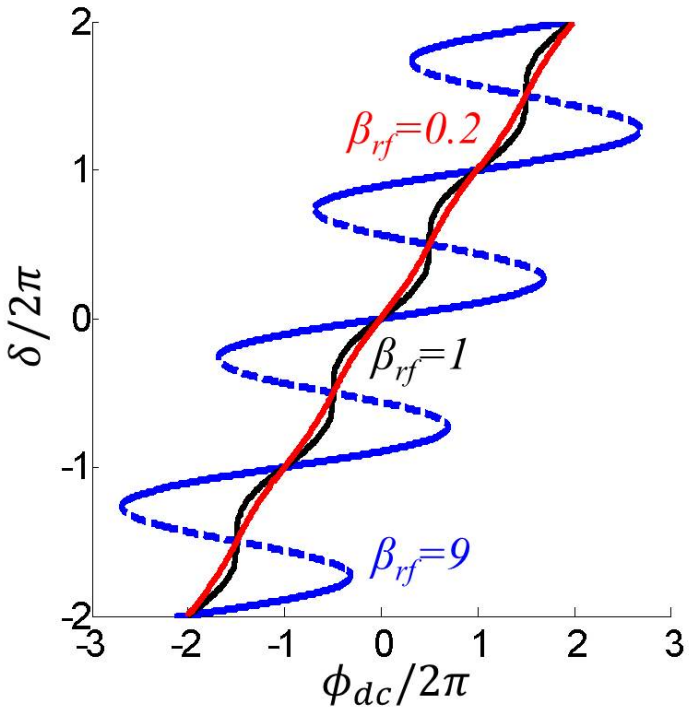

Figure 2.3: The relationship between δ and ϕ_{dc} when β_{rf} is 0.2 (red curve), 1.0 (black curve), and 9.0 (blue curve).

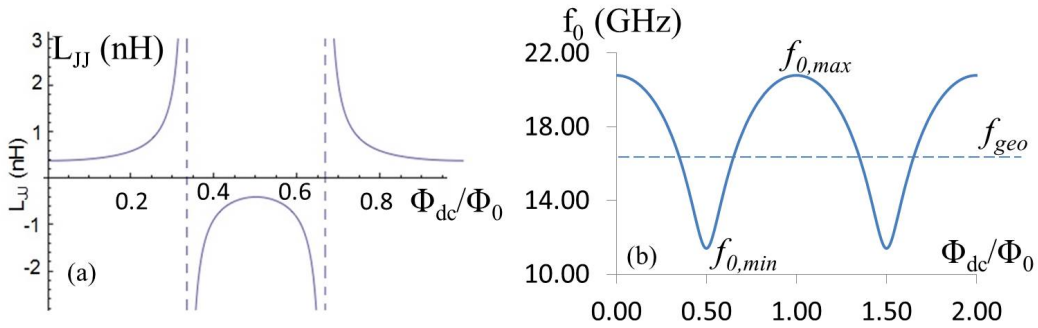

Figure 2.4: (a) The Josephson inductance L_{JJ} as a function of dc flux. (b) The resonant frequency of an rf-SQUID when the junction is modeled using the simple RSCJ model and the Josephson junction is modeled as a tunable inductance. The critical current I_c is 0.8 μA, $\beta_{rf} = 0.6$, inductance $L = 0.24$ nH, geometrical resonant frequency $f_{geo} = 16.6$ GHz, and capacitance $C = 0.4$ pF.

Remember that $L_{JJ} = \Phi_0/(2\pi I_c \cos\delta)$ 2.3. From the above discussions of Eq. (2.5) for $\beta_{rf} < 1$, we achieve the following conclusions: when $\phi_{dc}/2\pi = 0, \pm1, \pm2, ...$, $\cos\delta = 1$ and $L_{JJ} = \Phi_0/(2\pi I_c)$; as $\phi_{dc}/2\pi = \pm1/2, \pm3/2, ...$, $\cos\delta = -1$ and $L_{JJ} = -\Phi_0/(2\pi I_c)$. We plot L_{JJ} for a junction embedded in an rf-SQUID as a function of perpendicular dc flux in Fig. 2.4 (a).

The self-resonant frequency of an rf-SQUID incorporating the JJ will then be tuned with dc flux, as shown in Fig. 2.4 (b). We write the tunable resonant frequency of the rf-SQUID f_0 in terms of the geometrical resonant frequency $f_{geo} = 1/(2\pi\sqrt{LC})$,

$$f_0 = \frac{1}{2\pi\sqrt{\left(\frac{1}{L} + \frac{1}{L_{JJ}}\right)^{-1} C}} = f_{geo}\sqrt{1 + \frac{L}{L_{JJ}}}.$$

At zero dc flux, L/L_{JJ}=$2\pi LI_c/\Phi_0 = \beta_{rf}$; the resonant frequency has the maximum value $f_{0,max}$. At $\Phi_{dc}/\Phi_0 = \phi_{dc}/2\pi = 1/2$, the ratio L/L_{JJ}=$-2\pi LI_c/\Phi_0 = -\beta_{rf}$; the resonant frequency is at minimum $f_{0,min}$. The resonant frequency is periodic with dc flux Φ_{dc} with a periodicity of Φ_0.

$$f_{0,max} = f_{geo}\sqrt{1+\beta_{rf}} \tag{2.6}$$

$$f_{0,min} = f_{geo}\sqrt{1-\beta_{rf}} \tag{2.7}$$

To get maximum tunability, we usually design our SQUID samples to have a near unity value of β_{rf}. The theoretically predicted minimum resonant frequency is thus close to DC, out of our microwave measurement frequency range because our measurements are performed inside a single-conductor waveguide with a finite non-zero cutoff frequency. In the experiment we measure $f_{0,max}$ as well as f_{geo}; this is how we estimate the quantity β_{rf} for our SQUID, and compare with the nominal design value.

2.2 Full Nonlinear Numerical Calculation

Next we consider the most general case where the applied magnetic flux Φ_a is composed of a dc flux Φ_{dc} and an rf flux $\Phi_{rf,a}(t)$. Here we assume the rf flux is in the form of $\Phi_{rf,a}(t) = \Phi_{rf}\sin\omega t$ where ω is the driving frequency and Φ_{rf} is the amplitude of the rf magnetic flux. The current I in the loop flows through the junction, the shunt resistance R and the capacitance C in the RCSJ model (see Fig. 2.1): $I = I_c\sin\delta + V/R + CdV/dt$. We replace these terms in Eq. (2.1), and obtain:

$$\Phi_{tot} = \Phi_{dc} + \Phi_{rf}\sin\omega t - L(I_c\sin\delta + \frac{V}{R} + C\frac{dV}{dt}) \tag{2.8}$$

Substituting Φ_{tot} with $\Phi_0\delta/2\pi$ and V with $(\hbar/2e)d\delta/dt$ into equation (2.8) and rearranging terms, we arrive at the dimensionless equation:

$$\frac{d^2\delta}{d\tau^2} + \frac{1}{Q}\frac{d\delta}{d\tau} + \delta + \beta_{rf}\sin\delta = (\phi_{dc} + \phi_{rf}\sin\Omega\tau) \tag{2.9}$$

where $\phi_{dc} = 2\pi\Phi_{dc}/\Phi_0$ and $\phi_{rf} = 2\pi\Phi_{rf}/\Phi_0$ are the applied dimensionless dc flux and rf flux, $\omega_{geo} = 2\pi f_{geo} = 1/\sqrt{LC}$ is the geometrical frequency, $\Omega = \omega/\omega_{geo}$, $\tau = \omega_{geo}t$, $Q = R\sqrt{C/L}$ is the quality factor of the SQUID that reflects the dissipation, and $\beta_{rf} = 2\pi LI_c/\Phi_0$ is the coefficient determining the degree of nonlinearity and tunability in an rf-SQUID.

An array of N coupled rf-SQUIDs can be described as a system of coupled nonlinear differential equations [113]:

$$\hat{\delta} + \bar{\bar{\lambda}}(\frac{d^2\hat{\delta}}{d\tau^2} + \frac{1}{Q}\frac{d\hat{\delta}}{d\tau} + \hat{\delta} + \beta_{rf}\sin\hat{\delta}) = \hat{\phi}_{dc} + \hat{\phi}_{rf}\sin\Omega\tau \tag{2.10}$$

where $\hat{\delta}$ is an N-element vector describing the gauge-invariant phases of the N rf-SQUIDs, $\hat{\phi}_{dc}$ and $\hat{\phi}_{rf}$ are N-element vectors denoting the non-dimensional dc flux and rf flux applied to each rf-SQUID respectively, $\bar{\bar{\lambda}}$ is an $N \times N$ coupling matrix determining the interactions between the meta-atoms [113]. More details of the array behavior can be found in my colleague's work [113]. In this work we mainly consider the weakly coupled and uniformly driven SQUID array, which can be modeled as a single Josephson junction RCSJ model.

We solve equation (2.9) (or equation (2.10) for an array) numerically to deter-

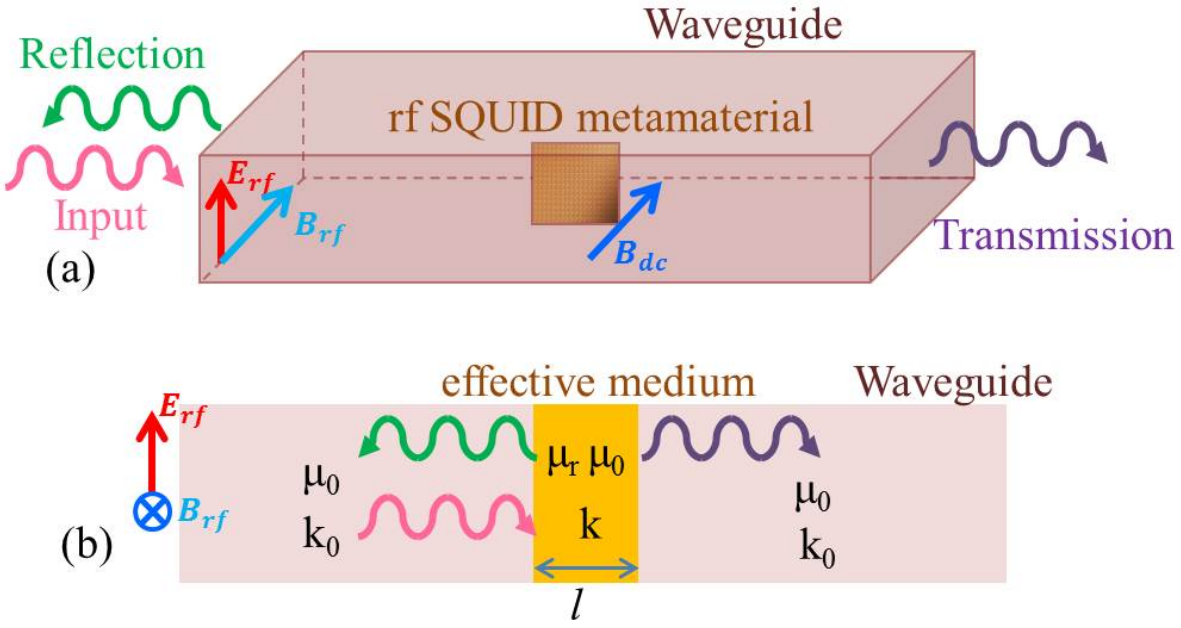

Figure 2.5: (a) Schematic for measuring the transmission of the SQUID meta-atoms and metamaterials inside a rectangular waveguide. (b) The analog for the experimental setup that treats the SQUID meta-atoms or metamaterials as an effective medium with length l and effective permeability μ_r inside a waveguide.

mine $\delta(\tau)$ in steady state. The $\delta(\tau)$ also has a dc component and an rf component.

To obtain the resonant performance of the SQUID meta-atoms and metamaterials, we measure the resonant frequency and the resonance of our SQUID meta-atoms and metamaterial using the setup in Fig. 2.5 (a). The SQUID meta-atom or metamaterial is positioned in a rectangular waveguide (either X, Ku, or K-band), orientated so that the rf magnetic field of the propagating wave is perpendicular to the SQUID loops (Fig. 2.5 (a)).

As the SQUID meta-atoms are on resonance, they absorb energy traveling through the waveguide, thus the transmission S_{21} as a function of frequency will show a dip at the resonant frequency. We calculate S_{21} of this setup by treating the SQUID meta-atoms or metamaterials as an effective medium with length l and

effective relative permeability μ_r inserted into the waveguide (Fig. 2.5 (b)), and calculate the S-parameters.

We calculate the effective permeability μ_r of a meta-atom (or a metamaterial) using the rf component. Consider the SQUID as an effective medium with an effective relative permeability, μ_r [60] [114], we find

$$\mu_r = 1 + F\left(\left\langle \frac{\Phi_{ac}}{\Phi_{rf}\sin\omega t}\right\rangle - 1\right), \tag{2.11}$$

where Φ_{ac} is the rf flux response of the loop, the angle brackets represent time averaging, and F is the filling fraction of the SQUID in the medium [65] [115]. The transmission and reflection through a partially filled rectangular waveguide with the rf-SQUID medium can be calculated and compared to experiment [62]. The transmission S_{21} is proportional to the ratio of the transmitted electric field, E_T, to the incident field E_0, and can be calculated using the continuity of E and H fields at the boundaries of the effective medium and the empty waveguide as

$$S_{21} = \sqrt{\gamma}\frac{E_T}{E_0} = \frac{\sqrt{\gamma}}{\cos kl - \frac{i}{2}\left(\frac{1}{\gamma}+\gamma\right)\sin kl}, \tag{2.12}$$

where l is the effective length of the medium, $\gamma = k/(\mu_r k_0)$, $k = \sqrt{\mu_r\left(\omega/c\right)^2 - \left(\pi/a\right)^2}$ is the wave number in the medium, and $k_0 = k(\mu_r = 1)$ is the wave number in the empty waveguide.

Chapter 3: Experiment Setup and Sample Designs

3.1 Fabrication and Design of SQUID Meta-atoms and Metamaterials

The 3D structure of a single rf-SQUID design is shown in Fig. 3.1 (a) . Two dimensional metamaterials were constructed by positioning rf-SQUID meta-atoms in a square grid array on a planar substrate. Two Nb films (135 nm and 300 nm thick) connected by a via and a Josephson junction make up the superconducting loop with geometrical inductance L. The capacitance C has two parts: the overlap between two layers of Nb with SiO_2 dielectric in between, and the Josephson junction intrinsic capacitance.

The single rf-SQUID meta-atoms the metamaterials were fabricated by Hypres Inc. in Elmsford, New York. The meta-atom has a superconducting transition temperature $T_c = 9.2$ K. We plot the layout for one of our SQUIDs in Xic Graphical Editor [116] and label each layer in Fig. 3.1 (b). The inset blows up the Josephson junction area. There are through holes in the two Nb layers designed to prevent vortices from moving around. According to our experimental results, this might not be a good idea because these holes would trap magnetic flux, which may be the

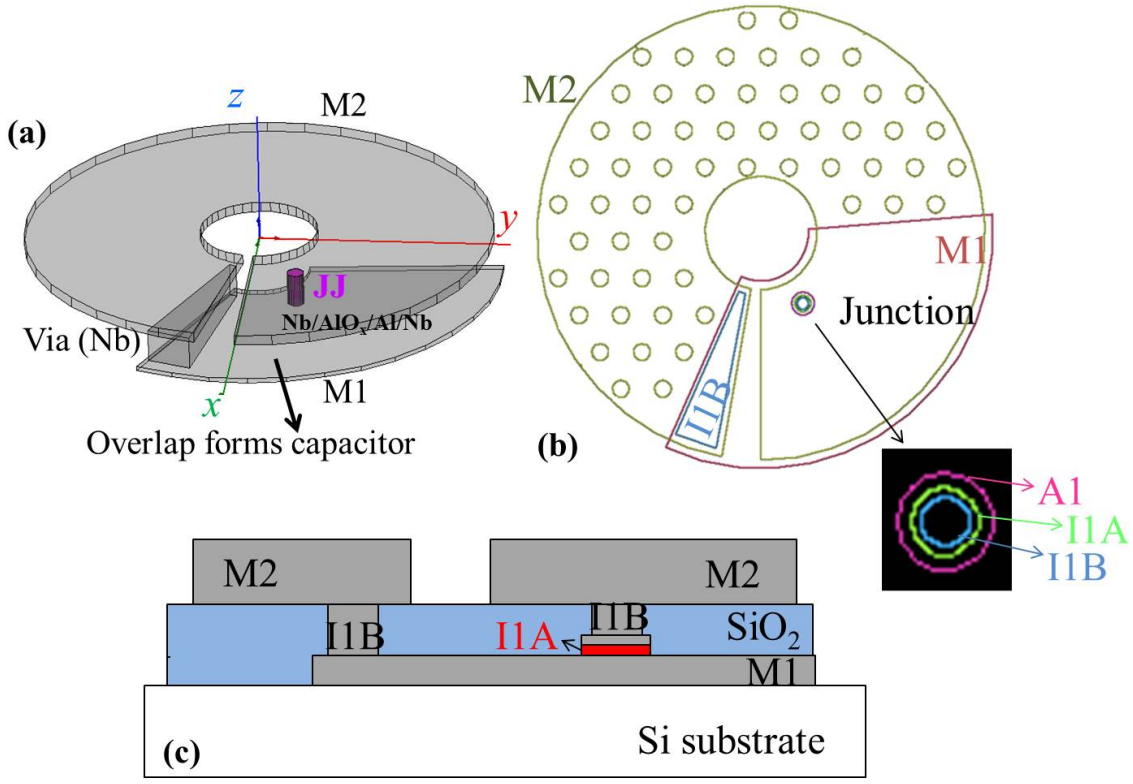

Figure 3.1: (a) The 3D structure of a single rf-SQUID. The distance between the two niobium layers is exaggerated to show the overlap capacitance. (b) The mask layout of (a). (c) The chip cross-section at the junction looking into the x-axis of (a). The gray areas represent the niobium films, the blue area denotes the SiO_2 dielectric layer. The red area is the Josephson junction. The layers are labeled by their mask names respectively.

reason we usually see an offset in the dc magnetic field. Figure 3.1 (c) shows the chip cross-section at the junction looking into the x-axis of Fig. 3.1(a).

The fabrication process is composed of several main procedures: 1) the first layer of niobium film M1 (135 nm) is deposited and etched to the designed shape; 2) the Josephson junction layer I1A (50 nm) is defined and fabricated using Hypres 0.3 μA/μm^2 Nb/AlO$_x$/Nb junction process; 3) the dielectric layer SiO$_2$ (200 nm) is deposited to separate and isolate Nb layers, and then etched to form the via (I1B) between M1 and M2, and the through holes from M2 to the junction; 4) the second Nb layer M2 (300 nm) is deposited and etched according to the design. Both M1 and M2 layers have a penetration depth of $\lambda = 90$ nm [117]. After these processes a layer of SiO$_2$ material is deposited on top of the whole chip to protect the device from oxidization and damage. The details of the process flow and properties of each layer in designing our SQUIDs are shown in Table 3.1 and Table 3.2.

Note that the Nb ground plane utilized in the standard Hypres process will affect our SQUIDs' properties and we need to get rid of it. We define the area of layers M0 and I0 to cover the whole chip (see chip layout Fig. 3.2) so that they would be developed away through lithography process since the mask polarity of the two layers are negative. The resistance layers and contact pads (not shown in Table 3.1 and 3.2) are not used in our design; details of them can be find in the Hypres website [117].

The rf-SQUIDs are designed to be low-noise ($\Gamma = \frac{2\pi k_B T}{\Phi_0 I_c} < 1$ where T is the temperature and I_c is the critical current in the Josephson junction, and $L_F = \frac{1}{k_B T}\left(\frac{\Phi_0}{2\pi}\right)^2 >> L$ [118]) and non-hysteretic ($\beta_{rf} = \frac{2\pi L I_c}{\Phi_0} < 1$).

Table 3.1: Selected Hypres Niobium Process Flow Overview

Layer	Description	Mask polarity
	Nb deposition	
M0	holes in Nb ground plane	-
	SiO_2 deposition	
I0	via between M1 and ground plane	-
	$Nb/AlO_x/Nb$ trilayer deposition	
I1A	Counter-electrode (junction area) definition.	+
	Base electrode anodization	
A1	Anodization layer patterning	+
M1	Quad-layer base electrode patterning	+
	SiO_2 deposition	
I1B	Contact (via) between M2 and (I1A, or M1)	-
M2	M2 layer patterning	+
	SiO_2 deposition	

Table 3.2: Selected Physical Layer Process Specifications

Layer	Material	layer properties	thickness (nm)
M1	Nb	Base electrode. Penetration depth $\lambda_L = 90$nm	135±10
I1A	AlO_x/Nb	Trilayer counter electrode and tunnel barrier	50±5
A1	Nb_2O_5	Insulation on M1 surrounding I1A	40±5
	SiO_2	Insulator. Capacitance: 0.42 fF/μm^2 ± 20 %	100±10
	SiO_2	Insulator. Capacitance: 0.42 fF/μm^2 ± 20 %	100±10
I1B		Contact hole through the above two SiO_2 layers	
M2	Nb	Penetration depth $\lambda_L = 90$nm ± 5 %	300±20
	SiO_2	Insulator. Capacitance: 0.08 fF/μm^2 ± 20 %	500±40

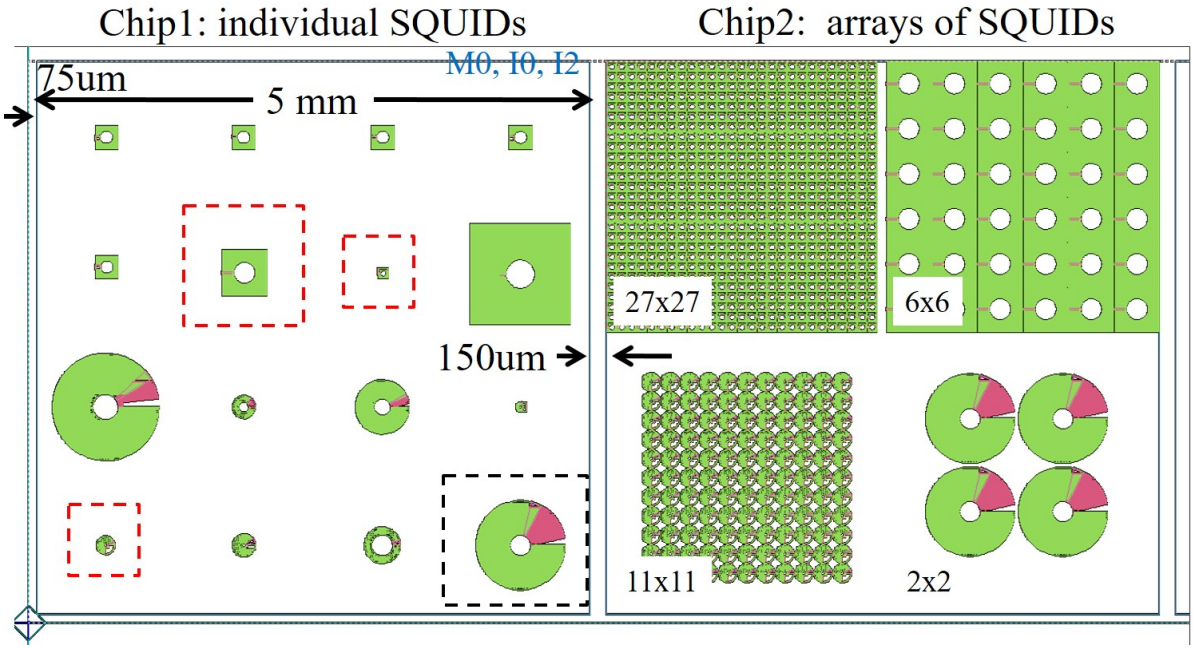

Figure 3.2: The layouts of the SQUID chips we designed and had fabricated at Hypres. The white areas represent the Silicon substrate and the top SiO_2 protection layer. The green and red areas denote the M2 and M1 layers, respectively.

There are additional constraints when we design the samples. First of all, the SQUIDs should operate around 10 - 20 GHz to meet the frequency requirement for the Hypers next generation wireless communication system. Thus all the designs have geometrical resonant frequency $f_{geo} = 1/(2\pi\sqrt{LC})$ inside this frequency range of 10 - 20 GHz. We also hope to get maximum tunability by dc flux without going into the hysteretic regime, by demanding $\beta_{rf} = 2\pi LI_c/\Phi_0 < 1$ but close to unity.

We designed 16 distinct single SQUIDs, each has a different value of f_{geo} as well as a different size. The layouts shown in Fig. 3.2 are drawn in Xic Graphical Editor [116]. We design two chips both of 5mm×5mm; one is for individual SQUIDs, and one has four arrays of SQUIDs. The two chips are separated by 150 μm for dicing required by Hypres design rules. Four arrays (27×27, 6×6, 11×11, 2×2)

are composed of identical SQUIDs meta-atoms that are labeled by red and black dashed boxes in Fig. 3.2. The SQUID in the black dashed box is the only single SQUID meta-atom we measured. Results in the following chapters on the single SQUID meta-atom comes from this design. The optical image of this SQUID is shown in Fig. 3.3 (a). The detailed parameters of the individual SQUIDs in Fig. 3.2 can be found in Anlage group backup space.

The inner radius r_i and the outer radius r_o of the superconducting loop determines its self magnetic inductance L at a fixed temperature. The penetration depth λ obeys $\lambda < d/2$ (d is the thickness of the superconducting films) for the M2 layer. For the M1 layer, $\lambda > d/2$, but the two-dimensional screening length $2\lambda^2/d << r_i$. So we can assume that on the superconducting surfaces, the normal component of the magnetic induction is zero [119]. A consequence is that the superconductor has inverse-square-root singularities in the sheet-current distribution at the edges, which leads to a simple expression for the inductance of the thin-film superconducting ring [119]

$$L = \mu_0 r_o[\frac{r_i}{r_o} - 0.197(\frac{r_i}{r_o})^2 - 0.031(\frac{r_i}{r_o})^6 + (1 + \frac{r_i}{r_o})\tanh^{-1}\frac{r_i}{r_o}].$$

Here r_i and r_o are in units of meters, $\mu_0 = 1.26 \times 10^{-6}$ H/m is the permeability of free space, and the inductance is in units of Henry.

I also calculate the kinetic inductance of the superconducting ring according to Ref. [120], and find it is almost 5 orders of magnitude less than the self-inductance at temperature below the critical temperature T_c of the superconducting film (9.2 K).

The kinetic inductance starts to play a role only when the temperature is close to the critical temperature. Our base temperature of the cryostat is 4.6 K; the kinetic inductance is thus neglected in our design.

We will use the size of the loop (or the inductance L), the β_{rf}, and f_{geo} to complete the design of the junction and the capacitance. Knowing $\beta_{rf} = 2\pi L I_c/\Phi_0$ and L gives the value of critical current I_c through the junction, and further the area of the junction A_{JJ} since the critical current density in the Hypres process is 0.3 μA/μm^2. The Josephson capacitance is then:

$$C_{JJ} = \frac{1}{24.7 - 2.0 \ln j_c} \times A_{JJ},$$

where A_{JJ} is the junction area in units of μm^2, j_c is in units of μA/μm^2, and C_{JJ} is in units of pF.

The total capacitance C can be obtained from the values of the geometrical resonance f_{geo}, and the inductance L. The Josephson capacitance C_{JJ} and the overlap capacitance C_o (from the SiO_2 layer sandwiched by two Nb layers) are in parallel, so $C = C_{JJ} + C_o$. According to Hypres fabrication design rules,

$$C_o = 0.42 A_o.$$

Here, A_o is the the overlap area in units of μm^2, and C_o are in units of fF. Thus the overlap area A_o of the two Nb layers can be also derived.

Two examples of our sample designs are discussed here. Figure 3.3 shows the

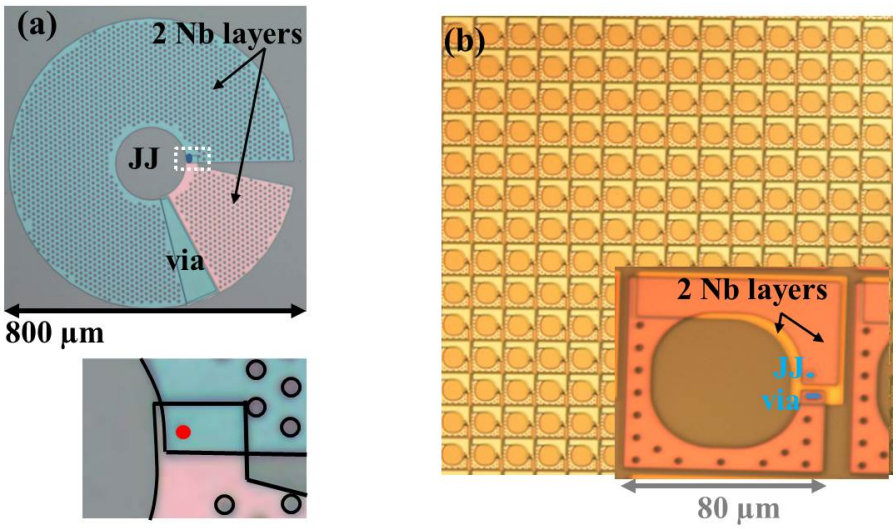

Figure 3.3: The optical images of (a) the single rf-SQUID meta-atom, and (b) part of a 27 × 27 array. Inset of (a) is a zoom-in of the dashed rectangular box. Inset of (b) shows a SQUID meta-atom inside the 27 × 27 array metamaterial, where the Josephson junction, the via, and the two Nb layers are labeled.

optical images of (a) a single rf-SQUID meta-atom and (b) a 27 × 27 array SQUID metamaterial. The single meta-atom is on a 1.25mm × 1.25mm chip and the array is on a 2.5mm × 2.5mm chip. The single SQUID has an outer diameter of 800 microns, while the meta-atoms in the array has a small outer diameter of 80 microns.

Note that larger SQUID size results in higher value of the inductance. To compensate for β_{rf} and f_{geo} respectively, we need to have a small junction size as well as a small overlap area for the capacitor. That is why the large single SQUID (Fig. 3.3 (a)) has a very small overlap area and a small junction (radius of 1.3 micron), while the meta-atoms in the array (Fig.3.3 (b)) has an overlap area taking up half of the loop, with a junction radius of 3 micron.

The parameters for the single meta-atom are: Geometrical inductance of the rf-SQUID loop $L = 280$ pH, the total capacitance $C = 0.495$ pF, the geometrical

resonant frequency $\omega_{geo}/2\pi = 13.52$ GHz, the resistance in the junction $R = 1780$ Ω (4.6 K), $I_c = 1.15\mu$A (4.6 K), $\beta_{rf} = 0.98$, rf-SQUID inner diameter 200μm, outer diameter 800μm. The 0 dc flux low-power resonant frequency is at 19 GHz at 4.6 K.

The parameters for meta-atoms of the 11×11 array at 4.6 K: $L = 55.99$ pH, $C = 2.1$ pF, $\omega_{geo}/2\pi = 14.85$ GHz, $R = 500$ Ω, $I_c = 5\mu$A, $\beta_{rf} = 0.86$, rf-SQUID inner diameter 40μm, outer diameter 160μm, center-center distance 170μm. The 0 dc flux low-power resonant frequency is at 20.25 GHz.

3.2 Experimental Setup

We measure the resonant frequency and the resonance of our SQUID meta-atoms and metamaterial using the setup in Fig. 3.4. Our sample is positioned in a rectangular waveguide (either X, Ku, or K-band), orientated so that the rf magnetic field of the propagating wave is perpendicular to the SQUID loops and couples to the meta-atoms (Fig. 3.4) [62]. The waveguide is made of copper and is not superconducting. The rectangular waveguide allows us to excite single-mode propagation which ensures that the rf magnetic field is perpendicular to the sample, it also opens up the opportunity for measurement of 3D SQUID metamaterials. A superconducting coil outside the waveguide provides dc magnetic field also perpendicular to the SQUID loops. The sample sits inside a pulsed-tube refrigerator with a base temperature of 4.6 K. The temperature is controlled via an electric resistor heater, and measured by a diode thermometer.

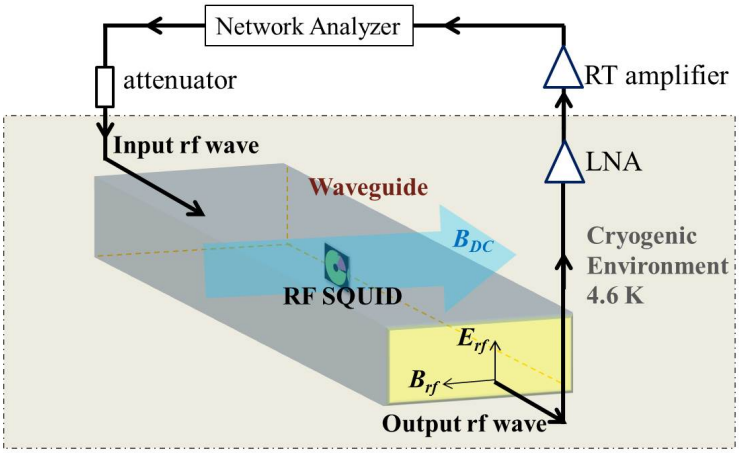

Figure 3.4: Schematic diagram of the experiment showing the flow of the rf signal from the network analyzer (at room temperature, RT), through the attenuator, into waveguide (in the cryogenic environment), through the rf-SQUID sample biased by dc magnetic field, out of the waveguide through a series of amplifiers, and back to the network analyzer.

We assembly these parts in the cryostat as in Fig. 3.5 (a). The waveguide is clamped by an E-shape customized waveguide holder (Fig. 3.5 (b)) made of oxygen-free high thermal conductivity (OFHC) copper. The holder is screwed tightly beneath the 4K plate for good thermal conductivity. The sample is stabilized in the waveguide by a kind of foam called "rohacell" [121], which has nearly the same dielectric properties as air [121]. We cut the rohacell to fit the size of a waveguide, and open up an aperture in it to put our sample, then insert the rohacell with the sample inside the waveguide. The superconducting solenoid is made of NbTi (critical temperature is 10 K) wrapped around a Bakelite coil holder designed to fit each waveguide (see Fig. 3.5 (b)). The coil is clamped to the waveguide with good thermal conductivity by a customized copper clamp. A resistor heater is screwed tightly to the waveguide holder by a heater clamp. Two waveguide adapters transition the microwave signals between coaxial and single-conductor waveguide geometries. A

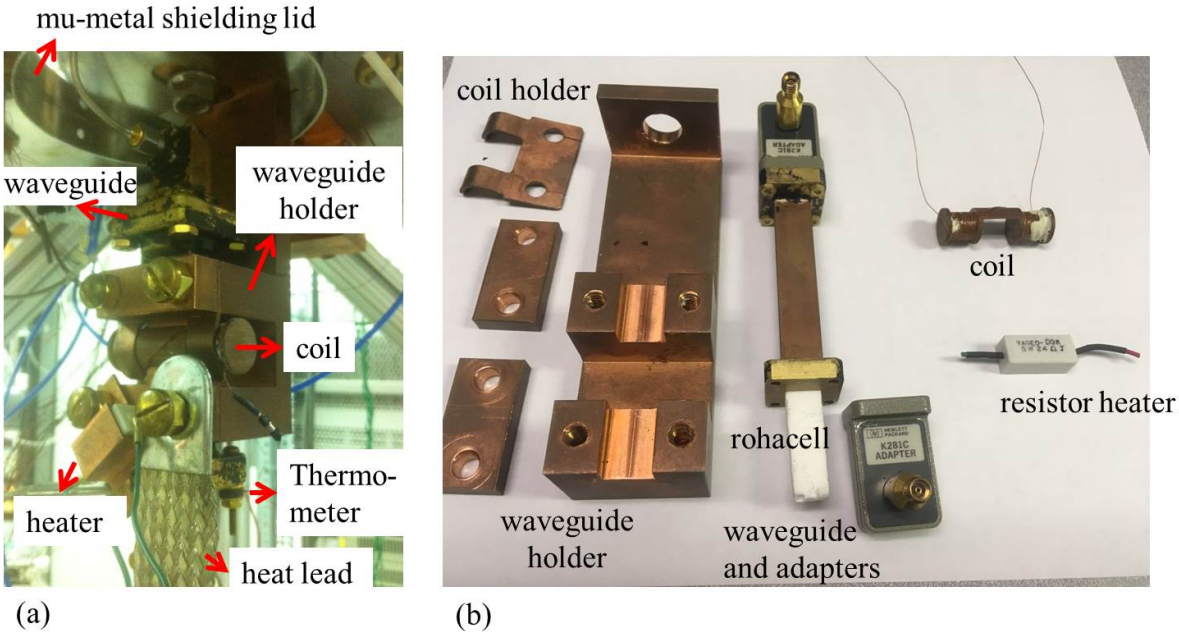

Figure 3.5: Picture of the waveguide and components around it for the measurement. (a) Assembled parts inside the cryostat. (b) Details of each part. The waveguide holder is composed of a clamp and two planar pieces with screw holes to stabilize the waveguide in the clamp; the through hole on the top is for attaching to the 4K plate. The rohacell carrying the sample is inserted in the rectangular waveguide and the two adapters. The coil is made up of superconducting wires; it is held in position with a coil holder. The resistor heater is attached to the waveguide holder by a heater holder; the two connections are for dc current to flow through the heater and generate heat.

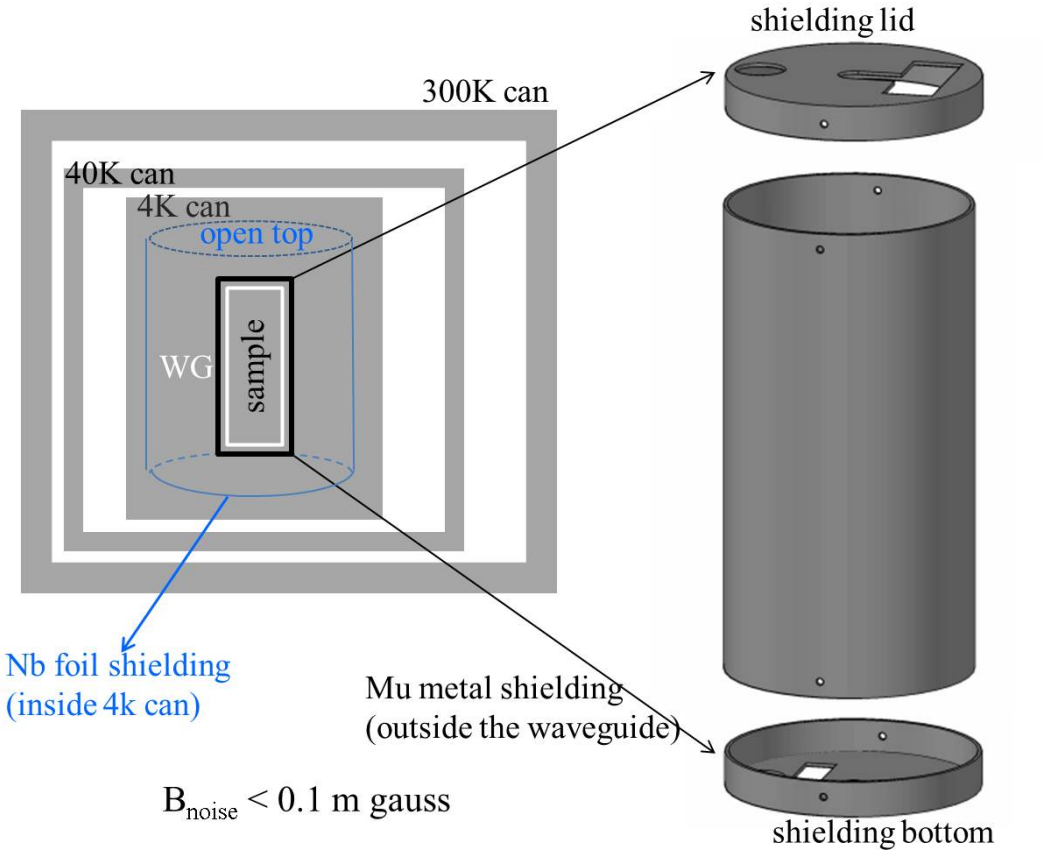

Figure 3.6: Schematic of the magnetic shielding layers inside the cryostat made of three temperature-stage cans.

thermometer is attached to a corner of the bottom waveguide adapters by a screw. For better thermal conductivity, one or two grounding braids (heat leads) made of tin-plated copper conductor are screwed on the waveguide and holder, and are attached tightly to the 4K plate of the cryostat.

The sample is protected from environmental magnetic fields via several layers of magnetic shielding around the waveguide, including one layer of Nb foil with a thickness of 100 micron covering the side walls and bottom of the 4K can, and a μ-metal cylindrical box. The schematic of the magnetic shielding layers are shown in Fig. 3.6. The μ-metal shielding is composed of three parts: the lid, the body, and the bottom. Four screws attach them together. The openings in the top lid allows one coaxial cable and the thermometer into the shielding, and helps screwing together the top of the waveguide holder and the top of the 4K plate (see Fig. 3.5 (a)). The openings cut in the bottom lid are used for connecting the other coaxial cable, all the dc wires (for the coil and the heater), and the heat leads into the shielding.

The dc current through the superconducting coil is applied by a Keithley 220 programmable current source. The transmission and reflection signals from our sample are amplified by a cryogenic low noise amplifier (LNF-LNC6_20A) and a room temperature amplifier (HP 83020A), and are measured by a network analyzer (Agilent N5342A). The wires of the heater are connected to a Lake Shore Cryogenic Temperature Controller (Model 340).

Our experiment detects the resonance as a dip in the frequency dependent transmission magnitude through the waveguide $|S_{21}(\omega)|$. We observe the change in

frequency and strength of the resonance dip as we change various parameters, such as dc flux, rf flux, temperature and stimulus scanning directions.

3.3 Verification of Experiment Design with HFSS

There are several things to verify before we finalize the designs for the SQUID samples, as well as the experimental setup. For example, how would the substrate of the SQUIDs affect the resonance, how well does the waveguide mode couple magnetically to the sample, will there be a measurable resonance, and so on. We look into these concerns with the High Frequency Structure Simulator (HFSS) electromagnetic simulation package.

The SQUID layout in .gds file format can be directly imported into HFSS. We then assign material properties and thicknesses to each layer. An example is shown in Fig. 3.7. HFSS does not have the ability to simulate superconductors and Josephson junctions, and it can only simulate linear responses. Therefore, we treat the superconducting material Nb as perfect electric conductors (PEC) which have zero resistivity. The nonlinear Josephson junction is treated as a PEC material with a lumped parallel RLC boundary. The resistance and capacitance of the lumped RLC boundary are the nominal design values for the Josephson junction. The effective Josephson inductance is related to the dc flux so it can be derived as well and included in the HFSS model.

We first check if the SQUID has a resonance within the frequency range of single-mode propagation in the waveguide. To make sure that there is a strong

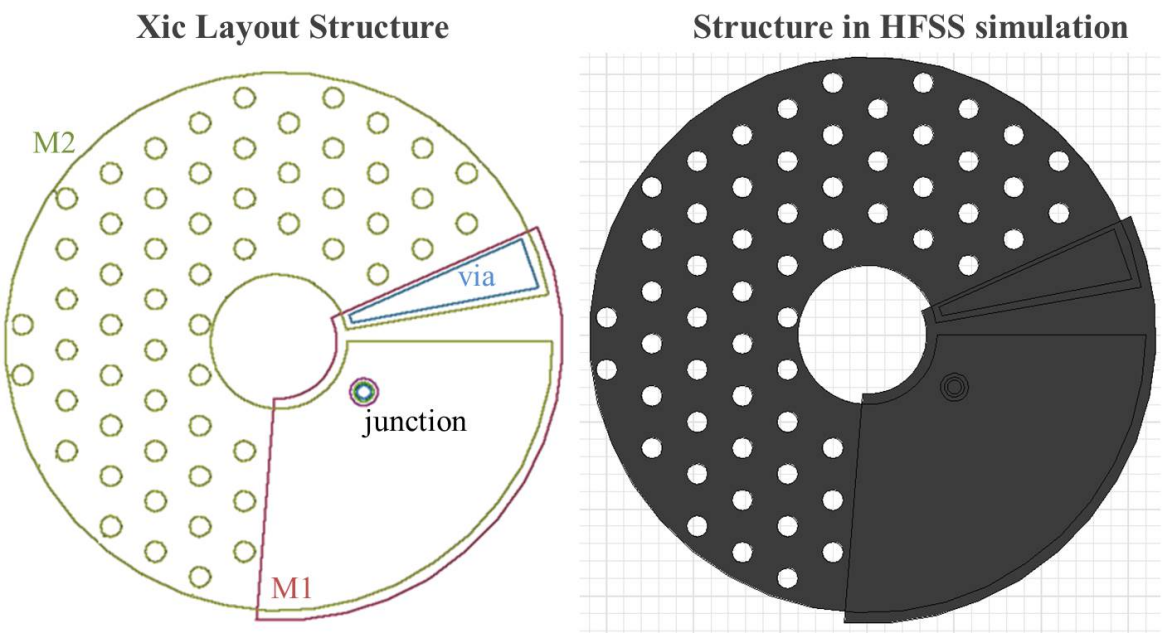

Figure 3.7: The picture of SQUID layout in Xic layout software and in HFSS.

coupling and thus a strong signal in HFSS simulation, we use a pair of rf magnetic loops (diameter of 0.2 mm and separation of 1 mm) to excite the SQUID directly, instead of a rectangular waveguide. A single SQUID is positioned in the center of a pair of rf magnetic loops (inset of Fig. 3.8). The loops are coaxial cables where the stripped inner conductor bends and connects to the outer conductor. The rf wave is sent into the magnetic loops through two ports at the ends of the coaxial cables, and we simulate S_{21} of the system. The current flowing in the top loop creates a magnetic field coupling strongly to the SQUID, which in turn induces some magnetic field and couples to the lower loop. In this SQUID design, the resistance is 2880 Ω, and the Josephson capacitance is 0.88 pF.

We simulate the zero dc flux case and the half quantum flux case by assigning the Josephson inductance to be 73 pH and -73 pH respectively (at a temperature of 6.5 K). Figure 3.8 shows S_{21} as a function of the frequency of the input signal.

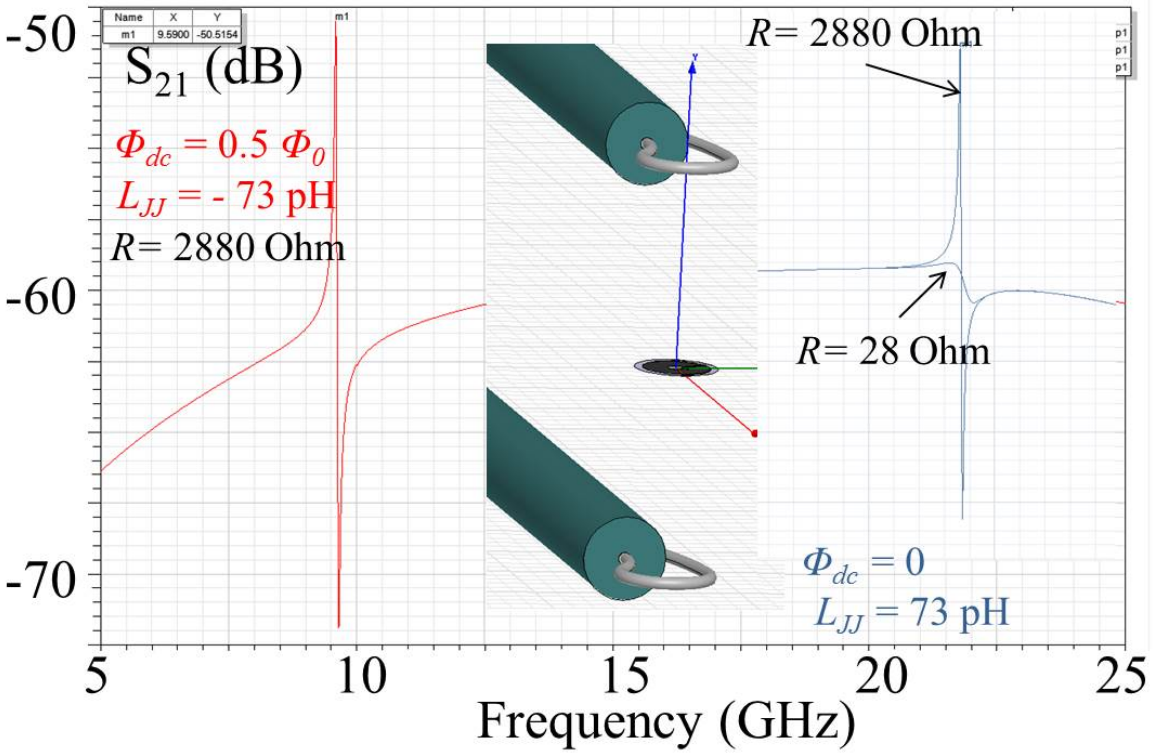

Figure 3.8: HFSS simulation result for the SQUID coupled to a pair of rf magnetic loops. The simulated transmission shows a resonant feature (red) at around 9.7 GHz at a dc flux of $0.5\Phi_0$, and a resonant feature (blue) at 22 GHz at 0 dc flux. Two 0 dc flux transmission simulation also shows that lower resistance gives rise to a weaker resonance.

The resonance feature is at around 21.8 GHz and 9.6 GHz for $\phi_{dc}/2\pi$ of 0 (blue curves), and 0.5 (red curve), respectively. The results verify that the SQUID can resonate when excited by rf magnetic field, and the resonant frequency is similar to our design.

We vary the resistance in the Josephson junction, and simulate again for the zero dc flux case (Fig. 3.8). Clearly a higher resistance results in a sharper resonance feature (higher quality factor). This justifies our choice of not having external shunt resistance in the SQUID design.

Figure 3.8 is a result for a SQUID without holes in the Nb layers and without the thick silicon substrate. We simulate the same SQUID again with holes in the lower film as in our layout and find that the holes only reduce the resonant frequency by at most 0.1 GHz. Further, adding a 500 micron thick silicon substrate to the SQUID chip drops the resonant frequency by 0.5 GHz. Thus, it is safe to conclude that the SQUID equation (Eq. (2.9)) can effectively predict the behaviors of the SQUID meta-atoms and metamaterials, even with some extra small holes in the superconducting loop, and with a silicon substrate. The effects of holes and substrate cannot be measured directly, thus will just be treated as modifications to the parameter set of the RCSJ model, in the following sections.

Next we simulate the SQUID in a rectangular waveguide and see if there is still a resonance feature in the calculated transmission S_{21}. The simulated transmission of the SQUID meta-atom (same design) in a 5 cm long X-band waveguide as a function of frequency is shown in Figure 3.9 for $\phi_{dc}/2\pi = 0.5$. The TE mode is excited so that the SQUID is oriented perpendicular to the rf magnetic field. On

resonance, the SQUID absorbs energy from the propagating wave so there is a dip at the resonant frequency 9.5 GHz. Note that the SQUID fills up very small space inside the waveguide, so the resonance dip is only -0.0023 dB deep. We utilized several methods in HFSS trying to strengthen the signal. One is to add an extra metal ring close to the SQUID to create more perturbation. It does not work out because the response of the ring totally overwhelms the signal coming from the SQUID. Other methods like operating in a smaller waveguide and simulating a larger SQUID array can increase the signal strength. A higher resistance value also greatly improves the quality factor and depth of the resonance.

We simulated a 3×3 array SQUID metamaterial inside the rectangular waveguide using the same design as the previously simulated single SQUID. The resonant frequency increases to 10.3 GHz, as expected from the coupling of the SQUID meta-atoms [68].

In experiment, it is hard to position the SQUID exactly at the center of the waveguide, and perfectly perpendicular to the rf magnetic field of the TE mode. Results of HFSS simulation actually reveals that positioning the SQUID closer to one end of a waveguide can greatly increase the resonance strength. Tilting the sample up to 15° does not affect the resonance much. However if we tilt the sample so much that it is perpendicular to the electric field, the resonance strength is around 5 orders of magnitude smaller than coupling to the magnetic field. The other orientation of the SQUID, perpendicular to the wave propagation direction, gives a signal that is 4 orders of magnitude smaller than the case when the rf magnetic field B_{rf} is perpendicular to the SQUID.

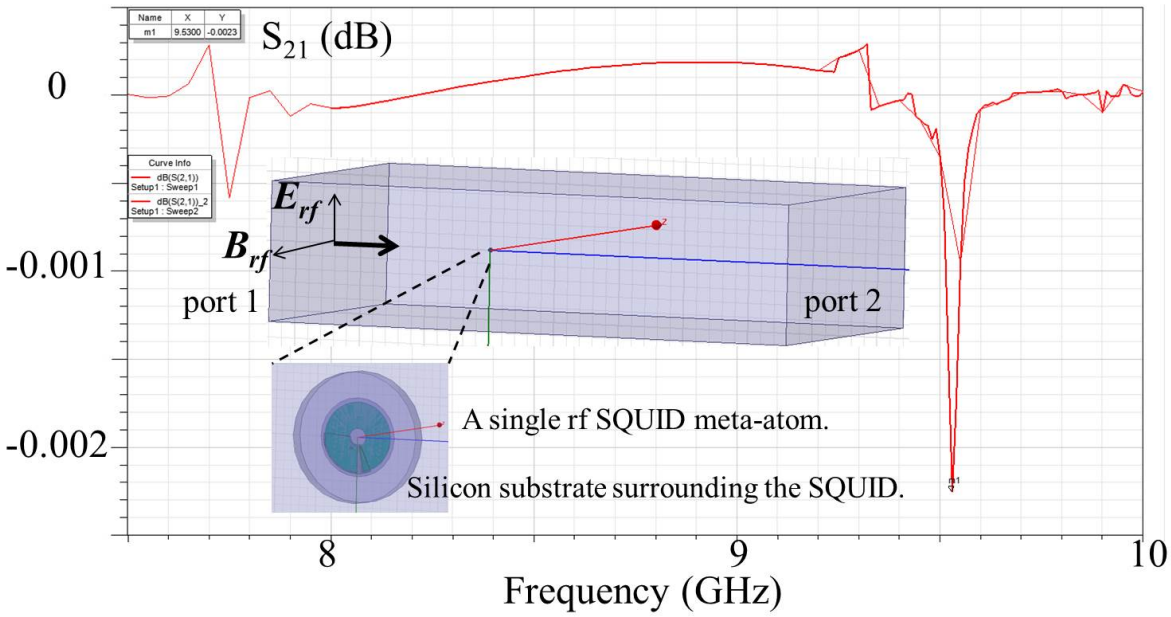

Figure 3.9: HFSS simulation result for the SQUID in a X-band rectangular waveguide.

In summary, simulation of HFSS verify the SQUIDs and measurement designs, giving us an idea of the signal strength, and give some idea of the sensitivity of the results to the orientation and placement of the SQUID in the waveguide. In the next chapter the measurement results of SQUID meta-atoms and metamaterials will be discussed.

Chapter 4: Experiment and Simulation Results for SQUID Meta-atoms and Metamaterials

There are many parameters that one can tune to modulate the response of an rf-SQUID. In our experiment, we mainly look at the modulation of resonance through rf magnetic flux (rf power of the input wave), dc magnetic flux, drive frequency, and temperature. The rf flux, or the drive amplitude, determines the nonlinear regime of a SQUID. Under three levels of the drive amplitude (low, intermediate, and strong), the SQUIDs behave dramatically differently. The dc magnetic flux tunes the resonant frequency for low and intermediate rf drive amplitudes. The temperature changes the critical current, and thus the parameter β_{rf} that sets the degree of nonlinearity and the range of tunability. We will discuss these effects seen in experimental data, under low, intermediate, and high rf drive amplitude, respectively, in this chapter.

4.1 Large DC Flux Tunability of Resonant Frequency in SQUID Meta-atoms and Metamaterials at Low rf Drive Amplitudes

As discussed in Chap. 2, when the rf-SQUID is driven by a small rf flux ($\Phi_{rf}/\Phi_0 < 0.001$), the Josephson junction is effectively a tunable inductance $L_{JJ} = \Phi_0/(2\pi I_c \cos\delta)$ where δ is determined by the applied dc flux by

$$\delta + \beta_{rf} \sin\delta = \phi_{dc}. \tag{4.1}$$

The resonant frequency of the lumped RLC circuit for an rf-SQUID is

$$f_0 = \frac{1}{2\pi\sqrt{\left(\frac{1}{L} + \frac{1}{L_{JJ}}\right)^{-1} C}}, \tag{4.2}$$

and can be tuned by the applied dc flux (which modifies L_{JJ}) and temperature (which modifies the critical current I_c).

4.1.1 Single rf-SQUID Meta-atom

Figure 4.1 (a) shows the experimental results for $|S_{21}|$ of an rf-SQUID meta-atom as a function of dc flux and frequency for an input rf power of -80 dBm. The rf power results in an rf magnetic flux through the loop and drives the SQUID. The incident rf flux amplitude at the sample and the temperature were fixed at $0.003\Phi_0$ and 6.5 K, respectively. Resonance dips in $|S_{21}(\omega)|$ appear as the red features in the plot against a yellow background of unaffected signals ($|S_{21}|$= 0dB). The signal was

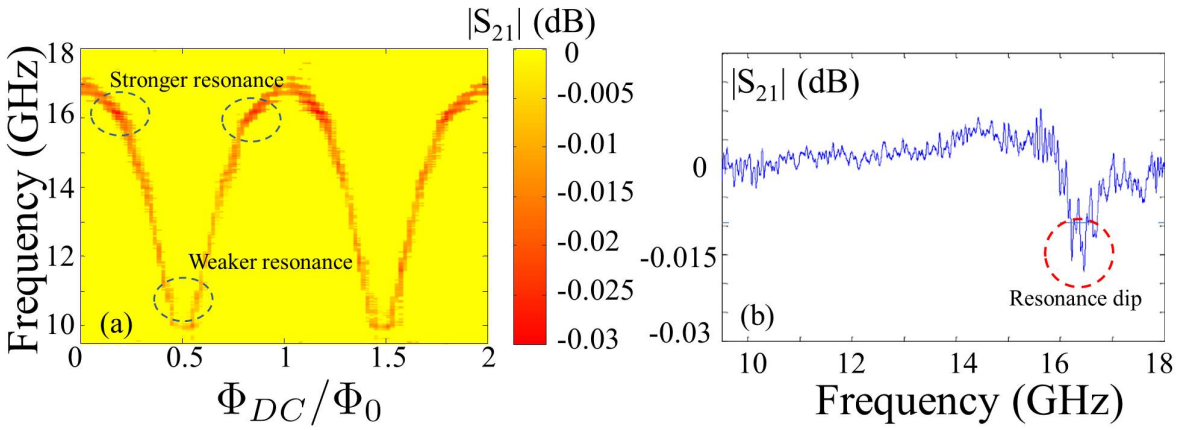

Figure 4.1: (a) Experimental measurements of $|S_{21}|$ of the rf-SQUID meta-atom as a function of frequency and applied dc flux at $0.003\Phi_0$ rf flux and 6.5 K. The resonant response is identified by the red features. (b) The $|S_{21}|$ of 0 dc flux.

extracted by subtracting $|S_{21}|$ at 16 K (which is well above the critical temperature) from $|S_{21}|$ at 4.6 K, removing a background variation, and applying a threshold to identify the resonance. The transmission dips show good periodicity as a function of dc flux, with a maximum resonant frequency of 17 GHz and minimum at around 9.5 GHz. Ku waveguide is used here; the cutoff frequency of the Ku waveguide is 9.5 GHz which imposes a lower frequency limit on this measurement.

A frequency cut at 0 dc flux is shown in Fig. 4.1 (b). There is a dip at around 16.5 GHz, with a depth of -0.015 dB and a width of around 1 GHz. The weak signal is due to the small filling factor of the single SQUID meta-atom in a Ku-band waveguide. We are sure that this signal comes from the single SQUID meta-atom because this resonance dip tunes with the applied flux.

There are also some consistent horizontal features on top of the tuning resonance dip feature in Fig 4.1 (a). We believe they comes from standing waves due to the impedance mismatch between components and cables. The transmission as

a function of frequency in Figure 4.1 (b) shows that the standing waves breaks the resonance into several split dips.

To reduce the base temperature, I replaced all the original coaxial cables with low thermal conductivity cables inside the cryostat to ensure low heat exchange with the outside. The cables, made by Coax Company, Ltd. in Japan [122], are made of beryllium copper conductors, are also non-magnetic. This change reduced the base temperature from 6.5 K to 4.6 K (even reaching 4.1 K once). The new cables also caused more attenuation of the microwave signals, which is favored in our measurement.

As the temperature decreases, the highest tunable resonant frequency 17 GHz at 6.5 K is modified to 19 GHz at 4.6 K (Fig. 4.2). The resonant frequency is not measurable below 9.5 GHz due to the cut-off frequency of the Ku-band waveguide, but from the measured geometrical resonant frequency f_{geo} =13.52 GHz (see Sec. 4.2) we can estimate the β_{rf} to be 0.98 at 4.6 K. The theoretical lowest resonant frequency, at a dc flux value of $0.5\Phi_0$, is then $f_{geo}\sqrt{1-\beta_{rf}} = 2$ GHz. The dc flux tunability of approximately 7 GHz at 6.5 K is then modified to approximately 17 GHz at 4.6 K. We also deliberately increased the temperature using an electric heater, and measure the dc flux tunability at different temperatures. The red features in Fig. 4.3 show the dc flux tuned resonances at 6.5 K, 7.6 K, and 8.3 K for an rf flux amplitude of $0.001\Phi_0$.

The increased temperature reduces the flux tunability from $\sim$ 7 GHz at 6.5 K, to approximately 3 GHz at 7.6 K, and approximately 1 GHz at 8.3 K. The grey lines follow the resonance dips by using the solution for δ from Eq. (4.1) and calculating

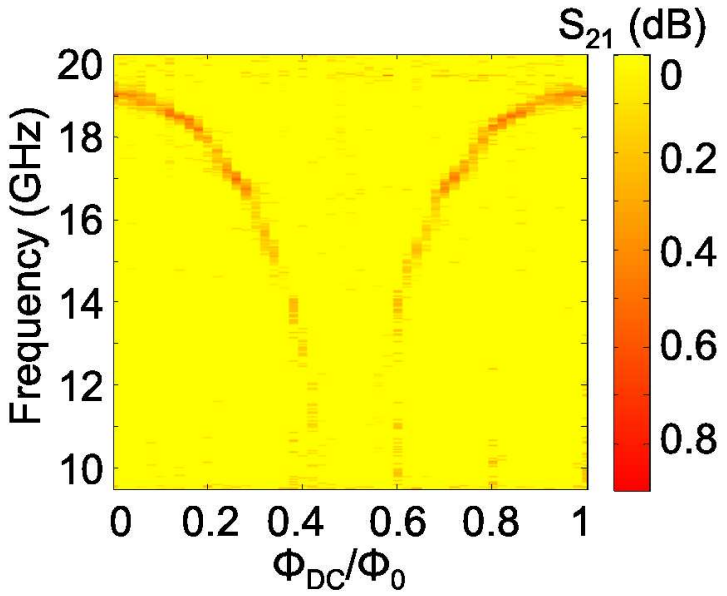

Figure 4.2: Experimental measurements of $|S_{21}|$ of the rf-SQUID meta-atom as a function of frequency and applied dc flux at $0.001\Phi_0$ rf flux amplitude and 4.6 K. The resonant response is identified by the red features.

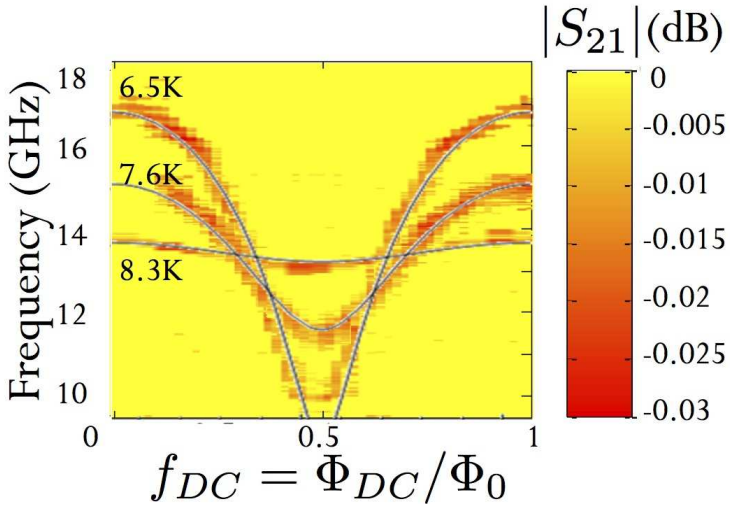

Figure 4.3: Experimental measurements of $|S_{21}|$ of the rf-SQUID meta-atom as a function of frequency and applied dc flux at three different temperatures, 6.5 K, 7.6 K, and 8.3 K, and $0.001\Phi_0$ rf flux amplitude. The resonant response is identified by the red features. The solid lines are the resonant frequency calculated by Eq. (4.1) and Eq. (4.2).

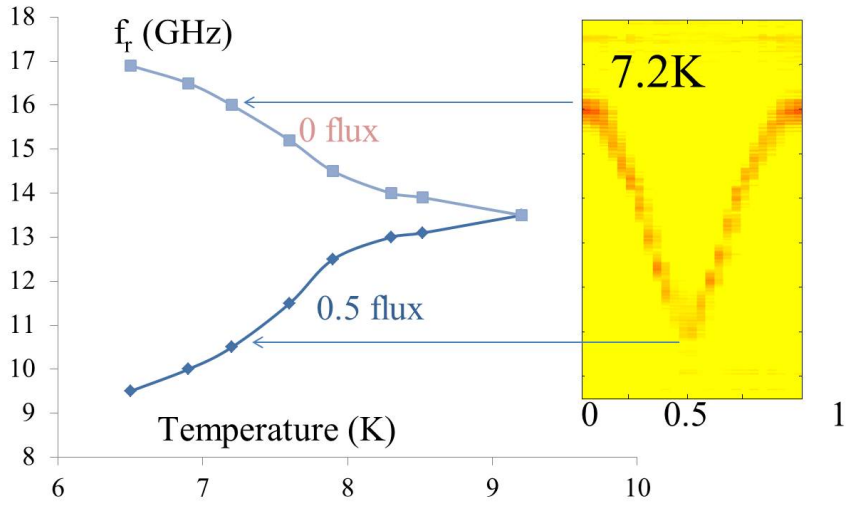

Figure 4.4: The highest and lowest tunable resonant frequency of a single SQUID meta-atom at different temperatures.

the resonant frequency using Eq. (4.2). The only parameter varied to fit this data is the temperature dependent critical current of the junction. We also performed a series of low rf flux amplitude measurements of $|S_{21}|$ as a function of frequency and dc flux for various fixed temperatures ranging from 6.5 to 9.2 K (Fig. 4.4) and observed that at $f_{dc} = \phi_{dc}/2\pi = 0$ the resonant frequency decreases from 17 to 13.5 GHz with increasing temperature and when $f_{dc} = 1/2$ the resonant frequency increases from 9.5 to 13.5 GHz over the same temperature range. The reduction in tunability with increased temperature in consistent with the predictions of the model. Also consistent with the model, the resonant frequency saturates in the high temperature limit at $\omega_{geo}/2\pi = 13.5 \pm 0.2$ GHz (Eq. (2.4)).

4.1.2 RF-SQUID 2D Array Metamaterial

When the SQUIDs are arranged into 2D array metamaterials, the flux-tunability of resonance in rf-SQUID metamaterials is similar to the tunability of a single rf-SQUID meta-atom. However, things become a little complicated because of the coupling between the meta-atoms, as well as the possibility of non-uniform applied flux.

We first look at the dc flux dependence of a 2×2 SQUID array metamaterial (inset of Fig. 4.5) composed of the same large single SQUID discussed before, with a diameter of 800 micrometers. We plot the transmission of this array as a function of frequency and dc flux in Fig. 4.5 when the applied rf flux is in the linear-response limit (power of -80 dBm). The temperature is 6 K. Unlike the single SQUID's transmission results, the resonance dips modulated by dc flux are composed of four nearby tunable curves, each of which represents a resonance of a SQUID meta-atom in the array. The discrete resonance dips all have a highest resonant frequency of around 18 GHz, and lowest resonant frequency below the cutoff frequency of the Ku-band waveguide, 9.5 GHz. They also have similar resonance strengths of -0.04 dB. I label those four resonances in one period as blue, black, white, and green dashed curves, respectively.

To extract the weak resonance features, the data is processed with great care. I first measured the $|S_{21}|(f)$ as a function of frequency for all the dc flux values, and I took the average of these curves to be $|S_{21}|_{avg}(f)$. Then I subtracted $|S_{21}|_{avg}(f)$ from the original $|S_{21}|(f)$ and plotted it in Fig. 4.5. Thus the figure only shows the

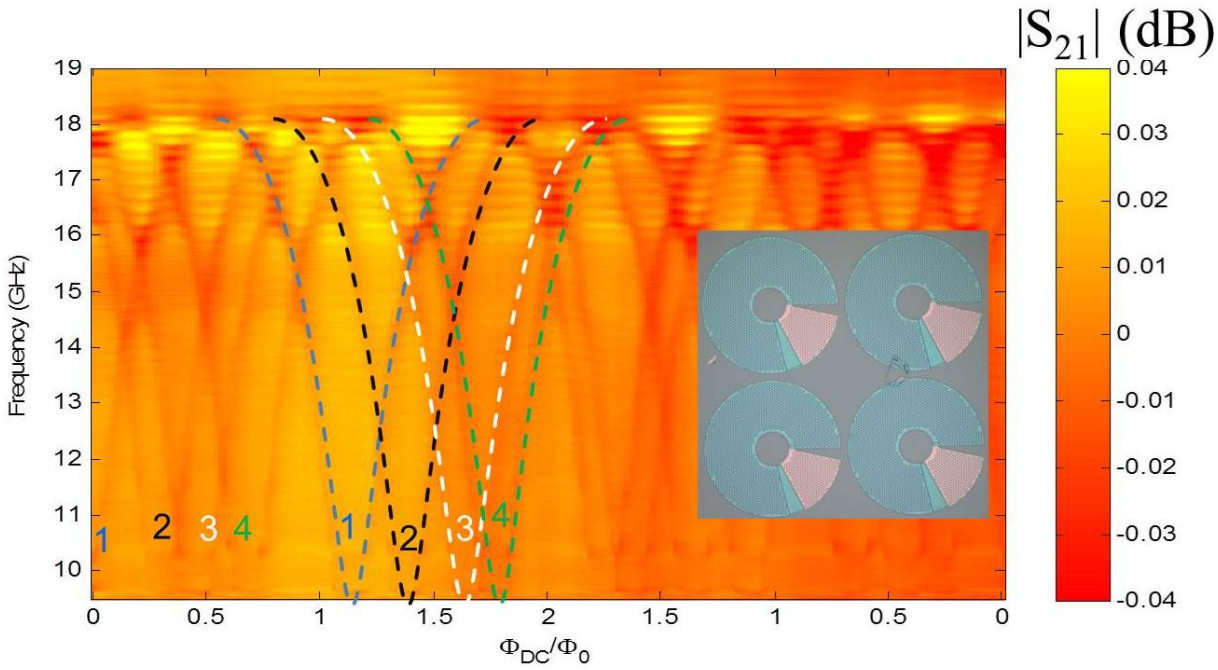

Figure 4.5: Experimental measurements of $|S_{21}|$ of a 2×2 rf-SQUID array metamaterial as a function of frequency and applied dc flux at 6 K, and $0.003\Phi_0$ rf flux amplitude. The resonant response is identified by the red features.

transmission change due to the dc flux applied on the SQUID. The positive values of $|S_{21}|$ are a result of this data processing.

The presence of four separate peaks might be caused by a non-uniform magnetic field. The SQUID meta-atoms are of very large size while the dc magnetic field is provided by a relatively small diameter solenoid. Here the SQUID diameter is around 1 mm, and cross-section of the coil is less then 1 cm in diameter. A small displacement of the SQUIDs to a location off the center of the solenoid can result in significant variation of the magnetic field. Therefore, each SQUID sees a different dc flux value. From Fig. 4.5 we know that the 2×2 array metamaterial has a variation in dc flux of approximately $\Phi_0/2$.

Luckily, 2D SQUID array metamaterials are not always so incoherent. When

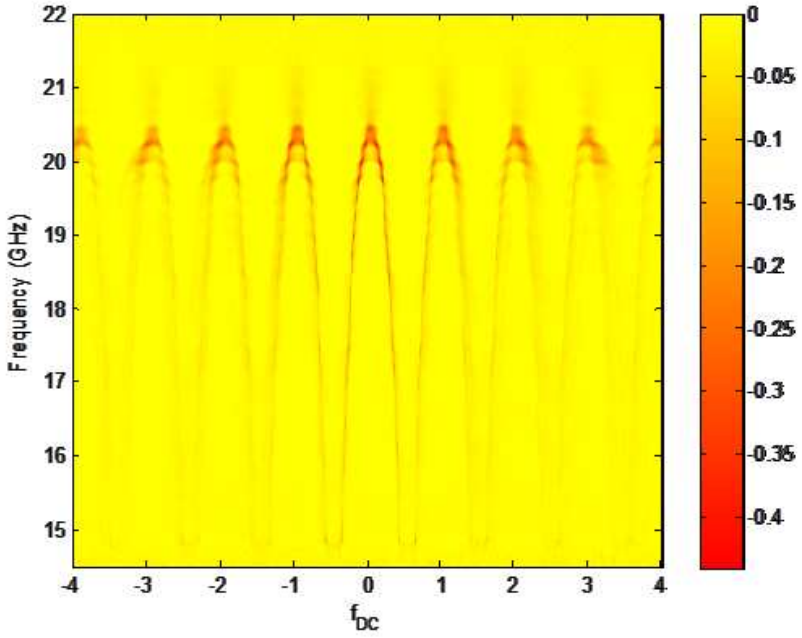

Figure 4.6: Experimental measurements of $|S_{21}|$ of an 11×11 rf-SQUID array metamaterial as a function of frequency and applied dc flux at 4.6 K, and $0.001\Phi_0$ rf flux. The resonant response is identified by the red features.

the applied magnetic field is uniform, an array can resonant coherently, almost like the performance of a single SQUID (see Fig. 4.6).

Figure 4.6 is the transmission for an 11 × 11 SQUID array as a function of frequency and dc flux, when the rf flux is $0.001\Phi_0$ (an rf power of -90 dBm) and the temperature is 4.6 K. The zero applied dc flux renders the highest resonant frequency (20.5 GHz in this case), while lowest resonance is at a half flux quantum, and the tunability is periodic in dc flux. Within two flux quanta the resonance feature tunes with the dc flux just like a single rf-SQUID. However, due to the disorder in the system, the resonance gets wider and shallower as the applied dc flux increases, and the periodicity is also affected. Details about this systematic degradation of the dc flux tuning curve can be found in my colleague's work [68].

Temperature changes the tunability of resonant frequency by dc flux even for a SQUID array. An example of the dc flux dependent transmission of a 27×27 SQUID array at two different temperatures (4.1 K and 7.9 K) is shown in Fig. 4.7 (a). Again, lower temperature results in a much larger tunability and a stronger signal.

The array behaves coherently in the dc flux range -0.5Φ_0 to 0.5Φ_0. Out of this flux range, the disorder in the SQUID array is so large that the resonance dip splits into several branches (labeled as "MI modes" in Fig. 4.7 (a)), due to the appearance of magneto-inductive modes in the the SQUID array [68]. Note here that the distinct MI modes disappear in the resonance dip of SQUID array at 7.9 K. Operating at high temperature might be useful to eliminate the effects of disorder.

Another set of experiments on temperature dependence for the 27×27 SQUID array with low rf flux drive is done at a fixed dc flux (in this case zero flux), while the temperature is changed continuously. The result is shown in Fig. 4.7 (b). As the temperature changes from 4.1 K to 8.5 K, the resonance feature gradually goes down in frequency from 23.5 GHz to 17.5 GHz. Further increasing the temperature to 9.2 K (the critical temperature T_c) leads to a much shallower resonance dip which goes to even lower frequencies (see inset of Fig. 4.7 (b)). Above 9.2 K, there is no measurable resonance dip, because the SQUID is no longer in its superconducting state and thus becomes lossy with low quality factor.

However, if we extract the highest resonant frequency measured for a SQUID array as a function of dc flux, and plot the resonant frequency as a function of temperature on top of Fig. 4.7 (b), the two curves do not match. This is because

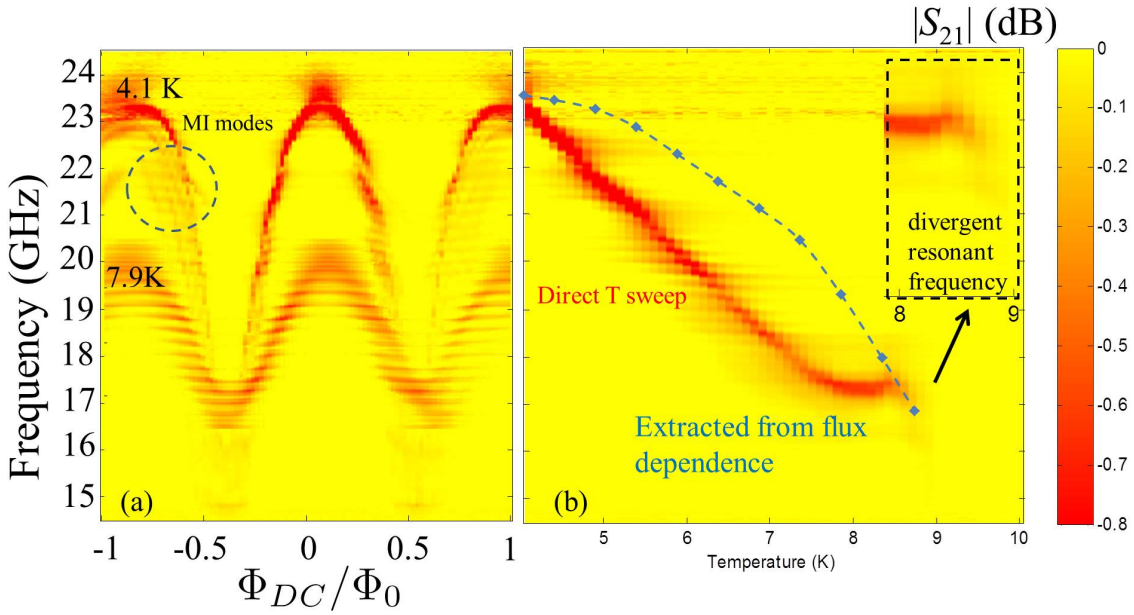

Figure 4.7: Measured transmission of $|S_{21}|$ of a 27×27 rf-SQUID array metamaterial (a) as a function of frequency and applied dc flux at 4.1 K, and (b) as a function of temperature at 0 dc flux. The resonant response is identified by the red features. The inset of (b) blows up the resonance feature at temperatures of 7.8 K to 9.2 K. The blue curve in (b) is plotted as the highest tunable resonant frequency extracted from the dc flux dependent transmission at each temperature. All measurement is under an rf flux amplitude of $0.001\Phi_0$.

the temperature is continuously increased by an electric heater, the ends of which are connected to two dc wires. When electrical current is brought into the heater, there is also magnetic field created by current flowing in the dc wires. This results in additional "dc" flux being applied to the rf-SQUID array. Hence a direct temperature dependence measurement where temperature is the only variable is difficult to realize. In all subsequent temperature dependence experiments, I always run a dc flux dependence experiment first to find the true "0" dc flux. Note here that all the higher temperature results are calibrated so that the dc flux axis reflects the true dc flux value that the SQUIDs experience. Using twisted pairs and careful wiring layout might reduce the dc magnetic flux offset coming with the temperature increase.

Also note that we frequently see an offset in dc magnetic flux value without introducing any external magnetic field (either by the heater or the solenoid) into the magnetic shielding. For example, in Fig. 4.7 (a) the whole red resonance feature is displaced in the x-axis by approximately 0.05. This is possibly because the holes we deliberately design in the Nb layers of the SQUIDs pin some residual field in the sample. Usually the residual magnetic flux is less than $\Phi_0/2$. It is easier to determine the true zero dc flux for the SQUID array than the single SQUID, because under that flux value the SQUID array is the most coherent, has a clear resonance dip and the highest resonant frequency, while the resonance of a single SQUID meta-atom is always periodic in dc flux (unless the field is so high that it destroys the superconductivity in the Niobium layers, or the current in the coils causes measurable temperature increase of the sample and shrinks the frequency

tunability range).

4.2 Broadband Transparency of SQUID Meta-atoms and Metamaterials at Low rf Drive Amplitudes

As the drive rf flux amplitudes increase, the effective Josephson inductance expression $L_{JJ} = \Phi_0/2\pi I_c \cos\delta$ (Eq. (2.3)) is not valid any more because the expression assumes that the term $\cos\delta$ does not vary with time. Even at a fixed applied dc flux, the modulation rf flux changes both the resonant frequency as well as the resonance absorption strength [64].

Measured transmission of a single meta-atom as a function of frequency and rf flux Φ_{rf} at a temperature of 4.6 K under 0 dc flux is shown in Fig. 4.8 (b). Red features denote the resonance absorption dips of the meta-atom. At low input rf flux, the resonance is strong at 19 GHz [62]. In the intermediate rf flux range, the resonance shifts to lower frequency and systematically fades away ($|S_{21}|=$ 0 dB) through the entire frequency range of single-mode propagation through the waveguide. At an upper critical rf flux, a strong resonance abruptly appears at the geometrical resonance frequency $\omega_{geo}/2\pi = 13.52$ GHz for a single rf-SQUID. We employ the nonlinear dynamics of an rf-SQUID in Eq. 2.9 to numerically calculate transmission shown in Fig. 4.8 (c) which shows the same transparency behavior.

We define a normalized transparency level that quantitatively determines the degree of resonance absorption compared to the low rf flux absorption. Under a fixed applied dc flux, the normalized transparency value is defined as a function of

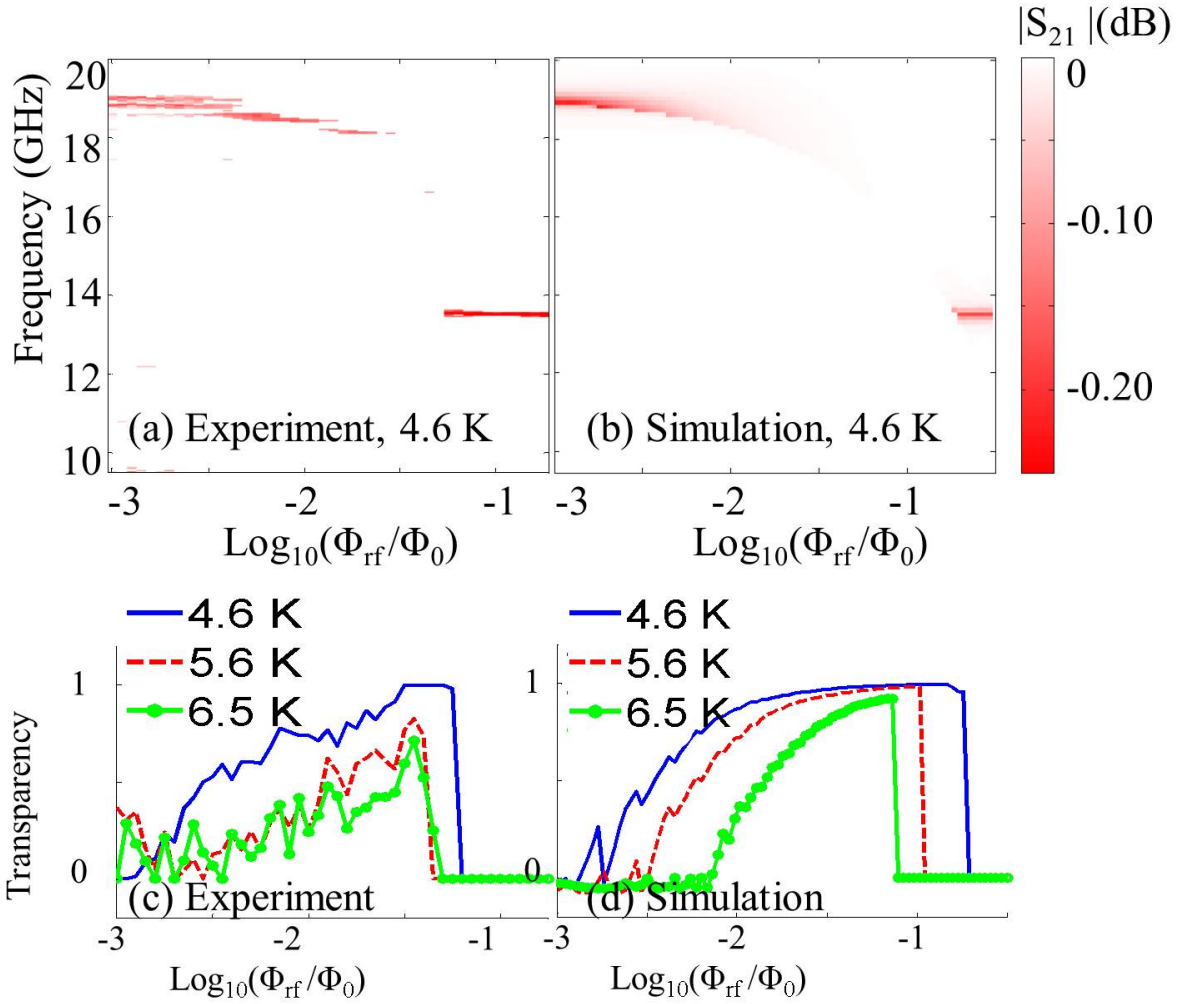

Figure 4.8: Transmission of a single meta-atom at 4.6 K depending on frequency and rf flux is shown in (a) experiment and (b) simulation. Red (dark) feature denotes the resonance dip. (c) and (d) shows the transparency as a function of input power under 4.6 K (solid blue), 5.6 K (dashed red) and 6.5 K (dot line green) both for (b) experiment and (c) simulation.

ϕ_{rf} (Fig. 4.8 and Fig. 4.9):

$$Transparency(\phi_{rf}) = 1 - \frac{|S_{21,res}(\phi_{rf})|(dB)}{|S_{21,res}(0)|(dB)} \tag{4.3}$$

where $|S_{21,res}(\phi_{rf})|$ is the transmission on resonance at a given rf flux, and $|S_{21,res}(0)|$ is the transmission on resonance when the drive amplitude is low ($\Phi_{rf}/\Phi_0 < 0.001$ for the single rf-SQUID meta-atom). High transparency indicates a weak resonance absorption. The extracted transparency shows a clear onset rf flux for transparency and an upper critical rf flux determining the abrupt end of transparency (insets of Fig. 4.8 (b) and (c)). The transparency approaches 1.0 between these rf flux values. The measurements are taken at 4.6 K, 5.6 K, and 6.5 K; at lower temperature, both experiment and simulation show a larger range of transparency as well as a higher degree of transparency.

Collecting rf-SQUID meta-atoms into a metamaterial preserves the self-induced broadband transparency behavior. Fig. 4.9 illustrates the transmission of an 11×11 rf-SQUID array metamaterial with interactions among the meta-atoms. The metamaterial is stimulated at fixed frequency while the rf flux amplitude is scanned under nominally 0 applied dc flux at 4.6 K. The resonance is almost invisible as the input rf flux increases continuously through the transparency range (Fig. 4.9 (a)).

However, a reverse rf flux scan renders an opaque behavior (Fig. 4.9 (b)): the resonance is strong across all rf flux values. Quantitatively, the transparency value reaches 0.9 in the forward sweep and is below 0.3 for the backward sweep (Fig. 4.9 (c)). We did numerical simulations on this metamaterial and they show the same

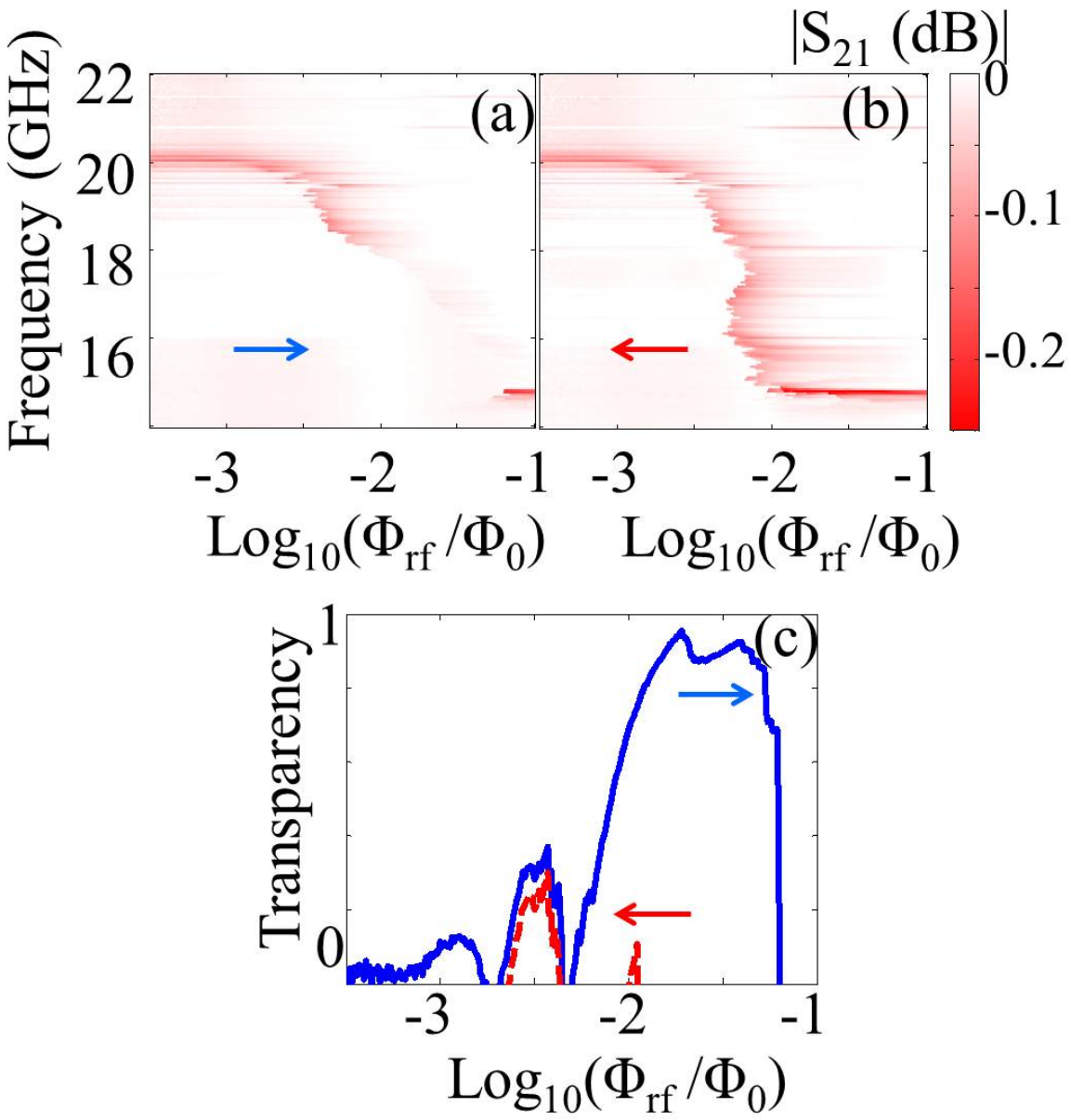

Figure 4.9: Measured transmission as a function of frequency and applied rf flux for an 11x11 array rf-SQUID metamaterial, when the input rf flux (a) keeps increasing, and (b) continuously decreases. (c) Extracted Transparency values for sweep directions (a) and (b). The arrows denote the rf flux scanning directions. The temperature is 4.6 K.

hysteretic transparent/opaque behavior [68]. Similar hysteresis is also observed for simulations of a single rf-SQUID meta-atom. These observations mean that transparency is a robust property of rf-SQUID metamaterials, and can be turned on and off depending on the stimulus scan direction and metamaterial history.

The origin of the nonlinear transparency is the intrinsic bi-stability of the rf-SQUID. The gauge invariant phase difference of the macroscopic quantum wavefunction across the Josephson junction, $\delta(t)$, and its time dependence, determine essentially all properties of the rf-SQUID and the associated metamaterial (see Modeling in Chapter. 2). In simulation, the amplitude of the gauge-invariant phase difference oscillation on resonance as a function of rf flux for a forward stimulus sweep (δ_{LH}) is lower than the amplitude for a reverse sweep (δ_{HL}) above the onset of bi-stability (Fig. 4.10 (a)). The lower gauge-invariant phase difference amplitude results in a smaller magnetic susceptibility and thus a reduction of resonant absorption. The relation between the resonance strength (degree of transparency) and δ_{LH} is shown in Fig. 4.10 (b) for the transparent state. The onset rf flux of transparency coincides with the abrupt reduction of δ_{LH}-Φ_{rf} slope and the onset of bi-stability.

We can apply the Duffing oscillator approximation to analytically predict the onset of bi-stability. For intermediate drive amplitude an rf-SQUID can be treated as a Duffing Oscillator (Kerr Oscillator) [123], which is a model widely adopted for studying Josephson parametric amplifiers [101, 102]. This approximation suggests that when the drive amplitude reaches a critical value, the amplitude of the $\delta(t)$ oscillation as a function of frequency is a fold-over resonance (Fig. 4.11 (a)), creating bi-stable oscillating states (see analysis in Sec. 5.2). The amplitudes of the

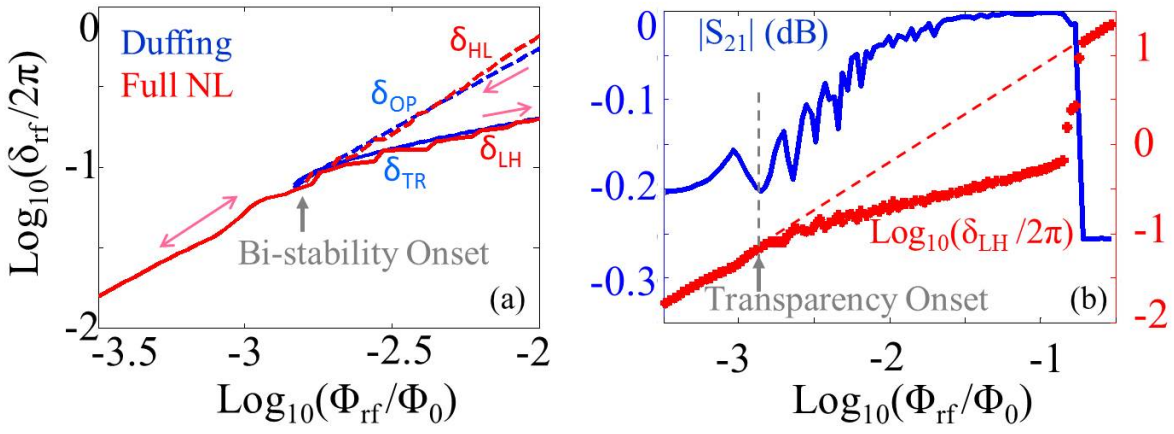

Figure 4.10: Simulation results for a single rf-SQUID. (a) The amplitude of gauge invariant phase $\delta(t)$ oscillation on resonance as a function of driving rf flux amplitude. Red curves denote the full nonlinear numerical results. The δ_{LH} is the amplitude of $\delta(t)$ when the frequency or rf flux scans from low value to high value, and δ_{HL} is the amplitude for a reverse scan. Blue curves are calculated analytically with the Duffing oscillator approximation. The δ_{OP} and δ_{TR} denote the analytic amplitudes for the opaque state and the transparent state respectively. The gray arrow points out the onset of bi-stability. (b) The simulated transmission (blue curve, left y-axis) and the amplitude of $\delta(t)$ (red curve, right y-axis) on resonance as a function of rf flux for the transparent case. The gray arrow shows the onset rf flux for transparency. It is the same as the bi-stability onset.

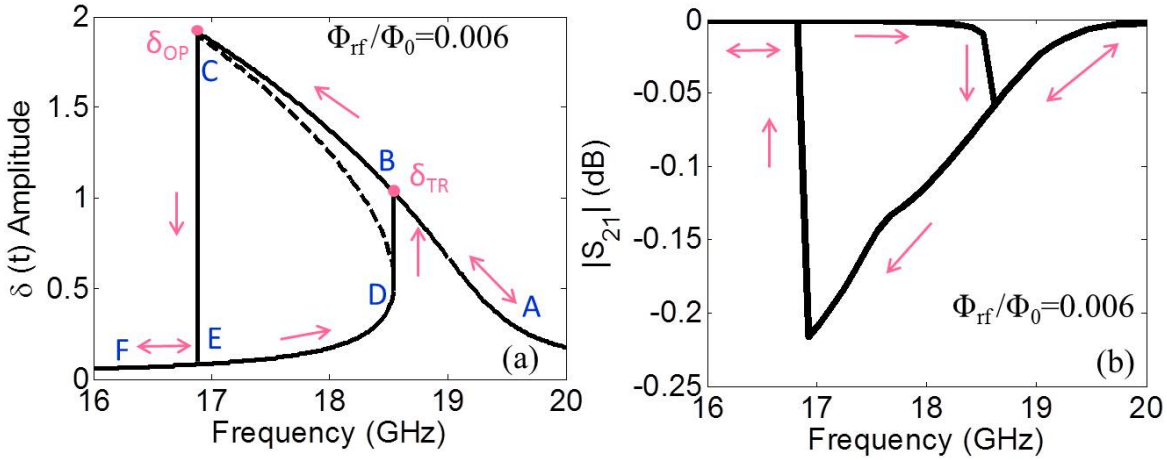

Figure 4.11: (a) The fold-over resonance of the amplitude of $\delta(t)$ calculated in the Duffing oscillator approximation results in a bistable oscillation on resonance with amplitudes δ_{TR} and δ_{OP} respectively at an rf flux of $0.006\Phi_0$. (b) The numerically calculated transmission as a function of rf driving frequency at an rf flux of $0.006\Phi_0$ shows that the frequency range of bistability is the same as analytically predicted in Duffing oscillator approximation in (a).

gauge-invariant phase difference oscillation for the transparent state (δ_{TR}) and the opaque state (δ_{OP}) are calculated analytically for each rf flux, and compared to the amplitudes δ_{LH} and δ_{HL} calculated numerically (Fig. 4.10 (a)). Both the onset of bi-stability and the amplitudes of the two states match very well. The bi-stability of $\delta(t)$ amplitudes explains the bi-stability of transmission observed in experiment and simulation (Fig. 4.11 (b)). The very good agreement between the Duffing oscillator and the full nonlinear numerical simulation allows us to study analytically how to enhance the transparency values and the transparency range.

The onset rf flux value for transparency depends on several parameters. Higher resistance in the junction, higher capacitance, and higher critical current all give a lower onset rf flux for transparency (see analysis in Sec. 5.2). Operating the meta-material at a lower temperature increases the resistance and the critical current, thus decreasing the onset, explaining the modulation of onset by temperature observed in experiment and simulation (insets of Fig. 4.8). The applied dc flux has a more modest effect on the onset rf flux. With a dc flux of a quarter flux quantum, the single rf-SQUID has an onset that is 13% smaller than the 0-flux case (see analysis in Sec. 5.2).

4.3 Strong Resonance in SQUID Meta-atoms and Metamaterials at High rf Drive Amplitude

The dc flux produces a strong modulation in the transparency upper critical rf flux. Above the upper critical rf flux, the rf-SQUID experiences phase slips on

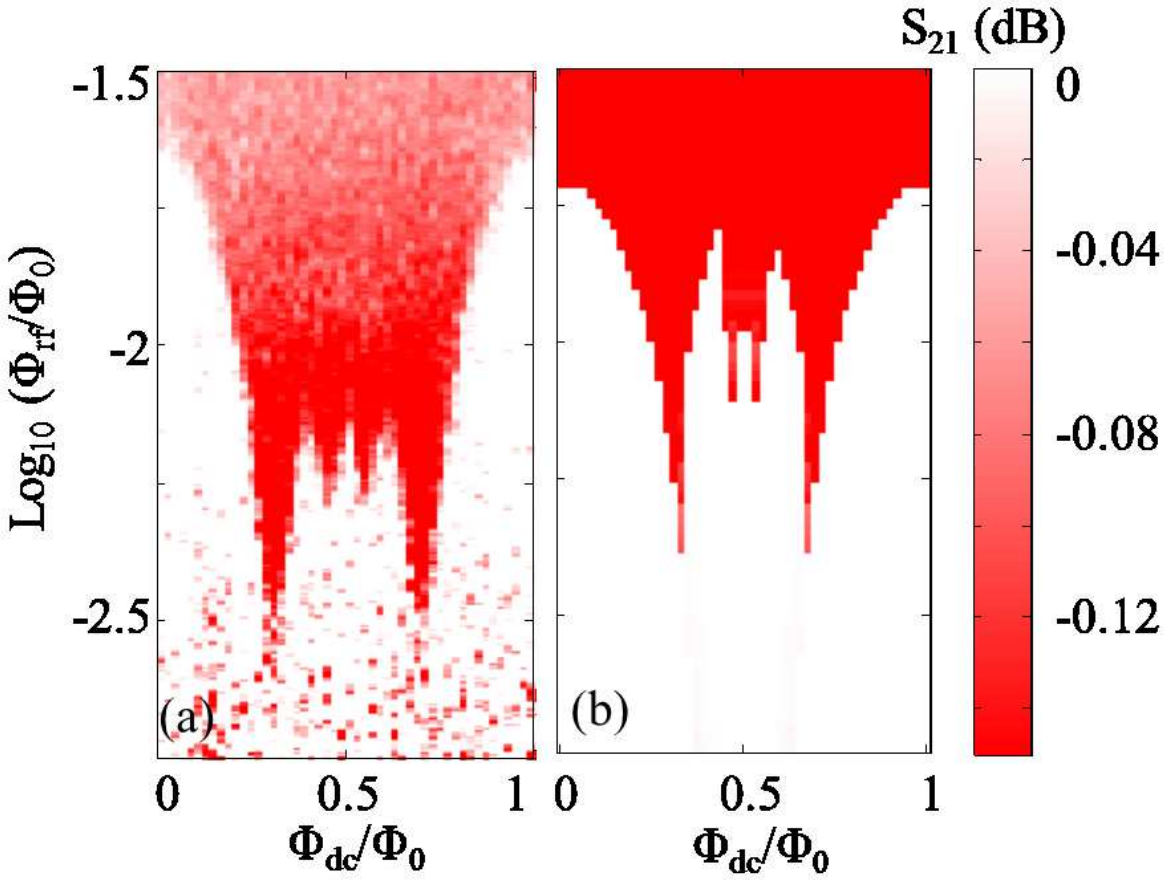

Figure 4.12: The transmission as a function of rf flux and dc flux at the geometrical frequency $\omega_{geo}/2\pi$ of (a) experiment and (b) simulation for a single rf-SQUID at 4.6 K. The strong resonance absorption (red region) at the geometrical frequency determines the upper critical rf flux of transparency. The edge between the red region and the white region denotes the tuning of upper critical rf flux with applied dc flux. The experiment is taken with pulsed rf measurement with a duty cycle of 1% . The pulse width is 2 μs which ensures that the rf-SQUID achieves a steady state. The details of the pulsed rf measurement are in Appendix A.

each rf cycle and shows strong resonant absorption at the geometrical frequency $\omega_{geo}/2\pi$ [63]. We can determine the transparency upper critical edge when the driving frequency is fixed at the geometrical frequency $\omega_{geo}/2\pi$, while rf flux amplitude scans from $0.001\Phi_0$ to $0.1\Phi_0$. The sudden decrease of transmission denotes the upper critical rf flux as a function of dc flux (Fig. 4.12 (a)). The numerical simulation is depicted in Fig. 4.12 (b). There is a tunability of over a factor of 10 in transparency upper critical flux by varying dc flux through the sample. Note that the entire dc magnetic field variation in Fig. 4.12 is only 10 nT. The result shows that at a fixed frequency $\omega_{geo}/2\pi$ the meta-atom can be transparent or opaque depending very sensitively on the rf flux and dc flux.

Also, at a fixed rf flux near the upper critical edge the sample can be resonantly absorbing at ω_{geo} or be transparent in the broadband frequency window depending on the applied dc flux. Fig. 4.13 plots the experimental transmission as a function of dc flux and frequency when our sample is illuminated with an rf flux amplitude of $0.018\Phi_0$ and $0.032\Phi_0$ respectively. Strong absorption at the geometrical resonance appears around $\Phi_0/4$ and $3\Phi_0/4$ dc flux values, while being broad-band transparent near 0 and 0.5 Φ_0. Figure 4.13 (c) shows that higher rf flux values push the rf-SQUID to be opaque under a larger range of dc flux, but the maximum value of transparency is higher than the lower rf flux case (Fig. 4.13 (c)). As the temperature increases, the transparency is weaker, as seen in Fig. 4.13 (d). The tuning of transparency by dc flux at a fixed rf flux indicates again a switchable on/off transparency behavior with dc flux for our meta-atom. The remarkable sharpness of transparency modulation gives an opportunity to use single flux quantum (SFQ)

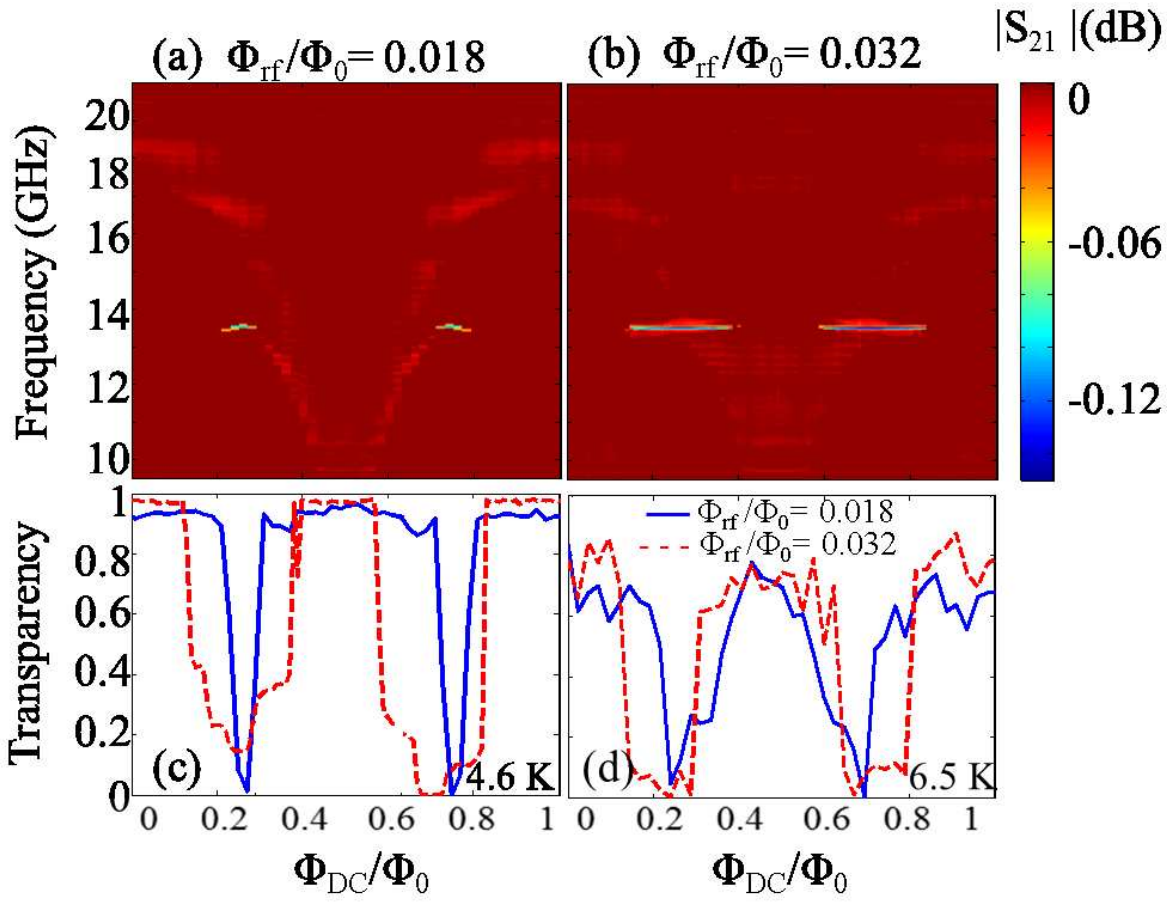

Figure 4.13: The measured transmission at 4.6 K of a single rf-SQUID meta-atom as a function of dc flux and frequency at different drive amplitudes: (a) rf flux= $0.018\Phi_0$, (b) rf flux= $0.032\Phi_0$. Dark red is the perfect transmission background, light red and blue features denote the weak and strong resonance absorption. The extracted transparency values for rf flux amplitude of $0.018\Phi_0$ (red dashed line) and $0.032\Phi_0$ (blue solid line) are shown for (c) 4.6 K and (d) 6.5 K. They both show a clear dc flux-switchable transparency.

logic to achieve fast transparency switching of the rf-SQUID metamaterial [62, 124]. This will enable a range of applications starting from SFQ-modulated digital communication transmitters to energy-efficient wireless data links between low-power cryogenic SFQ electronics and room-temperature semiconductor modules. Both of these applications are difficult to solve by means of conventional low-dissipation superconducting electronics.

Chapter 5: Analytical Models for Understanding Experimental Phenomena

We can make different approximations to equation (2.9), and analytically solve the full nonlinear equation to understand these phenomena, including the dc flux tunable resonant frequency, the broadband transparency behavior, and the strong resonance at the geometrical resonant frequency f_{geo} at high rf flux amplitudes. The gauge invariant phase difference can always be written as the combination of a dc part δ_{dc} and a time-dependent part δ_{rf}: $\delta = \delta_{dc} + \delta_{rf}$, leaving us with the following equation.

$$\frac{d^2\delta_{rf}}{d\tau^2} + \frac{1}{Q}\frac{d\delta_{rf}}{d\tau} + \delta_{dc} + \delta_{rf} + \beta_{rf}(\sin\delta_{dc}\cos\delta_{rf} + \cos\delta_{dc}\sin\delta_{rf}) = (\phi_{dc} + \phi_{rf}\sin\Omega\tau) \tag{5.1}$$

In the following analysis we will focus on how the two parts of $\delta(t)$ vary with various parameters for different levels of rf flux amplitude.

5.1 Linear Oscillator Approximation in Low rf Drive Amplitude

When the drive ϕ_{rf} is small ($\phi_{rf}/2\pi < 0.001$), the oscillation of δ under the small drive will be very weak. Thus, the amplitude of δ_{rf} is also small. We can assume that $\cos\delta_{rf} \approx 1$, $\sin\delta_{rf} \approx \delta_{rf}$ and separate the dc part from the rf part in

Eq. 5.1.

The dc part is only affected by the applied dc flux,

$$\delta_{dc} + \beta_{rf} \sin \delta_{dc} = \phi_{dc} \tag{5.2}$$

Note that δ_{dc} is a measure of the total dc flux in the system since $\delta = 2\pi\Phi_{tot}/\Phi_0 = \phi_{tot}$. Eq. (5.2) describes how the total dc flux in the system responds to the external dc flux depending on the parameter β_{rf}. Since β_{rf} is smaller than one in my experiments, this equation has a single solution for δ_{dc}. Larger β_{rf} will result in multiple solutions for δ_{dc} at a fixed applied dc flux and the response of the SQUID will be hysteretic. For this reason, the rf-SQUID with a larger-than-unity β_{rf} is called a hysteretic rf-SQUID. In our case, we only consider non-hysteretic rf-SQUID ($\beta_{rf} < 1$) which does not show hysteresis upon applied dc flux amplitude scanning, however, it can be hysteretic as the rf flux amplitude increases.

The equation for δ_{rf} from Eq. 5.1 shows a linear oscillator behavior,

$$\frac{d^2\delta_{rf}}{d\tau^2} + \frac{1}{Q}\frac{d\delta_{rf}}{d\tau} + (1 + \beta_{rf} \cos \delta_{dc})\delta_{rf} = (\phi_{dc} + \phi_{rf} \sin \Omega\tau). \tag{5.3}$$

The resonant frequency of this linear oscillator is $\sqrt{1 + \beta_{rf} \cos \delta_{dc}}\, \omega_{geo}$. When $\delta_{dc} = 0$, the oscillator has the highest resonant frequency. When $\delta_{dc} = \pi$, the resonant frequency is lowest. And when $\delta_{dc} = \pi/2$, the system resonates at ω_{geo}. Recall that δ_{dc} is determined through the nonlinear Eq. (5.2). The analytical resonant frequency as a function of applied dc flux fits the experimental results very well (see Fig. 5.1).

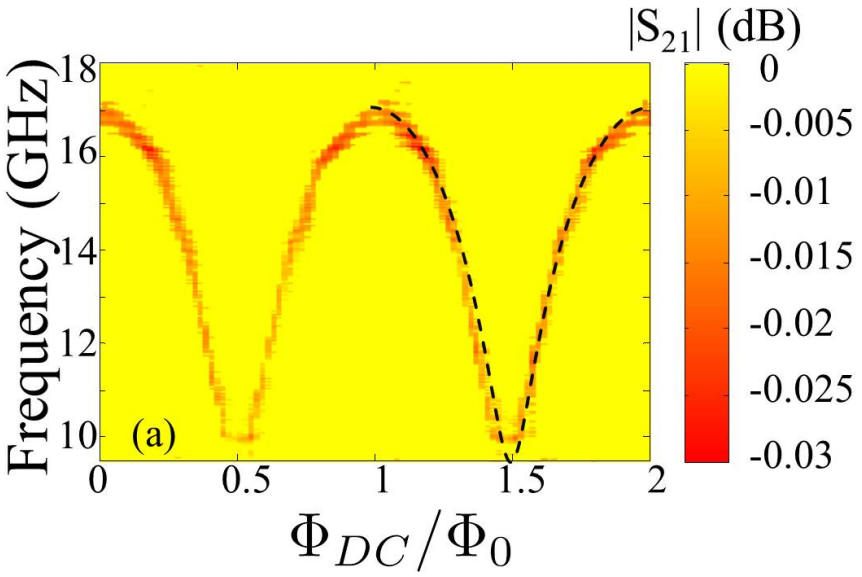

Figure 5.1: Experimental measurements of $|S_{21}|$ of the rf-SQUID meta-atom as a function of frequency and applied dc flux at $0.003\Phi_0$ rf flux and 6.5 K. The calculated analytical resonant frequency is plotted as black dashed lines on top of the figure.

5.2 Duffing Oscillator Approximation Analysis at Intermediate rf Drive Amplitude

As the rf drive amplitude increases, the system is not linear any more. Given that $\sin\delta \simeq \delta - \delta^3/3!$ for small argument, we get the equation of a single rf-SQUID in the Duffing oscillator approximation, which can be solved analytically

$$\frac{d^2\delta}{d\tau^2} + \frac{1}{Q}\frac{d\delta}{d\tau} + (1+\beta_{rf})\delta - \frac{\beta_{rf}}{6}\delta^3 = \phi_{dc} + \phi_{rf}\sin\Omega\tau \tag{5.4}$$

The natural frequency of the oscillating δ when $\phi_{dc} = 0$ is $\omega_0 = \sqrt{1+\beta_{rf}}\omega_{geo}$; it determines the resonant frequency of an rf-SQUID when the drive amplitude is very low. For the single meta-atom at 4.6 K, $\omega_0/2\pi = 19$ GHz. The $-\beta_{rf}/6$

prefactor of the nonlinear term δ^3 will modify the resonance properties when the drive amplitude increases.

We separate the dc and ac parts of $\delta(t)$ for analysis. With the ansatz $\delta = \delta_{dc} + \delta_{rf}$ in equation (5.4), we get two coupled equations for δ_{dc} and δ_{rf},

$$-\frac{\beta_{rf}}{6}\delta_{dc}^3 + (1+\beta_{rf})\delta_{dc} - \phi_{dc} = 0 \tag{5.5}$$

$$\begin{aligned}\frac{d^2\delta_{rf}}{d\tau^2} + \frac{1}{Q}\frac{d\delta_{rf}}{d\tau} + (1+\beta_{rf} - \frac{\beta_{rf}}{2}\delta_{dc}^2)\delta_{rf} \\ - \frac{\beta_{rf}}{6}\delta_{rf}^3 - \frac{\beta_{rf}}{2}\delta_{dc}\delta_{rf}^2 = \phi_{rf}\sin\Omega\tau.\end{aligned} \tag{5.6}$$

The non-zero ϕ_{dc} gives rise to a non-zero δ_{dc}, which adds a δ_{rf}^2 term in the ac gauge invariant phase oscillation. Also, the resonant frequency at low drive with a non-zero dc flux is modified to

$$\omega_1 = \omega_{geo}\sqrt{1+\beta_{rf} - (\beta_{rf}/2)\delta_{dc}^2} \tag{5.7}$$

which is smaller than ω_0 found above.

If we make the ansatz that the long-term response is at the drive frequency, $\delta_{rf} = b\sin\Omega\tau$ [125], we find a cubic equation for the amplitude b^2,

$$b^2[(\epsilon - \kappa b^2)^2 + (\frac{\omega_{geo}}{2Q})^2] = [\frac{(\omega_{geo}^2\phi_{rf})^2}{2\omega_1}]^2 \tag{5.8}$$

where $\epsilon = \omega - \omega_1$ is the difference between driving frequency and the natural frequency, and κ is the anharmonicity coefficient given by:

$$\kappa = -\frac{\beta_{rf}\omega_{geo}^2}{16\omega_1}(1 + \frac{5}{3}\frac{\beta_{rf}\omega_{geo}^2\delta_{dc}^2}{\omega_1^2}) \tag{5.9}$$

The number of real roots of equation (5.8) changes with driving frequency and driving amplitude. When the driving amplitude is very small, equation (5.8) has one real root for b^2 throughout the whole frequency range. The peak value of b denotes resonance. If driving amplitude of the meta-atom increases, the resonance bends towards the lower frequency side, but is still single-valued. After the driving amplitude reaches a critical value $\phi_{rf,bi}$ determined by

$$\phi_{rf,bi} = 2\sqrt{\frac{\omega_1^2}{3\sqrt{3}|\kappa|Q^3\omega_{geo}}}, \tag{5.10}$$

equation (5.8) has three real roots for b^2 in a range of frequencies. The amplitude of the oscillating δ, or the quantity b, is plotted in Fig. (5.3) (a) for an rf flux amplitude larger than $\phi_{rf,bi}$. The middle-value root is unstable [125], so finally we get bi-stability in a certain range of frequencies at a high enough driving amplitude.

With a non-zero dc flux, the oscillating δ now has a dc part, and the natural frequency decreases to ω_1, which further modifies the anharmonicity coefficient κ. Since the onset of transparency predicted by Eq. (5.10) is related the resonant frequency ω_1 and κ, we can tune the onset of transparency by dc flux. For example, with a dc flux of a quarter flux quantum, the single-SQUID has an onset $\phi_{rf,bi}/2\pi$ that is 13% smaller than the 0-flux case.

5.2.1 Transparency Range Tuning

We evaluate the onset Φ_{rf}/Φ_0 of transparency in the Duffing oscillator approximation, and the upper critical Φ_{rf}/Φ_0 by methods discussed in [63]. The two limits of transparency can be tuned by different parameters (Fig. 5.2). Larger critical current I_c increases significantly the upper critical Φ_{rf}/Φ_0, while the higher capacitance and resistance reduce the onset Φ_{rf}/Φ_0 for transparency. The transparency range greatly broadens when any of these three parameters is increased. At lower temperature, the critical current and resistance increase simultaneously, resulting in a wider transparency Φ_{rf}/Φ_0 range. The enhancement of transparency range at lower temperature is consistent with both experimental and numerical results shown in Figs. 4.8 (a) and (b).

5.2.2 Bi-stability of fold-over resonance

In the bi-stability regime, a frequency scan and rf flux amplitude scan both result in hysteretic transparency behavior. The fold-over resonance (Fig. 5.3(a)) predicted in the Duffing oscillator approximation shows that if the driving frequency scans from low to high, the amplitude of δ follows the trace F-E-D-B-A, where the largest amplitude is at point B, denoting the transparent resonance state (δ_{TR}). A reversed frequency scan of trace A-B-C-E-F makes point C the dissipative resonance (δ_{OP}).

The hysteresis in rf flux is similar. Fig. 5.3 (b) plots the bi-stable fold-over resonance of an rf-SQUID meta-atom at drive amplitude $\Phi_{rf}/\Phi_0 = 0.003$ (red curve)

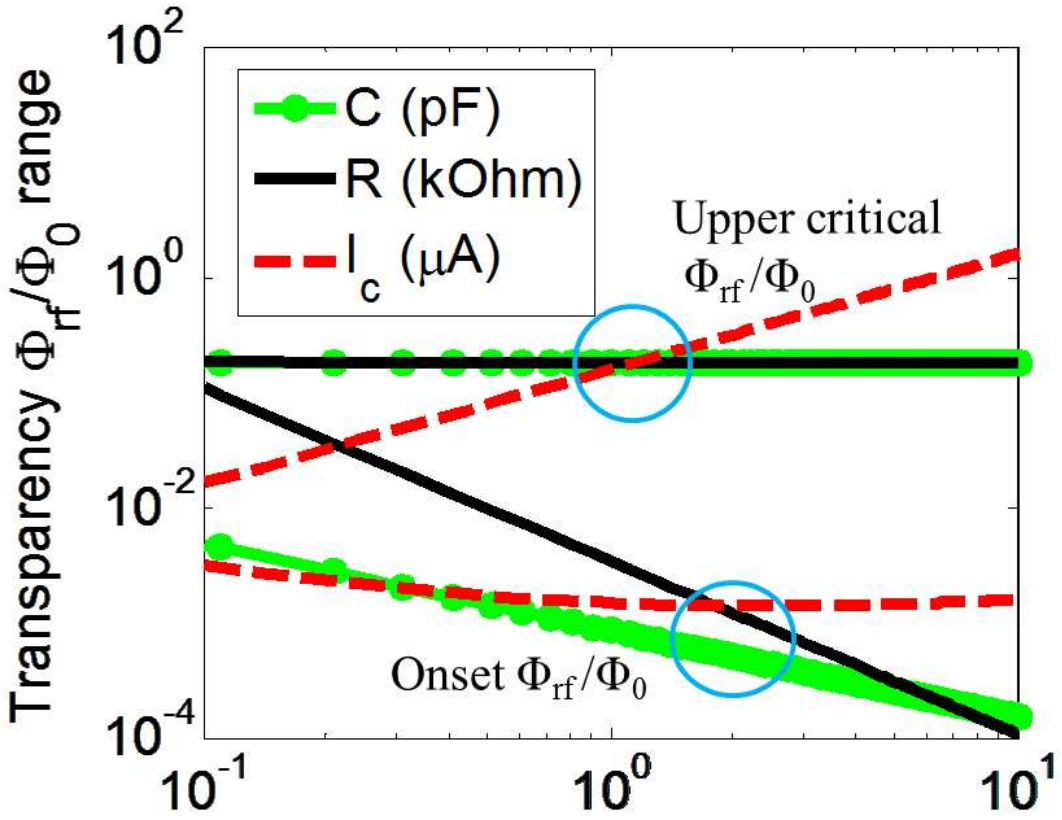

Figure 5.2: The transparency rf flux range tuned by capacitance (green line, $R =$ 1780 ohm, $I_c = 1.15$ μA), resistance of the junction (black solid line, $C = 0.49$ pF, $I_c = 1.15$ μA), and the critical current (red dashed line, $R = 1780$ ohm, $C = 0.49$ pF). In all cases $L = 280$ pH, rf-SQUID inner diameter: 100 μm, outer diameter: 800 μm.

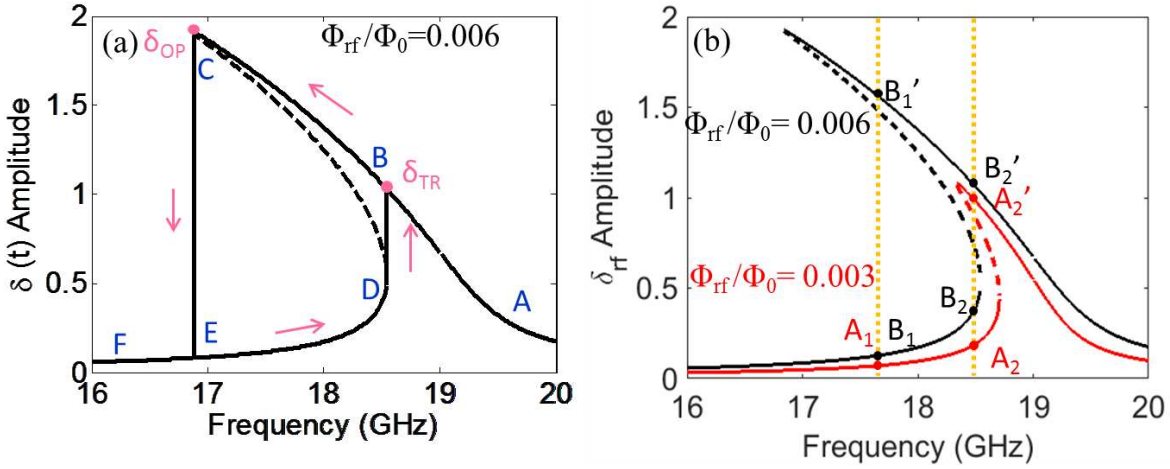

Figure 5.3: The analytically calculated fold-over resonance of an rf-SQUID meta-atom in the Duffing approximation. (a) The fold-over resonance when $\Phi_{rf}/\Phi_0 = 0.006$. The region between B-C-E-D is hysteretic. Depending on scanning direction, the resonance can either happen at point B with amplitude of δ_{TR} or at point C with amplitude of δ_{OP}. (b) The calculated fold-over resonances for two rf flux values: $\Phi_{rf}/\Phi_0 = 0.003$ (red line), and $\Phi_{rf}/\Phi_0 = 0.006$ (black line). Dashed lines denote the unstable state. A_1 (B_1) and A_2 (B_2) are the lower-amplitude roots in the bi-stability regime for $\Phi_{rf}/\Phi_0 = 0.003$ ($\Phi_{rf}/\Phi_0 = 0.006$) case. A_2' is the higher-amplitude root in the bi-stability regime for $\Phi_{rf}/\Phi_0 = 0.003$ at the same frequency of A_2. B_1' and B_2' are the higher-amplitude roots in the bi-stability regime for $\Phi_{rf}/\Phi_0 = 0.006$.

and $\Phi_{rf}/\Phi_0 = 0.006$ (black curve). As the rf flux amplitude keeps increasing at a fixed frequency, in this case 17.6 GHz, the amplitude of δ changes from A_1 to B_1, and stays in the transparent state. However, if the scan starts from very high rf flux value and gradually decreases, the higher amplitude B_1' which denotes the dissipative mode will be excited. Further reducing the rf flux to $\Phi_{rf}/\Phi_0 = 0.003$ brings the rf-SQUID back to the A_1 state. The highest amplitude at a fixed frequency (17.6 GHz) is at B_1 when sweeping rf flux from low to high values, while it is at B_1' for a reverse scan. The same applies for the rf flux amplitude scan at 18.5 GHz: a forward sweep in rf flux amplitude keeps the amplitude of δ in the lower values (A_2 to B_2), while the backward sweep excites δ to oscillate at B_2' and A_2', resulting in a dissipative state.

5.3 Linear Approximation for High rf Drive Amplitude

At even higher drive amplitude ($\phi_{rf}/2\pi > 0.01$), where the rf-SQUID enters the phase-slip state, the Duffing approximation fails. Now the amplitude of δ is much greater than $\sin\delta$, so we ignore the $\sin\delta$ term in Eq. (2.9) to obtain

$$\delta + \frac{L}{R}\frac{d\delta}{dt} + \frac{1}{\omega_{geo}^2}\frac{d^2\delta}{dt^2} = (\phi_{dc} + \phi_{rf}\sin\omega t). \tag{5.11}$$

The dc part now is determined by $\delta_{dc} = \phi_{dc}$ and the rf part is a linear oscillator resonating at ω_{geo}. This explains the high power resonance for a single rf-SQUID meta-atom.

A detailed discussion on the multistability in high rf drive amplitude is also

in section 6.2.4 [63].

Up to this point we have mainly discussed the results for a single rf-SQUID, because the flux-tuning and transparency behavior of the rf-SQUID metamaterial arise from the tunability and bi-stability of single meta-atoms, respectively. Disorder in the rf or dc flux can affect the degree of transparency in an rf-SQUID metamaterial but the effect is quite small. In experiments on an 11×11 array metamaterial, an intentionally introduced dc flux gradient of $0.11\Phi_0$ across the array changes the peak transparency value from 0.94 (for the uniform applied flux case) to 0.91. This suggests the transparency is quite robust against noise and disorder. However, simulation shows that increased coupling between meta-atoms reduces the transparency range [113].

Chapter 6: Multi-tone Response of rf-SQUID Metamaterials

6.1 Intermodulation Measurement

We have shown in previous sections that the rf-SQUID meta-atom and metamaterial are very nonlinear and tunable when responding to dc/rf magnetic field. Nonlinearity also brings in possible frequency mixing when signals composed of more than one frequency are applied. The multi-tone behaviors are explored here using an intermodulation (IM) measurement, where two tones f_1 and f_2 with a small difference in frequency go through the SQUID metamaterial, interact with it, and generate signals at frequency $pf_1 + qf_2$ (IM products) where p and q are integers. I will show results from experimental and theoretical IM studies of rf-SQUID meta-atoms and metamaterials around their tunable and bi-stable resonance [126]. I first focus on the case where two input signals have the same amplitude, as opposed to IM amplification experiments (section 6.2.5) where one tone is much stronger than the other.

In the experimental setup Fig. 6.1 (a), the rf-SQUID array sits in a rectangular waveguide orientated so that the rf magnetic field of the TE mode is perpendicular to the rf-SQUIDs. Before each two-tone experiment, a single-tone transmission experiment is conducted to determine the resonant frequency at which the system

has maximum power absorption. IM products are then measured systematically around the resonance; two signals of frequencies f_1 and f_2 having the same amplitude and a small difference in frequency $\Delta f = f_2 - f_1 > 0$ are injected. The output signal contains the two main tones and their harmonics, as well as IM products.

The two-tone signal is generated from two built-in synthesizers of the network analyzer (Agilent PNA-X N5242A). The output power of the IM signal (up to 99^{th}-order) can be directly measured at the output by the same network analyzer. Using this equipment we can scan either the center tone frequency $f = (f_1 + f_2)/2$, the frequency difference Δf, or the tone powers, and measure the IM power easily and quickly. However our setup does not have the ability to do the phase sensitive measurements in the two-tone experiment; only amplitudes (powers) of the two main tones and IM tones are obtained. In the experiment we usually keep the frequency difference Δf fixed and small ($\leq$ 10 MHz) compared to the 3 dB bandwidth of the resonance dip of SQUID meta-atoms and metamaterials, such that the two tones stay in the resonance dip together.

An example of the generation of an IM spectrum in the metamaterial around resonance (a 27×27 array of rf-SQUIDs) is shown in Fig. 6.1 (b) with $\Delta f = 1$MHz. This spectrum was measured under a fixed tone center frequency and a fixed tone power. The input two-tone signal was from the network analyzer, and the output spectrum was measured by the spectrum analyzer. The noise floor of the spectrum analyzer is around -145 dBm while that of the network analyzer is -110 dBm so it reveals more IM products than the network analyzer above the noise floor. However, the spectrum analyzer measurement is much slower than the measurement of

network analyzer. For measurement of a specific IM product as a function of tone power and center frequency we usually employed the network analyzer.

The output signal at frequency $pf_1 + qf_2$ is called the $(|p|+|q|)^{th}$ order IM. We focus on nearby IM products which are of the $3^{rd}, 5^{th}, 7^{th}, ...$ order. The IM signals generated at nearby frequencies $f_3 = 2f_1 - f_2$ and $f_4 = 2f_2 - f_1$, called the lower and upper 3^{rd} order IM ($f_2 > f_1$), respectively, are of most concern in communications and mixing applications. When the metamaterial is superconducting (measured at $T = 4.6$ K), there is strong IM generation observed above the noise floor up to 51^{st} order. There is no observed IM output when temperature is above the transition temperature,$T_c = 9.2$ K.

The IM spectrum changes considerably as the center frequency and tone power are varied. We mainly examine the modulation of the 3^{rd} order IM power. Again we first search for resonance in a single-tone experiment as the input power varies. In the intermediate power regime, higher input power results in a shift of the resonant frequency to lower values [64], as seen in the purple curve in Fig. 6.2 (a). The 3^{rd} order IM power is then measured with two-tone input around the resonance. Fig. 6.2 (a) shows the upper 3^{rd} order IM power P_{f_4} (colors) generated from a single rf-SQUID meta-atom as a function of the input tone power (horizontal axis) and the center frequency (vertical axis) of the two tones. The IM generation generally follows the resonant frequency curve. Intermodulation is small for low input tone powers (< -80 dBm), with a peak just below the resonant frequency. As the input power increases, the IM generation also increases while shifting to lower frequencies. At the same time a second peak appears above the resonant frequency, forming an IM

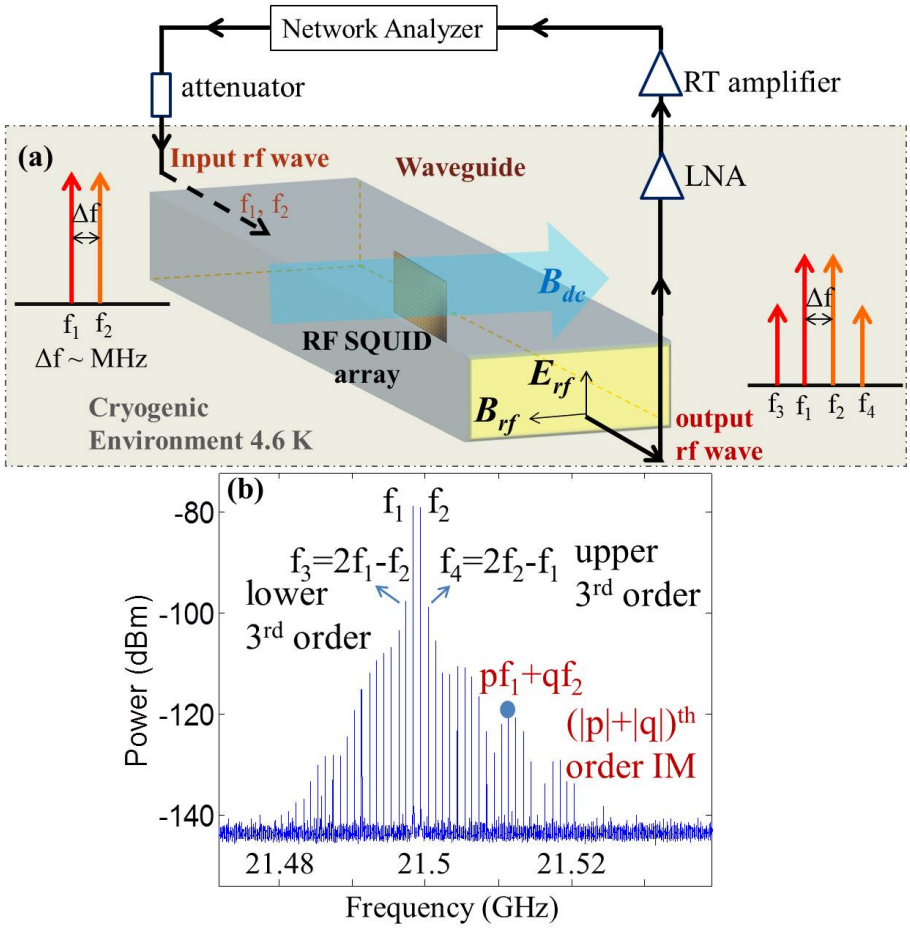

Figure 6.1: (a) The experimental setup for our IM measurements. (b) Experimental measurements of output power from the 27×27 rf-SQUID metamaterial at a temperature of $T = 4.6$ K as a function of frequency when two signals of the same amplitude are injected at a center frequency of 21.499 GHz and a difference frequency of 1 MHz.

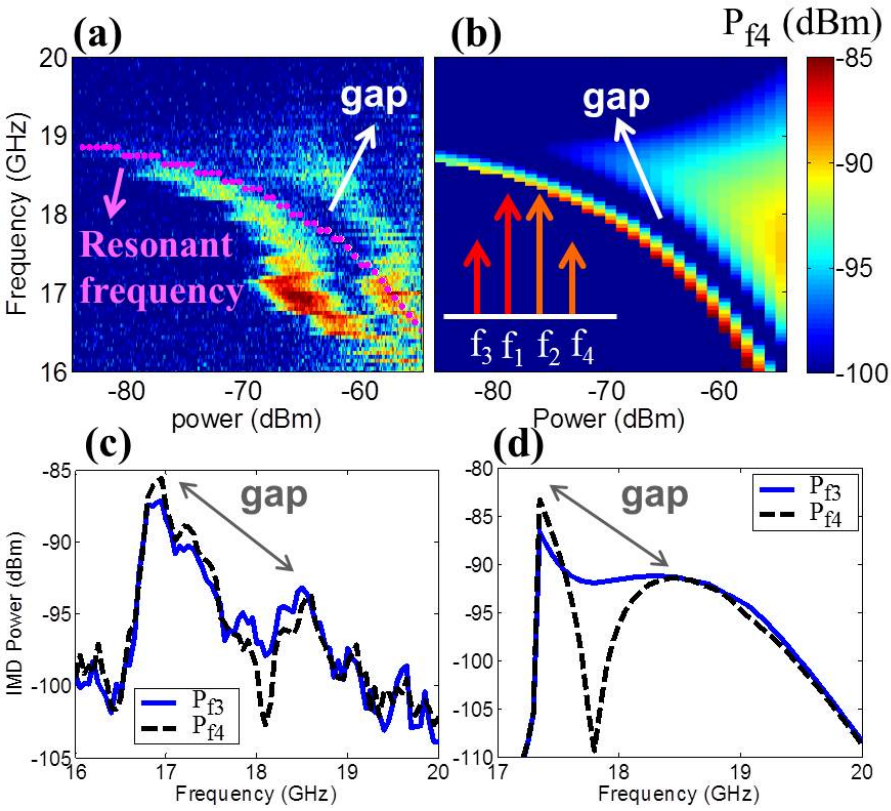

Figure 6.2: The upper 3^{rd} IM power P_{f_4} generated from a single rf-SQUID meta-atom as a function of the applied rf flux and the center frequency of the two tones for (a) experiment and (b) numerical simulation. The purple curve indicates the resonant frequency for a single-tone excitation. The frequency cut for output power at the third IM P_{f_3} (blue solid line) and P_{f_4} (black dashed line) at -65 dBm for (c) experiment and (d) simulation. The spacing between the two input tones is 10 MHz, and the temperature is 4.6 K.

gap where the IM is reduced to nearly the noise level around the resonant frequency. The same phenomenon is observed for a 6×6 array rf-SQUID metamaterial and an 11×11 array rf-SQUID metamaterial. Operating the meta-atom or metamaterial in the gap regime minimizes the 3^{rd} order IM frequency mixing.

Figure 6.2 (c) compares the measured lower and upper 3^{rd} order IM products (P_{f_3} and P_{f_4}) as a function of frequency around the gap feature at -65 dBm. Both IM powers show a sharp onset above the noise level at around 17 GHz, and decrease to a minimum value at 18 GHz, then reach another peak at around 18.4 GHz before dropping continuously at higher frequencies. However, the upper tone P_{f_4} has a higher peak and a substantially lower dip than the lower tone P_{f_3}. This asymmetry between two same-order IM tones was also observed in other SQUID samples and in our numerical simulations. We now wish to explore the origins of the features seen in the data, including the sharp onset and the dip in the 3^{rd} IM generation, as well as the asymmetry between the upper and lower IM output signals.

6.2 Modeling

6.2.1 Numerical Simulation

In this section we explore a simple circuit model that reproduces the effects seen in the previous sections. A single rf-SQUID can be treated as a Resistively and Capacitively Shunted Josephson Junction (RCSJ-model) in parallel with superconducting loop inductance (Fig. 2.1). We assume a uniformly driven and uncoupled SQUID array metamaterial can also be described by the single junction RCSJ-model.

The gauge-invariant phase difference across the junction δ determines the current through the junction $I = I_c \sin\delta$ (I_c is the critical current of the junction). In a closed superconducting loop δ is related to the total magnetic flux inside the loop: $\delta - 2\pi\Phi_{tot}/\Phi_0 = 2\pi n$, where n is an integer, and again $\Phi_0 = h/2e$. Here we can take n to be 0 without loss of generality as shifting δ by 2π leaves the current I unchanged [56]. The voltage across the junction can be written as $V = 2\pi\Phi_0 d\delta/dt$.

The time evolution of the phases is determined by the RCSJ circuit equation [56], obtained by demanding that the total flux through the loop Φ_{tot} is the combination of the dc and rf applied flux ($\Phi_{dc} + \Phi_{rf}(t)$), and the induced flux due to the self inductance L of the loop,

$$\Phi_{tot} = \Phi_{dc} + \Phi_{rf}(t) - L(I_c \sin\delta + \frac{V}{R} + C\frac{dV}{dt}). \tag{6.1}$$

Here, $I_c \sin\delta + V/R + CdV/dt$ is the total current through the loop, which flows through the parallel combination of the junction, shunt resistance R and capacitance C in the RCSJ model. Replacing Φ_{tot} by $\Phi_0\delta/2\pi$ and V by $\Phi_0 d\delta/dt$ in Eq. (6.1) and rearranging terms, we obtain the dimensionless RCSJ equation:

$$\frac{d^2\delta}{d\tau^2} + \frac{1}{Q}\frac{d\delta}{d\tau} + \delta + \beta_{rf}\sin\delta = \phi_{dc} + \phi_{rf}(\tau) \tag{6.2}$$

where $\beta_{rf} = 2\pi L I_c/\Phi_0$, $\phi_{dc} = 2\pi\Phi_{dc}/\Phi_0$, $\phi_{rf} = 2\pi\Phi_{rf}/\Phi_0$, $\omega_{geo} = (LC)^{-1/2}$, $\tau = \omega_{geo}t$, and $Q = R\sqrt{C/L}$.

Typical parameter values are as follows. The inductance, $L = 280$ pH, of

the single SQUID meta-atom is calculated numerically by Fasthenry based on its geometrical structure [127]. Other parameters such as the capacitance, $C = 0.495$ pF, the shunt resistance in the junction, $R = 1780\ \Omega$ (4.6 K), and the critical current, $I_c = 1.15\mu$A, are determined by fitting to the measured geometrical resonant frequency $\omega_{geo}/2\pi = 13.52$ GHz, the measured quality factor $Q = 75$, and the quantity $\beta_{rf} = 0.98$. The quantities ω_{geo}, Q, and β_{rf} were directly measured in previous single-tone transmission experiments. For our setup, the rf flux ϕ_{rf} driving the loop results from the injected rf power inside the rectangular waveguide. Note that the single SQUID meta-atom has an inner diameter of 200μm, and an outer diameter of 800μm. Other meta-atoms in our SQUID metamaterials all have smaller sizes. Thus the rf flux amplitude through the SQUID loop is always much smaller than the flux quantum in the rf power range we consider in this work. Thus, $|\phi_{rf}| < 2\pi$.

The time-dependent functional form of the rf flux is determined by the driving signal. To study intermodulation, the circuit is driven with two tones, which generally can be written

$$\phi_{rf} = \phi_{rf,1}\sin(\Omega_1\tau + \theta_1) + \phi_{rf,2}\sin(\Omega_2\tau + \theta_2) \tag{6.3}$$

where $\Omega_{1,2} = 2\pi f_{1,2}/\omega_{geo}$ and f_1 and f_2 are the frequencies of the two injected signals. Here the two tones have different amplitudes $\phi_{rf,1}$ and $\phi_{rf,1}$, and phases θ_1 and θ_2.

The driving flux can also be written in the form of a complex phasor envelope

modulated by a carrier at the mean frequency $\Omega = (\Omega_1 + \Omega_2)/2$,

$$\phi_{rf,a} = Re[e^{i\Omega\tau - i\pi/2}\phi_e(\tau)] \tag{6.4}$$

where the envelope function $\phi_e(\tau) = \phi_{rf,1}\exp(-i\Delta\Omega\tau/2 + i\theta_1) + \phi_{rf,2}\exp(i\Delta\Omega\tau/2 + i\theta_2)$ and $\Delta\Omega = \Omega_2 - \Omega_1 > 0$ is the difference frequency. For the situation in our experiment, $\Delta\Omega << \Omega$, *i.e.*, the carrier frequency is much greater than the envelope frequency. This will lead to a number of simplifications in the analysis. At present it allows us to argue that the results will not depend on the relationship between the carrier and the envelope phases. Since the relative phase between the carrier and the envelope is unimportant we may shift the time axis in the carrier and the envelope independently. Shifting time in the carrier by $\tau_{sc} = -\Omega^{-1}(\theta_1 + \theta_2)$ and in the envelope by $\tau_{se} = \Delta\Omega^{-1}(\theta_1 - \theta_2)$ removes the phases θ_1 and θ_2 from the problem. Equivalently we can set $\theta_1 = \theta_2 = 0$.

We first consider the case of equal amplitude tones (set $\phi_{rf,1} = \phi_{rf,2} = \phi_s$ to be the amplitude) and set $\theta_1 = \theta_2 = 0$. We then solve Eq. (6.2) for $\delta(\tau)$ using the previously described circuit parameters. Under all circumstances explored here $\delta(\tau)$ is observed to be sinusoidal to a good approximation. Figure 6.3 (c) is an example of the solution to $\delta(\tau)$ at an input power of -65 dBm, with tone frequencies f_1 and f_2 centered around $f = 17.35$ GHz and separated by of $\Delta f = 10$ MHz. The dense blue curves are the fast carrier oscillations and the vertical extreme of the blue represents the slowly varying envelope. More precisely, $\delta(\tau)$ can be represented as in Eq. (4). In this example, the envelope varies on a time scale 3 orders of magnitude longer

than the carrier period. One beat period of the envelope is shown in Fig. 6.3 (c) .

To further investigate IM, we extract the amplitude and phase of δ_i for frequency component f_i via Fourier transform of $\delta(\tau)$. Since magnetic flux is related to δ through $\delta = 2\pi(\Phi_{tot}/\Phi_0)$, we can extract the generated third order IM magnetic flux $\Phi_{3,4}$. The IM flux translates into an IM magnetic field inside the SQUID loop of area A, i.e., $B_{3,4} = \Phi_{3,4}/A$. The excited IM magnetic field transmits through the rectangular waveguide and generates the third order IM powers at the detector. The SQUID is inductively coupled to the waveguide via a coupling coefficient g [128], so only part of the IM power couples to the waveguide mode. The final simulated output IM power is adjusted by varying g ($g \approx 0.015$ for the single SQUID meta-atom), and plotted as a function of center frequency and tone power in Fig. 6.2 (b) for the upper third order IM tone P_{f_4}, with a cut through -65 dBm plotting both lower and upper third order IM powers (P_{f_3} and P_{f_4}) in Fig. 6.2 (d). The cut through the simulated IM power displays a similar sharp onset and gap feature as observed in the experiment, as well as the prominent asymmetry between the two IM tones.

Since δ_i is a surrogate for the output tone power P_{f_i} ($\delta_i \sim \sqrt{P_{f_i}}$) and a direct solution of the nonlinear equation, we use this quantity to analyze the degree of IM generation. Figure 6.3 (a) shows amplitudes of δ_1 to δ_4 as a function of tone center frequency at an input power of -65 dBm, which shows the same asymmetric gap feature. The upper third order IM output δ_4 reduces to nearly zero inside the gap. We plot $\delta(t)$ during one beat period of the input rf signal at the onset center frequency (17.35 GHz) of the abrupt IM generation peak in Fig. 6.3 (c). The $\delta(t)$ envelope stays at a higher amplitude in the first quarter of the signal beat period,

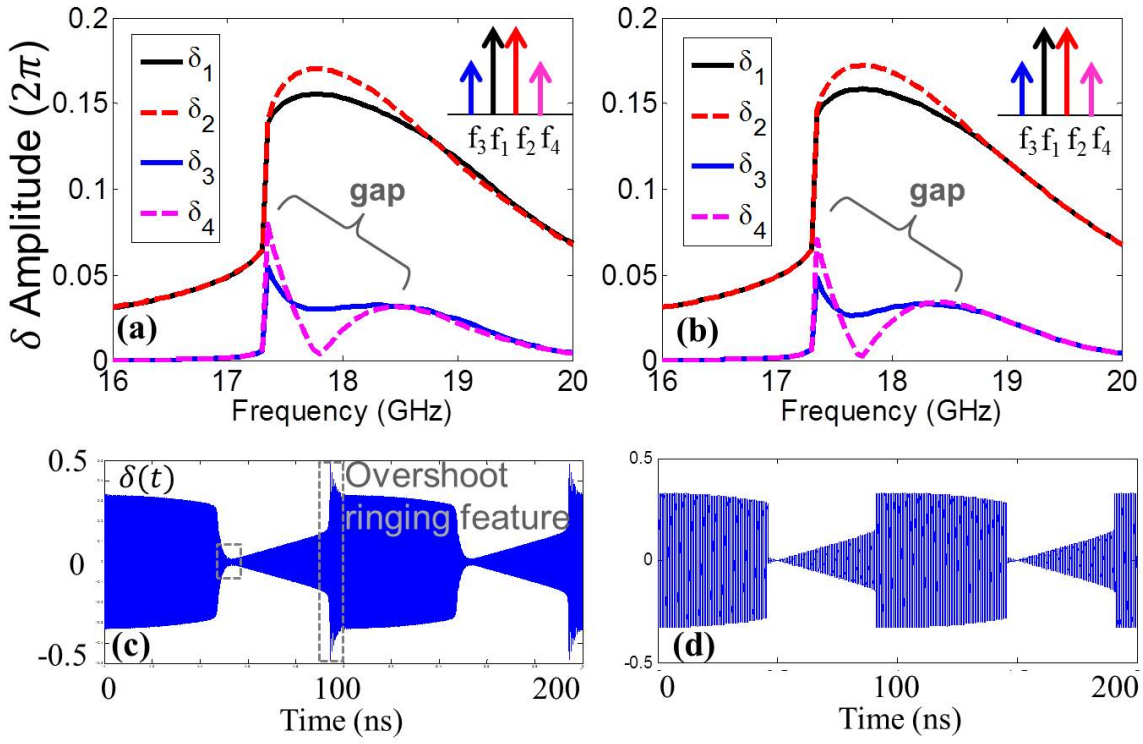

Figure 6.3: The lower and higher main tone output amplitudes δ_1 and δ_2, and third order tones δ_3 and δ_4 for a single rf-SQUID meta-atom at -65 dBm calculated with (a) numerical simulation and (b) analytical model. Plots of $\delta(t)$ over a beat period at 17.35 GHz and -65 dBm calculated by (c) numerical simulation and (d) steady-state analytical model. The dashed boxes in (c) point out the overshooting ringing features in numerical simulation. The spacing between the two input tones is 10 MHz, the temperature is 4.6 K, and the applied dc flux is set to zero.

suddenly decreases to a low amplitude, and gradually increases before it jumps to a higher amplitude again. Note that each abrupt jumps comes with an overshoot feature (labeled as dashed boxes in Fig. 6.3 (c)) with a frequency around 1.5 GHz. The overshoot frequency is intermediate to the fast oscillation (17.35 GHz) and the slow modulations (10 MHz).

6.2.2 Steady-State Analytical Model

In this section we develop an analytical model to understand the phenomena revealed in the experiment and the numerical solutions of the previous sections. We adopt the observation that the gauge-invariant phase $\delta(\tau)$ and the driving flux can be represented as in Eq. (6.4) as a rapidly varying carrier modulated by an envelope. Thus, we insert Eq. (6.4) on the right hand side of Eq. (6.2). We first look for solutions where the time variation of the envelope is so slow that the temporal derivatives of it can be ignored. This leads (after neglecting harmonics of the drive signal, which will be justified below) to a time-dependent gauge-invariant phase difference

$$\delta(\tau) = \bar{\delta} + \tilde{\delta}\sin(\Omega\tau + \theta)$$

where $\Omega = (\omega_1 + \omega_2)/(2\omega_{geo})$ and $\bar{\delta}$, $\tilde{\delta}$ and θ are taken to be constants that depend parametrically on τ through the slow variation of $\phi_{rf}(\tau) = \tilde{\phi}_{rf} = \phi_e$. Here $\bar{\delta}$ and $\tilde{\delta}$ denote the dc part and the slowly varying envelope of δ, respectively, θ is the phase of δ (which can also vary slowly with time).

For the nonlinear term in Eq. (6.2) we have $\sin\delta = \sin[\bar{\delta} + \tilde{\delta}\sin(\Omega\tau + \theta)] =$

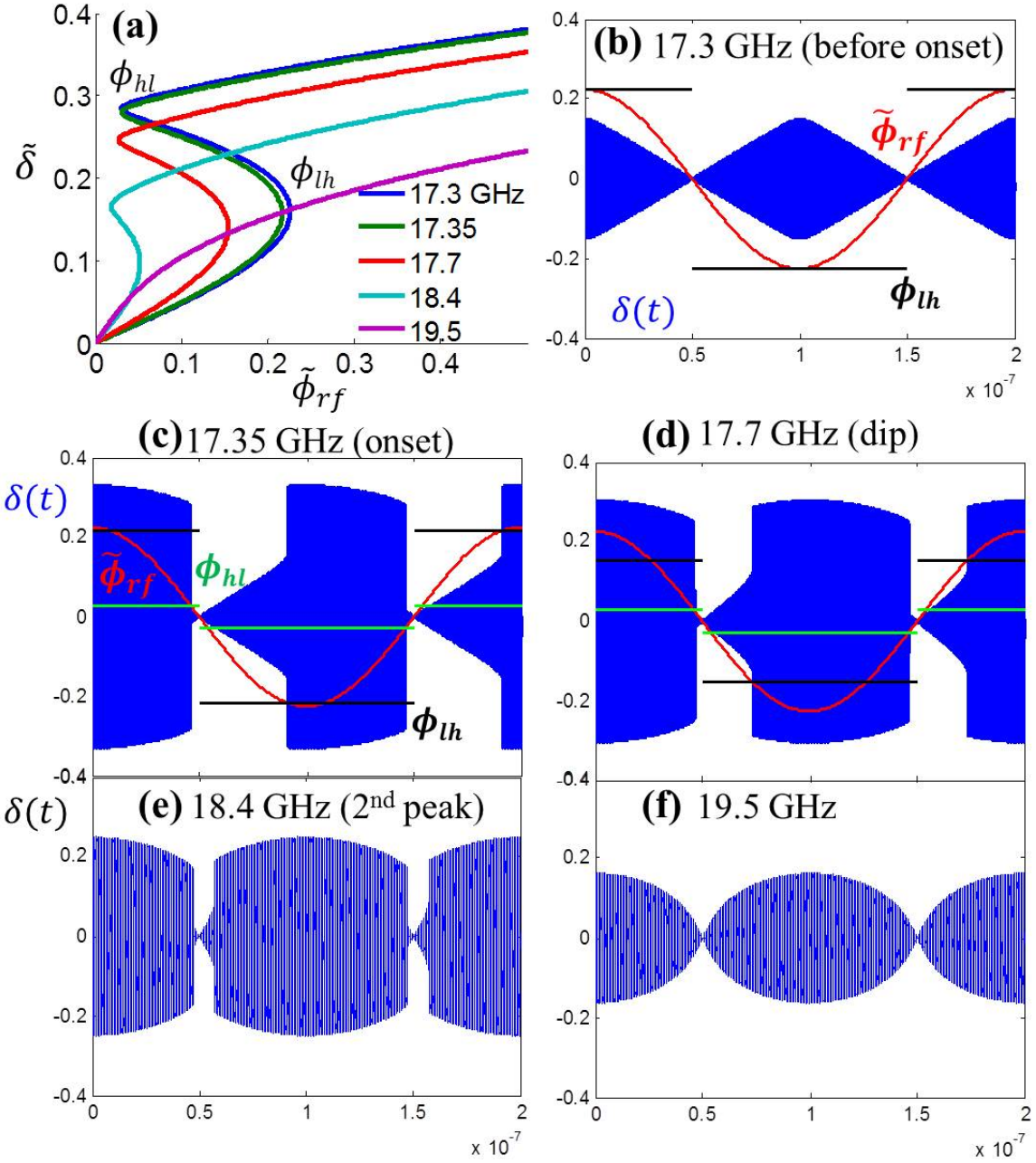

Figure 6.4: Analytical solutions of steady-state model (Eqs. (6.5)-(6.7)) at an rf power of -65 dBm. (a) The relationship between $\tilde{\delta}$ and $\tilde{\phi}_{rf}$ for five remarkable frequencies. ϕ_{lh} denotes the value of rf flux required for transitions of $\tilde{\delta}$ from low to high amplitude solution branch, and ϕ_{hl} denotes the rf flux value for the transition from high to low amplitude solution. (b) to (f): Blue curves represent $\delta(t)$ calculated by the analytical model for (a) 17.3 GHz, right before the onset of strong IM generation, (b) 17.35 GHz, at the onset (c) 17.7 GHz, at the gap (d) 18.4 GHz, at the 2^{nd} peak, and (e) 19.5 GHz, low IM generation. The red curve is $\tilde{\phi}_{rf}$ as a function of time during a beat period. ϕ_{lh} and ϕ_{hl} are marked in the figures as black and green lines. All assume $\phi_{dc} = 0$.

$\sin\bar{\delta}\cos[\tilde{\delta}\sin(\Omega\tau+\theta)] + cos\bar{\delta}\sin[\tilde{\delta}\sin(\Omega\tau+\theta)]$ through a trigonometric identity. In principle this term will contain all harmonics of the carrier, $n\Omega$ $(n = 0, 1, 2, ...)$, and induce harmonics in the gauge-invariant phase difference $\delta(\tau)$. However, higher harmonics in the gauge-invariant phase are suppressed by the second derivative term in Eq. (6.2) (capacitive current). This is confirmed in our numerical solutions where the amplitudes of higher harmonics (components of frequency 2Ω and 3Ω) of δ are at least 2 orders of magnitude lower than the fundamental frequency component. We note that for the examples considered here the dc phase, $\bar{\delta}$, is zero and consequently only odd harmonics are present. We thus neglect these higher order harmonic terms when we expand $\sin[\tilde{\delta}\sin(\Omega\tau+\theta)]$ and $\cos[\tilde{\delta}\sin(\Omega\tau+\theta)]$. As a result, we obtain $\sin\delta \approx \sin\bar{\delta}J_0(\tilde{\delta}) + 2\cos\bar{\delta}J_1(\tilde{\delta})\sin(\Omega\tau+\theta)$ where $J_0(\tilde{\delta})$ and $J_1(\tilde{\delta})$ are Bessel functions. Separating the dc, in-phase, and quadrature components of Eq. (6.2), leads to three coupled equations for the three unknowns ($\bar{\delta}$, $\tilde{\delta}$ and θ),

$$(1-\Omega^2)\tilde{\delta} + 2\beta_{rf}\cos\bar{\delta}J_1(\tilde{\delta}) = \tilde{\phi}_{rf}\cos\theta \tag{6.5}$$

$$\frac{\Omega}{Q}\tilde{\delta} = -\tilde{\phi}_{rf}\sin\theta \tag{6.6}$$

$$\bar{\delta} + \beta_{rf}\sin\bar{\delta}J_0(\tilde{\delta}) = \phi_{dc} \tag{6.7}$$

We construct $\delta(t)$ by solving Eqs. (6.5) - (6.7) to find $\bar{\delta}$, $\tilde{\delta}$, and θ for a given $\tilde{\phi}_{rf}$ and ϕ_{dc}. The relationship between $\tilde{\delta}$ and $\tilde{\phi}_{rf}$ at different frequencies $(f_1 + f_2)/2$ is plotted in Fig. 6.4 (a) for our standard parameter set, $\phi_{dc} = 0$, $Q = 75$, and $\beta_{rf} = 0.98$. The oscillation amplitude $\tilde{\delta}$ as a function of rf flux

amplitude $\tilde{\phi}_{rf}$ is symmetric about the origin, so only positive $\tilde{\phi}_{rf}$ is shown. Figure 6.4 (a) indicates that $\tilde{\delta}$ can be single-valued or multi-valued depending on the fast-oscillation frequency and the slowly-varying envelope amplitude $\tilde{\phi}_{rf}$. For cases where $\tilde{\delta}$ is multivalued, we let ϕ_{hl} and ϕ_{lh} denote the lower and upper critical rf flux values (as labeled in Fig. 6.4 (a)) between which there are three solutions for the oscillation amplitude, $\tilde{\delta}$. When this occurs ($\phi_{hl} < \tilde{\phi}_{rf} < \phi_{lh}$) the middle solution is always unstable and the largest and the smallest solutions are stable. Thus, if $\tilde{\phi}_{rf}$ is in the bistable regime, and $\tilde{\delta}$ is on the lower (higher) stable branch, then, as $\tilde{\phi}_{rf}$ is slowly increased (decreased) through ϕ_{lh} (ϕ_{hl}), the solution for $\tilde{\delta}$ will experience a jump transition from the lower (higher) stable branch to the higher (lower) stable branch.

For two equal amplitude input tones with a fixed center frequency and a fixed tone power, $\tilde{\phi}_{rf}$ is a sinusoidal function with a peak value of $2\phi_s$, and a frequency of $\Delta\Omega/2$, i.e. $\tilde{\phi}_{rf} = 2\phi_s \cos \Delta\Omega\tau/2$.

Figures 6.4 (b) - (f) show the evolution of $\delta(t)$ at different center frequencies (blue), as well as the relationship between the envelopes of the rf flux $\tilde{\phi}_{rf}$ (red curves), the transition rf flux values ϕ_{lh} (black horizontal lines) and ϕ_{hl} (green horizontal lines) for positive and negative $\tilde{\phi}_{rf}$ values during a beat period ($\omega_{geo}\Delta\Omega/2\pi =$ 10 MHz). For tone center frequencies below 17.3 GHz, although $\tilde{\delta}$ is bistable, the envelope of rf flux $\tilde{\phi}_{rf}$ is always below ϕ_{lh}, so $\tilde{\delta}$ remains on the low amplitude branch during a beat period. Above 18.6 GHz, $\tilde{\delta}$ as a function of $\tilde{\phi}_{rf}$ becomes single valued. Both cases give rise to low IM generation.

Between 17.3 GHz to 18.6 GHz, however, the peak value of $\tilde{\phi}_{rf}$ exceeds the upper bi-stable transition rf flux amplitude ϕ_{lh}, while the minimum value of $\tilde{\phi}_{rf}$

is below ϕ_{hl}, so there are four discontinuous jumps in $\delta(t)$ during a beat period. Changing the center frequency from 17.35 GHz to 17.7 GHz makes the solutions for $\tilde{\delta}$ stay on the high-amplitude branch longer (Fig. 6.4 (d)). This is because ϕ_{lh} is smaller for higher frequencies (as seen in Fig. 6.4 (a)), so it is easier for $\tilde{\phi}_{rf}$ to pass the low-to-high transition. The sudden asymmetric state jumps during a beat period generates rich IM products.

We extract the IM components of δ by Fourier transform as discussed for the numerical simulation, and extract the amplitude of two main tones and two third order IM tones of δ, plotted in Fig. 6.3 (b). The analytically calculated amplitudes of IM tones are almost the same as those in the full numerical simulation. However, comparison of time dependent gauge-invariant phase $\delta(t)$ between the full numerical calculation and the analytical calculation in Fig. 6.3 (c) and (d) indicates that the dynamical ringing appears around the state jumps in the full-nonlinear numerical calculation but is not present in the steady-state solutions to Eqs. (6.5) to (6.7). These will be investigated subsequently.

6.2.3 Dynamical Analytical Model

The ringing behavior of $\delta(t)$ during state jumps indicates that the system requires time to transition from one stable state to another. We study this process using a dynamical model for the complex amplitude of the phase $\hat{\delta}$, where $\delta(\tau) = \bar{\delta} + Re[\hat{\delta}(\tau)e^{i\Omega\tau - i\pi/2}]$.

For two equal amplitude input tones, the envelope of the rf flux $\hat{\phi}_{rf} = \phi_e =$

$2\phi_s \cos(\Delta\Omega\tau/2)$ is real. In this case, $\sin\delta$ is expanded as

$$\sin\bar{\delta} J_0(|\hat{\delta}|) + 2\cos\bar{\delta} J_1(|\hat{\delta}|) Re(\hat{\delta} e^{i\Omega\tau - i\pi/2})/|\hat{\delta}|$$

with negligible higher order terms assuming that the higher harmonics of δ are much smaller than the base frequency component. In deriving an equation for the envelope, we adopt the approximations that $Q >> 1$ and that $\hat{\delta}(\tau)$ changes slowly, $|\Omega\hat{\delta}| >> |d\hat{\delta}/d\tau|$. Thus in Eq. (6.2) we replace $d/(Qd\tau)$ with $i\Omega/Q$, and $d^2/d\tau^2$ with $-\Omega^2 + 2i\Omega d/d\tau$. This yields a first-order nonlinear equation for the phasor $\hat{\delta}$ and a transcendental equation for the steady part of $\delta(t)$,

$$i\Omega[2\frac{d}{d\tau} + \frac{1}{Q}]\hat{\delta} + [1 - \Omega^2 + \beta_{rf}\cos\bar{\delta}\frac{2J_1(|\hat{\delta}|)}{|\hat{\delta}|}]\hat{\delta} = \hat{\phi}_{rf} \tag{6.8}$$

$$\bar{\delta} + \beta_{rf}\sin\bar{\delta} J_0(|\hat{\delta}|) = \phi_{dc} \tag{6.9}$$

To analyze the dynamics, we express $\hat{\delta}$ as an in-phase part and a quadrature part, *i.e.* $\hat{\delta} = \delta_R + i\delta_I$, and write the real and imaginary parts of Eq. (6.8). We note that in the absence of losses ($Q \to \infty$) one can construct a Hamiltonian function for the nonlinear system. Including losses we have

$$\frac{d}{d\tau}\delta_R = -\frac{1}{2Q}\delta_R - \frac{\partial}{\partial\delta_I}H(|\hat{\delta}|) \tag{6.10a}$$

$$\frac{d}{d\tau}\delta_I = -\frac{1}{2Q}\delta_I + \frac{\partial}{\partial\delta_R}H(|\hat{\delta}|) \tag{6.10b}$$

where

$$H = \frac{1}{4\Omega}[(1-\Omega^2)|\hat{\delta}|^2] - 2\beta_{rf}\cos\bar{\delta}J_0(|\hat{\delta}|) - \delta_R\hat{\phi}_{rf}$$

is the Hamiltonian. Equilibrium states of the system Eqs. (6.10a) and (6.10b) are the same as those described by Eqs. (6.5) - (6.7). However, we note that the Q-value for our system is quite large, $Q \approx 75$. As a result we look for equilibria of the lossless system, $Q \to \infty$, which are located in the $\delta_R - \delta_I$ plane at the stationary values of the Hamiltonian, $\partial H/\partial\delta_R = \partial H/\partial\delta_I = 0$. Equilibria will be stable if they are at maximal or minimal points of H when $(\partial^2 H/\partial\delta_I^2)(\partial^2 H/\partial\delta_R^2) > 0$. Note that the Hamiltonian is symmetric about $\delta_I = 0$.

In Figs. 6.5 (a) - (c) we plot the Hamiltonian as a function of δ_R and δ_I at a center frequency of 17.35 GHz and -65 dBm tone power, when the rf flux amplitude $\hat{\phi}_{rf}$ is at its peak (0.23), zero (0.0), and negative maximum (-0.23) during a beat period. Figure 6.5 (e) shows a cut through the $\delta_I = 0$ plane, plotting H as a function of δ_R at various rf flux values. In Fig. 6.5 (f) a blow-up of the dashed region is shown that traces the minimum and maximum of H as the rf flux envelope evolves with time. Note that the state transition occurs at an rf flux amplitude of 0.22 for this frequency. When rf flux is zero, the Hamiltonian H is symmetric around the origin, and has a local minimum (stable point) centered at the origin. As the rf flux increases, the $H(\delta_R)$ curve tilts so that the peak located in the positive region of δ_R decreases and moves towards the origin; gradually meeting the dip which moves away from the origin along the δ_R axis. At the same time another peak rises up. As the rf flux value reaches 0.23, the lower peak and the dip between the two peaks

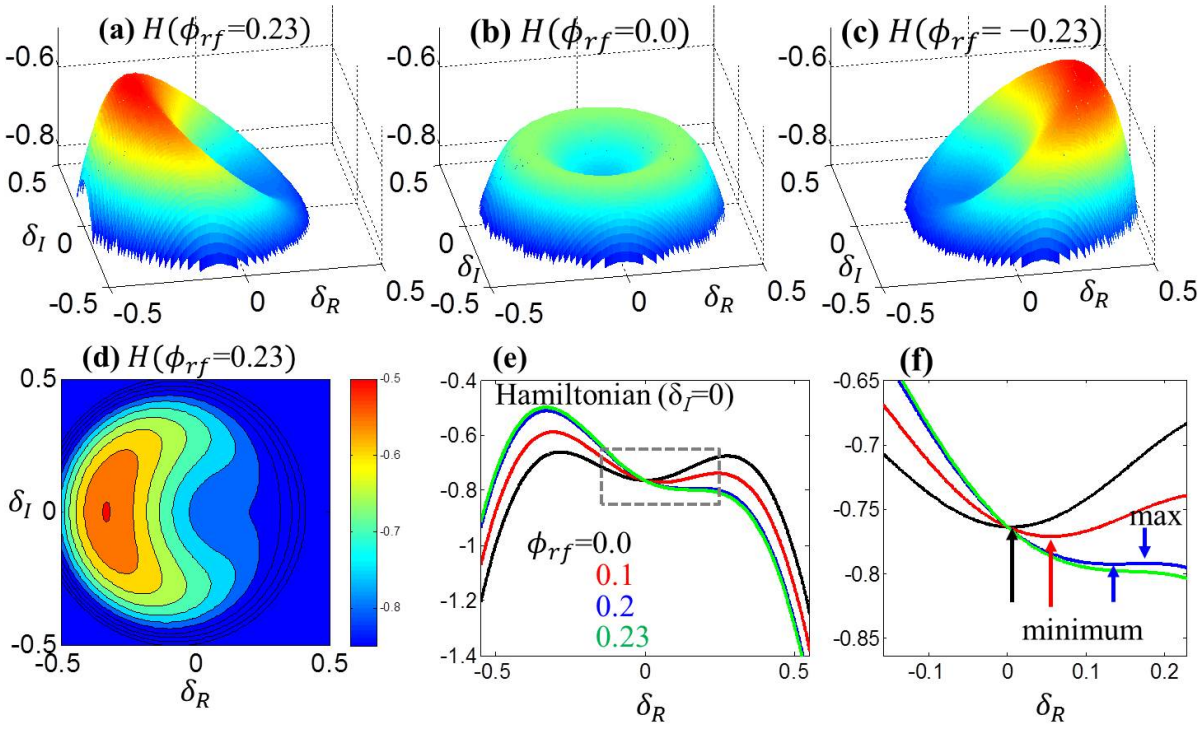

Figure 6.5: The calculated Hamiltonian of a single rf-SQUID as a function of δ_R and δ_I for rf flux amplitudes of (a) 0.23, (b) 0.0, and (c) -0.23. (d) The colormap of the calculated Hamiltonian as a function of δ_R and δ_I for rf flux amplitude of 0.23, with contours from -1 to -0.5 with a step of 0.05. (e) The calculated Hamiltonian as a function of δ_R when $\delta_I = 0$ with different values of rf flux. (f) A zoom-in plot of the dashed box in (e). The transition rf flux value to bistability is around 0.22. All assume a center frequency of 17.35 GHz.

disappear. The system then has to transition to another stable state located at the higher peak in the negative δ_R region. At an rf flux of -0.23, H tilts to the other side (Fig. 6.5 (c)).

Because of the high value of Q, the system's transition trajectory from one stable state to another follows the constant contour lines of the Hamiltonian surfaces in a spiral manner. Figure 6.5 (d) shows the contour lines (from -1 to -0.5 with a step of 0.05) on top of the Hamiltonian colormap at $\hat{\phi}_{rf} = 0.23$.

We can find the trajectory of $\hat{\delta}(t)$ for $\phi_{dc} = 0$ by solving Eq. (6.8) to obtain δ_R and δ_I during a beat period as $\hat{\phi}_{rf}$ changes. Again, we look at the solutions for a center frequency of 17.35 GHz at -65 dBm input tone power. The time trajectory of the phase envelope $\hat{\delta}$ in the δ_R-δ_I plane during the beat period as calculated by the dynamical model is shown in Fig. 6.6 (a). Compare this with Figs. 6.6 (b) and 6.6 (c) which present the $\hat{\delta}$ trajectories extracted from $\delta(t)$ in the full nonlinear numerical calculation and the steady-state model, respectively. Figure 6.6 (a) and (b) are almost identical to each other, serving to validate the dynamical model. In the trajectory plots Fig. 6.6 (a) and (b) we see four colored in-spiraling orbits centered around four corresponding dense regions (red and black dense regions are close to each other near the origin); the dense regions denote the steady-state solutions right after a state jump. We can clearly see these four states in the steady-state trajectory (Fig. 6.6 (c)) labeled as A, B, C and D. The blue dense region in Fig. 6.6 (a) and (b) is the solution at the beginning of a beat period, corresponding to state A. As the rf flux amplitude during a beat period reduces below ϕ_{hl}, the high-amplitude state has to jump to state B (red). For the steady-state solution (Fig. 6.6 (c)),

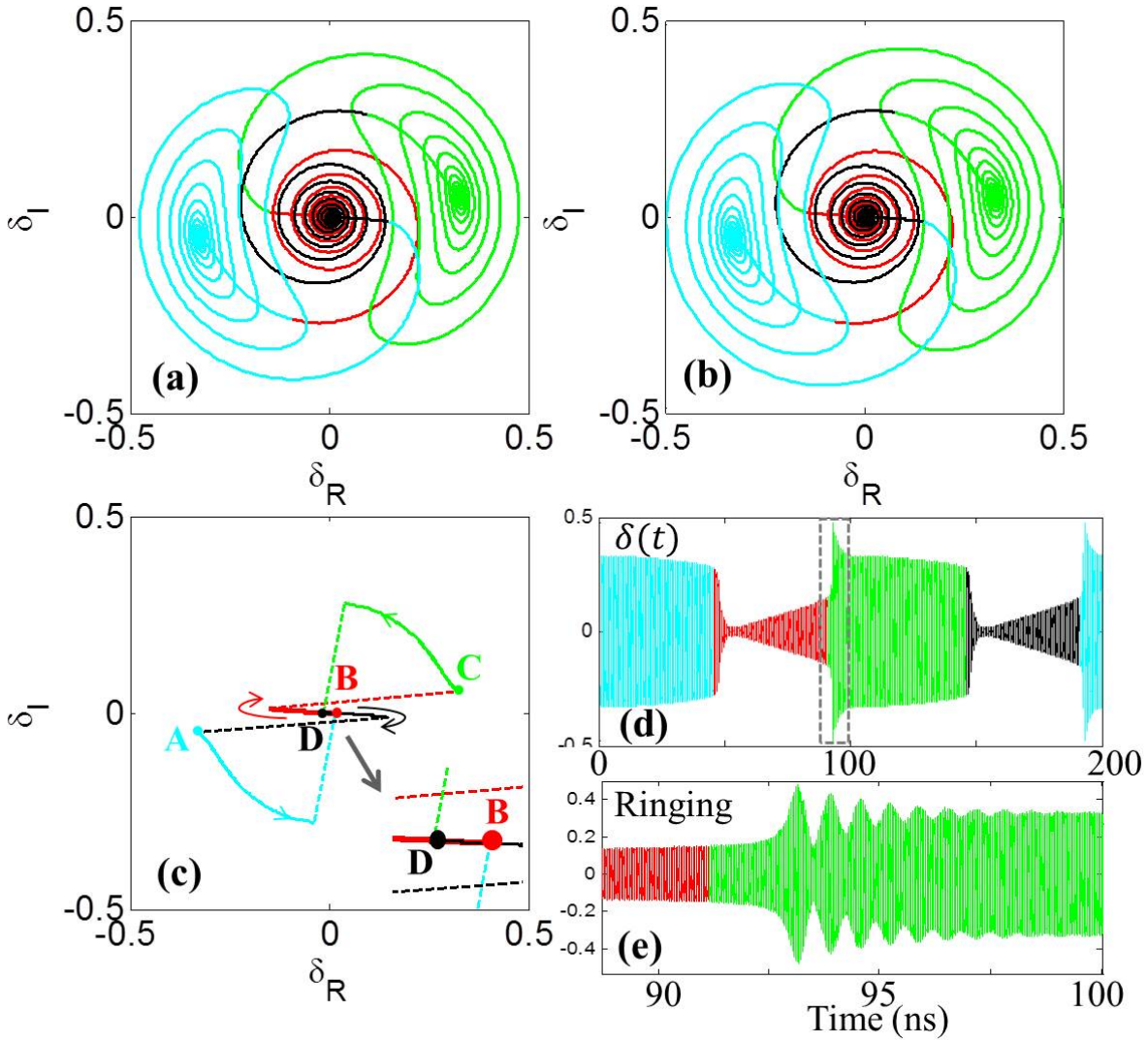

Figure 6.6: The time elapsed trajectories for $\hat{\delta}$(t) for one beat period calculated by (a) the dynamical model, (b) the numerical simulation, and (c) the steady-state model. The inset of (c) zooms in on the trajectory around the origin by five times. (d) shows $\delta(t)$ calculated from the dynamical model, and (e) is a zoom-in of the dashed box in (d) showing the ringing behavior.

the system oscillates in the high-amplitude branch following the blue curve, then directly jumps to state B (red dot). In numerical simulation of Eq. (6.2) and the dynamical model Eqs. (6.10a) and (6.10b) though, the system goes through several orbits before settling down at the low-amplitude stable state B (red dense region) near the origin in the δ-plane. It follows from Eqs. (6.10a) and (6.10b) that the area in phase enclosed by the orbit decreases exponentially at a rate $2/Q$ during approach to the equilibrium point. The boundary between the two colors denotes the time when the system starts to jump to another state.

The in-spiraling orbits during a transition are predicted by the Hamiltonian analysis. The shape of the trajectory before jumping to state A matches the contour lines in Fig. 6.5 (d), except that the trajectory is not symmetric about δ_I axis due to the losses (parameterized by Q) which is not included in the Hamiltonian. The number of trajectory orbits during the transition illustrates the relaxation time of a state jump. The relaxation time also depends on the losses.

Figure 6.6 (d) displays the $\delta(t)$ calculated by the dynamical model; Fig. 6.6 (e) is a zoom-in for the selected region near a state jump. The colors match the colored curves in the trajectory plots Fig. 6.6 (a) to (c). There are very clear ringing features during a jump, which is a reflection of damped spiral orbits. The ringing feature oscillates at a frequency of around 1.5 GHz, and can cause sidebands in the IM spectrum.

In principle the envelope of the generated rf power as a function of time can be measured, which is a surrogate for the gauge-invariant phase $\delta(t)$. Similar to the amplitude-modulated (AM) radio, the fast oscillation can be filtered out by a

nonlinear element, usually a diode, and the output would just be amplitudes of the slowly-varying envelope. Making the frequency difference Δf small allows us to expand the beat period and make it easier to measure the envelope. One concern is that the operating power range of the SQUID meta-atoms and metamaterials is very low. It is hard to see the signal from the diode at such low powers. The method also lacks the ability to measure the ringing between each state jump at a frequency of around 1.5 GHz because the bandwidth of the diode is limited.

6.2.4 DC Flux Dependence of IM generation in SQUIDs

The models all include dc flux as a variable that affects the response of the SQUID. Previous discussions mainly focus on the zero dc flux case. Varying the dc flux value modifies the relationship between the envelope of δ and the envelope of ϕ_{rf} (zero flux case shown in Fig. 6.4 (a)), but it preserves the discontinuous jumps during a beat. Here I explore the effect of non-zero dc flux on the IM generation.

Figures 6.7 (a) and (b) shows the measured lower 3^{rd} IMD power generated from a single rf-SQUID meta-atom as a function of center frequency and tone power, under applied dc flux $\phi_{dc}/2\pi$ of 0 and 0.3, respectively. Again, the spacing between the two input tones is 10 MHz, and the temperature is 4.6 K.

At low input tone powers (< -80 dBm), the non-zero dc flux case has a IM power peak when the two tones are centered at 16 GHz. The center frequency for the IM peak is 3 GHz less than the 0 dc flux case. In the intermediate power range, the IM gap feature also appears at non-zero dc flux. At higher input tone powers, the

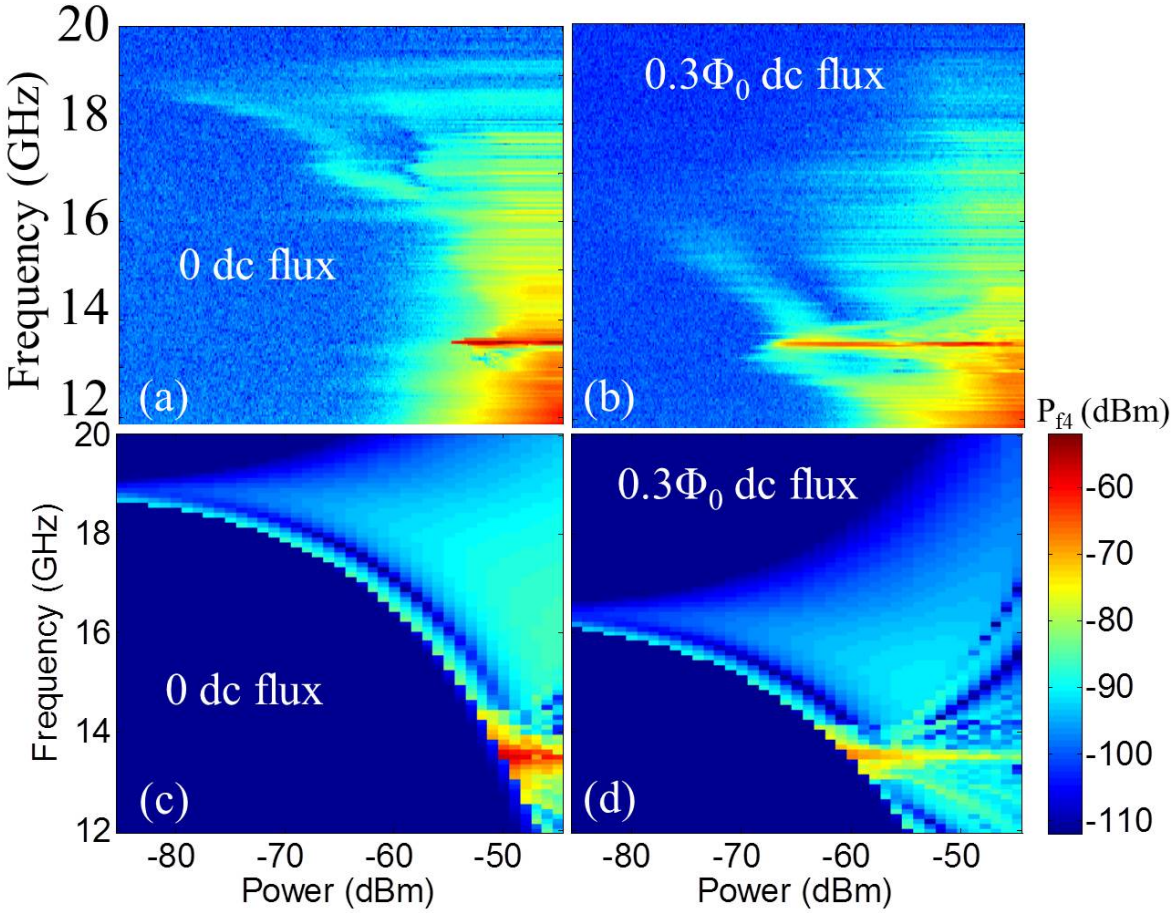

Figure 6.7: The measured lower 3^{rd} IMD power generated from a single rf-SQUID meta-atom as a function of center frequency and tone power, under applied dc flux $\phi_{dc}/2\pi$ of (a) 0, and (b) 0.3. The same quantity calculated by numerical simulation under applied dc flux $\phi_{dc}/2\pi$ of (c) 0, and (d) 0.3. The spacing between two inputs is 10 MHz. The temperature is 4.6 K. Four plots share the same colorbar.

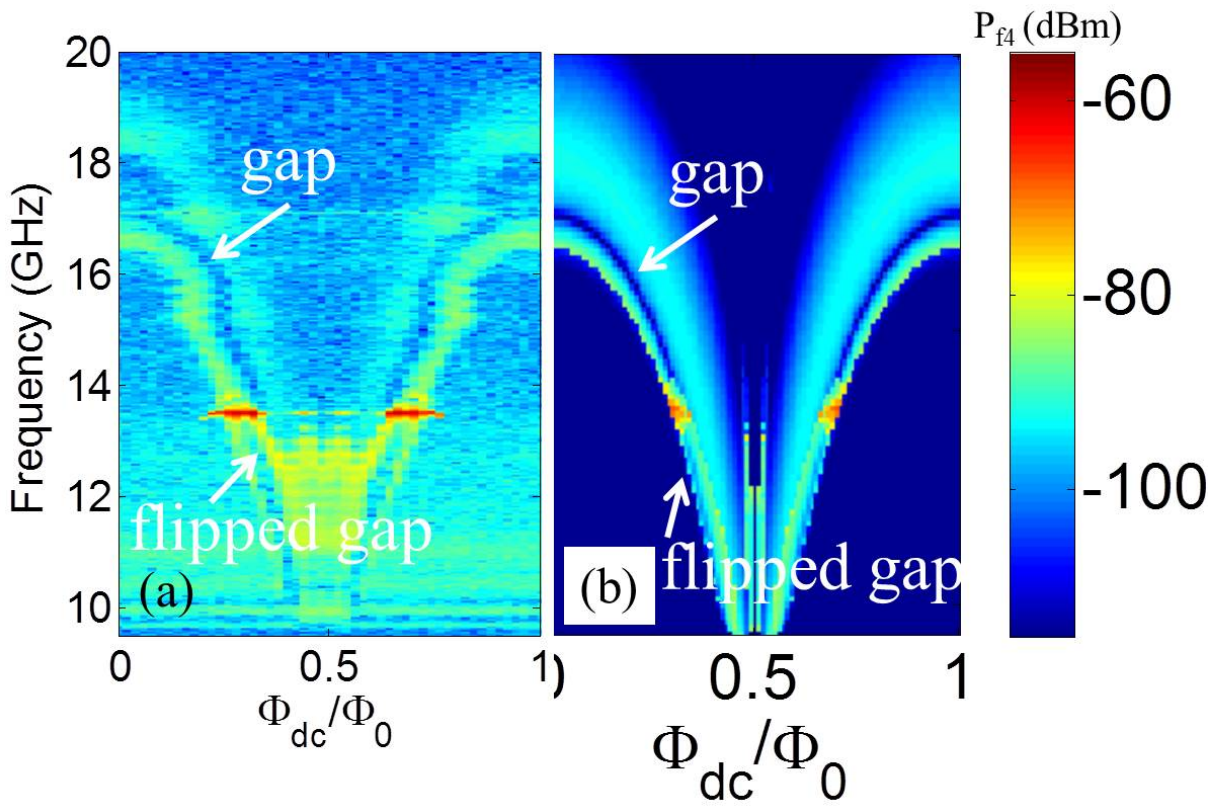

Figure 6.8: The (a) measured and (b) simulated upper 3^{rd} IM power P_{f_3} generated from a single rf-SQUID meta-atom P_{f_4} as a function of tone center frequency and the applied dc flux at a fixed rf power -60 dBm. The spacing between two inputs is 10 MHz. The temperature is 4.6 K. Note that in the simulation only IM powers at the dc flux values from 0 to $0.5\Phi_0$ are calculated, and then mirrored about the $0.5\Phi_0$ dc flux to generate results from $0.5\Phi_0$ to Φ_0. The experiment is taken from a dc flux range 0 to Φ_0.

IM power becomes very strong at the geometrical resonant frequency because the SQUIDs are multistable there. The critical tone power for the strong IM products at the geometrical resonant frequency changes from -50 dBm to -70 dBm as the dc flux value changes from 0 to $0.3\Phi_0$. The upper IM power P_{f_4} is calculated using the full nonlinear model for the single rf-SQUID meta-atom under two dc flux values. The calculated responses show similar behavior as in experiment. (Fig. 6.7 (c) and (d)).

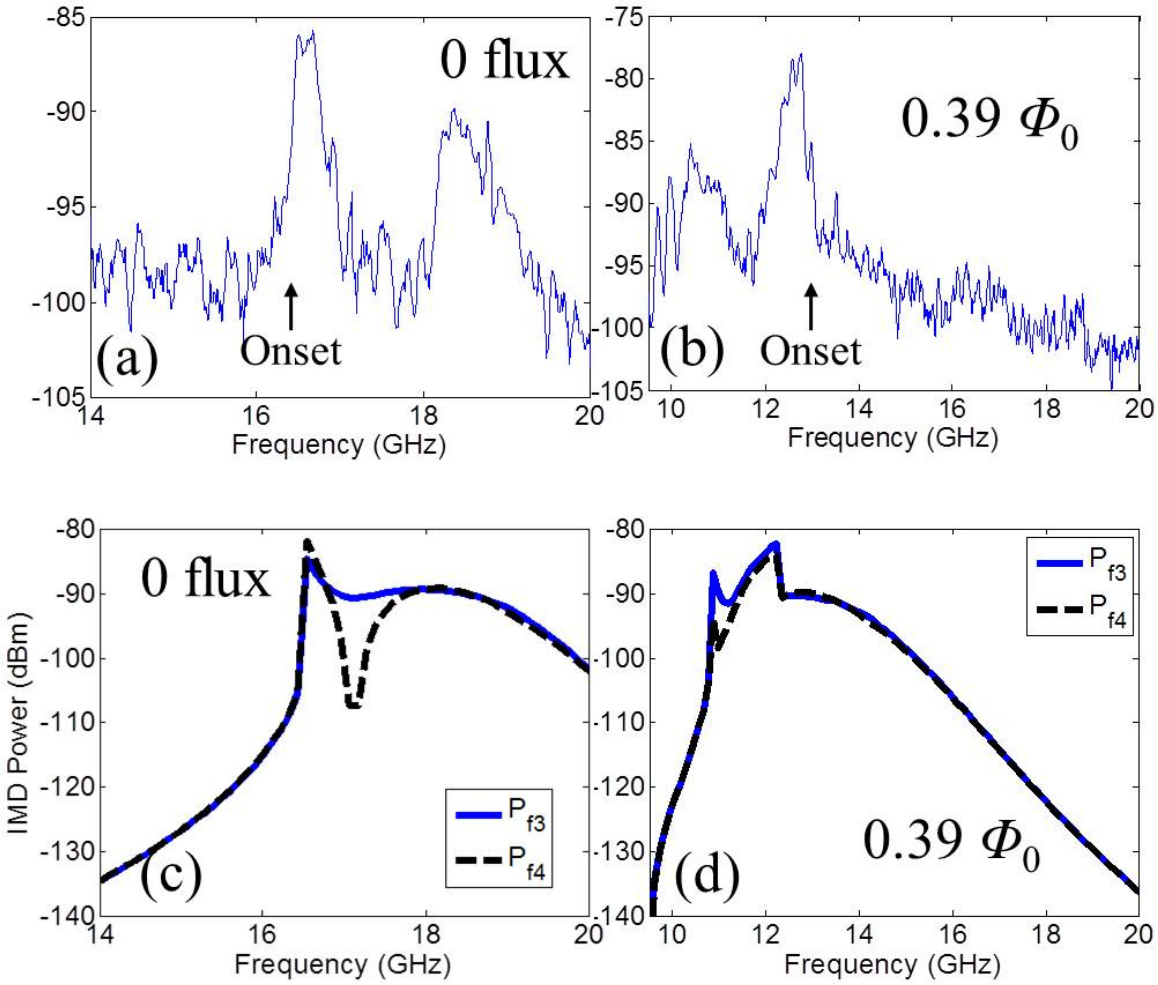

Figure 6.9: The measured upper 3^{rd} IM power P_{f_3} generated from a single rf-SQUID meta-atom. IM power P_{f_3}as a function of the tone center frequencyat a fixed rf power -60 dBm, and at (a) 0 dc flux, and (b) $0.39\Phi_0$ dc flux. (c) and (d): Same quantities as in (a) and (b), calculated by the full nonlinear numerical simulation. The spacing between two inputs is 10 MHz. The temperature is 4.6 K.

Next I explore how the IM gap changes with the applied dc flux. Figure 6.8 (a) shows the IMD power at a fixed input rf power (-60 dBm) as a function of frequency in varying dc flux. The gap width and frequency are tunable in almost all dc flux ranges except at the dc flux values with the strongest IM signals at the geometrical resonant frequency (around $0.3\Phi_0$). The gap, tuned smoothly from 0 to 0.3 Φ_0 dc flux, breaks as it reaches the geometrical resonant frequency f_{geo}, then "flips" and modulates smoothly with dc flux again below f_{geo}. Two frequency cuts at 0 and 0.39 Φ_0 dc flux in Fig. 6.9 (a) and (b) clearly reveal the flipped gap feature. At 0 dc flux the peak value of IM products is at the lower frequency side of the gap. At 0.39 Φ_0 dc flux however, the IM generation is strongest above the gap. The same quantities are calculated by numerical simulation and shown in Fig. 6.8 (b) and Figs. 6.9 (c) - (d) for comparison. The simulation also shows a flipped gap feature.

This flipped gap feature can be explained by the steady-state relationship between the envelope of the gauge-invariant phase δ and ϕ_{rf} (solutions to Eqs. 6.5 to 6.7), which changes with dc flux. Figures 6.10 (a) and (b) show this relationship for two dc flux values. Curves in various colors denote different center frequencies of the two excitation tones. At zero flux, the function is bistable around the gap regime. Higher center frequencies results in smaller upper critical rf flux value ϕ_{lh}. For a flux value close to 0.5 Φ_0 though, the upper critical rf flux value ϕ_{lh} is larger for higher center frequencies around the gap regime (10 - 13 GHz) - exactly opposite to the 0 dc flux case.

I extract the upper critical rf flux value ϕ_{lh} as a function of tone center frequency in blue when $\phi_{dc}/2\pi$ equals zero and 0.47, and plot them in Figs. 6.10

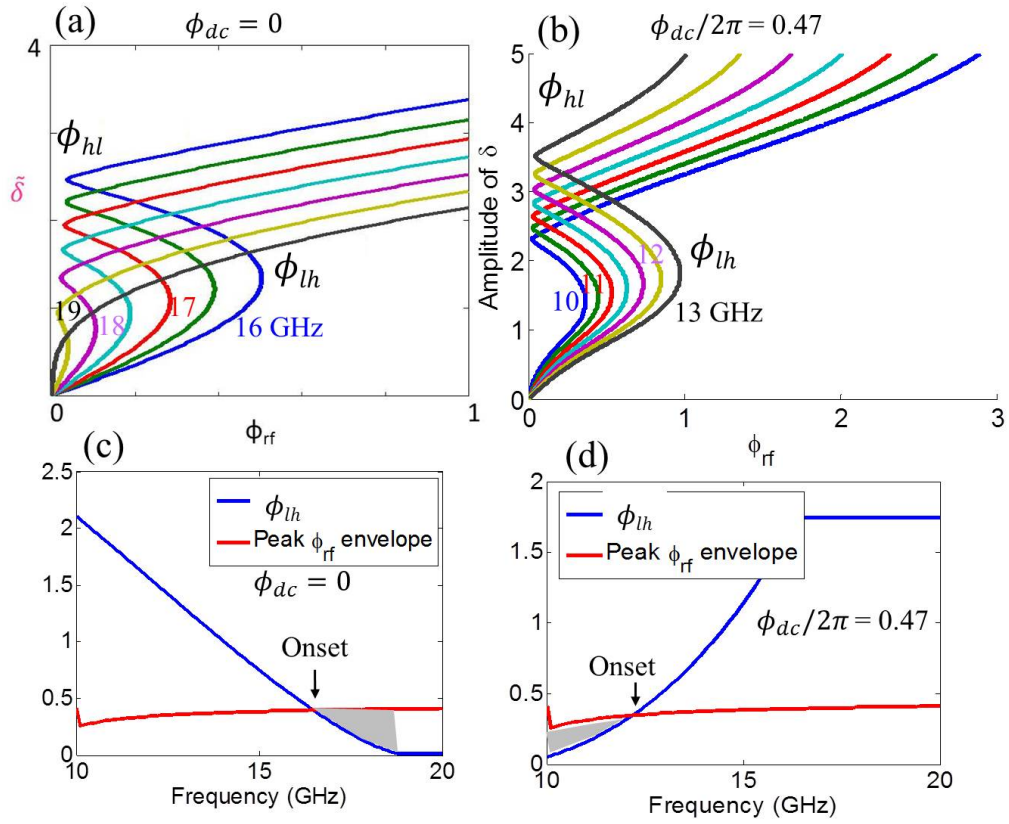

Figure 6.10: The extracted amplitudes of two main tones (δ_1 and δ_2) and two third IM tones (δ_3 and δ_4) from steady-state solutions $\delta(t)$ under (a) $\phi_{dc}/2\pi = 0$, and (b) $\phi_{dc}/2\pi = 0.47$. The upper critical rf flux value ϕ_{lh} (blue curves) and the peak value of rf flux envelope (red curves), as a function of tone center frequency at (c) 0 dc flux, and (d) $0.47\Phi_0$ dc flux. Gray areas denote the conditions for discontinuous jumps. The rf power is -60 dBm. The spacing between the two tone inputs is 10 MHz. The temperature is 4.6 K.

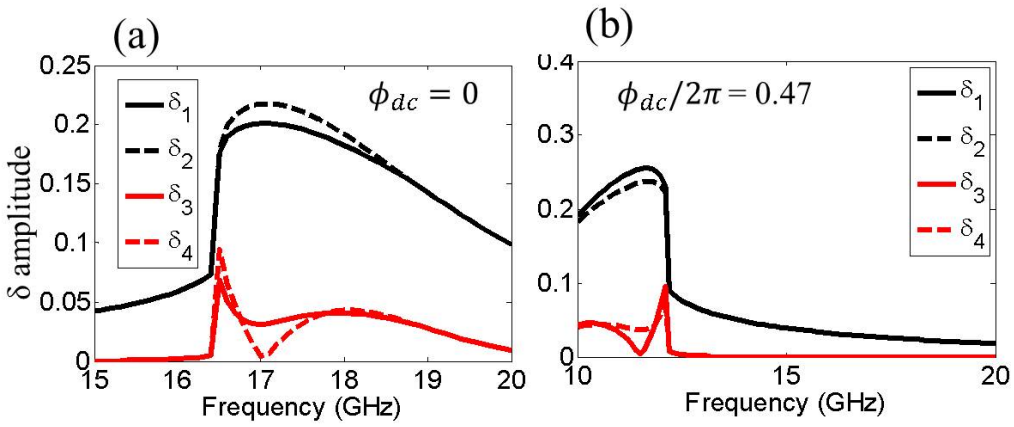

Figure 6.11: The calculatedamplitudes of two main tones (δ_1 and δ_2), and two third IM tones (δ_3 and δ_4) extracted from $\delta(t)$ by solving steady-state analytical model Eqs. (6.5) - (6.7), under (a) 0 dc flux, and (b) $0.47\Phi_0$ dc flux value.

(c) and (d), respectively. Also plotted is the peak value of rf flux envelope which slightly varies with frequency, because the rf magnetic field is related to rf power as well as the propagation constant inside the rectangular waveguide. From previous sections we know that when the peak value exceeds the non-zero critical rf flux value, the envelope of δ will experience four state jumps during a beat period. Gray areas denote the conditions for discontinuous jumps. Switching from no state jump to abrupt state jumps (where the state amplitude change is large) determines the richest IM generation. The switch happens at the lower and higher tone center frequency side for 0 and 0.47 Φ_0 dc flux, respectively (Figs. 6.10 (c) and (d)). This difference is consistent with the flipped gap feature observed in experiment.

Figure 6.11 shows the amplitudes of $\delta(t)$ at the two main tones, and two third IM tones extracted from $\delta(t)$ by solving the steady-state analytical model Eqs. (6.5) to (6.7). The calculated gap feature also flips as the dc flux value approaches 0.5 Φ_0, consistent with the experiment.

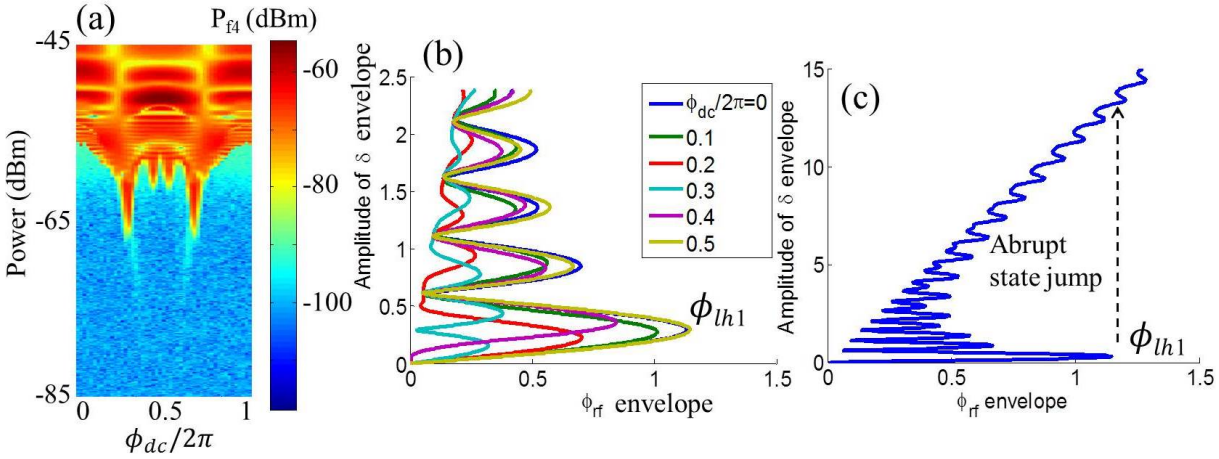

Figure 6.12: (a) The measured upper 3^{rd} IMD power generated from a single rf-SQUID meta-atom as a function of dc flux and tone power, at a tone center frequency of 13.54 GHz, just above the geometrical resonance frequency (13.52 GHz). (b) The steady-state relationships between envelope of δ versus envelope of rf flux at a center frequency of of 13.54 GHz; the dc flux modulates from 0 to 0.5 Φ_0. (c) Larger scale of (b) for 0 dc flux. The spacing between two inputs is 10 MHz. The temperature is 4.6 K.

Another effect brought on by non-zero dc flux is the change of the critical rf power for the strong IM generation around the geometrical resonant frequency at high rf drive amplitudes. The upper third order IM power shown as colors in Fig. 6.12 (a) is measured at a tone center frequency of 13.54 GHz (just above the geometrical frequency 13.52 GHz) with $\Delta\omega/2\pi = 10$ MHz, while the rf flux scans from low to high amplitudes, in different applied dc flux values. The red region denotes the strong IM power. The unique horizontal stair-like features are a characteristic of multistability [59, 63] .

Figure 6.12 (b) shows the steady-state relationships between the envelope of δ versus the envelope of rf flux at a tone center frequency of 13.54 GHz; the dc flux modulates from 0 to 0.5 Φ_0 in steps of $0.1\Phi_0$. All curves are calculated by Eqs. (6.5) - (6.7) reveal multistable solutions. The critical rf flux envelope value for

one stable state to jump to another depends on the current state the SQUID is in. However, the boundary between very weak and very strong IM generation region is determined by the critical rf flux envelope value for the lowest δ amplitude branch, labeled as ϕ_{lh1}. Once the peak value of the rf flux envelope function passes ϕ_{lh1}, the gauge-invariant phase δ would jump from the lowest amplitude branch to another high amplitude state.

An example of this state jump is shown in Fig. 6.12 (c) for the zero dc flux case where the envelope of δ as a function of the envelope of ϕ_{rf} is plotted in a much larger scale than Fig. 6.12 (b), so it reveals more states at higher amplitudes. The amplitude of the δ envelope changes from 0.25 to 13 during the abrupt state jump, giving rise to a much stronger IM products than the previously discussed IM products generated in the bi-stable regime. Thus the IM generation is always strongest around the geometrical resonant frequency at high tone powers.

From Fig. 6.12 (b) we can tell that the first critical rf flux envelope value ϕ_{lh1} is largest when $\phi_{dc}/2\pi$ is equal to 0 and 0.5, and is smallest near 0.3. This qualitatively explains the dc flux modulated boundary between weak and strong IM generation near the geometrical resonant frequency seen in Fig. 6.12 (a).

6.2.5 IM Hysteresis and Amplification in SQUID Metamaterial

We also notice that utilizing two equal-amplitude tone inputs always gives a zero node in the driving rf flux envelope, hence the IM products of the SQUID depend little on the system's history, even in the bistable regime. As long as the

rf flux envelope peak (determined by tone power) exceeds the transition point ϕ_{lh}, the SQUID will experience discontinuous jumps during a beat. However if the two tones have different amplitudes so that the minimum value of the envelope is higher than ϕ_{hl}, the amplitude of the δ envelope depends on the direction of tone power sweep. In an upward sweep δ modulates in the low-amplitude branch during the whole beat until the tone power increases to the point that the rf flux envelope peak exceeds ϕ_{lh}; δ will then keep oscillating in the high-amplitude branch during a beat. In a downward tone power scan though, δ would modulate with the beating rf flux in the high-amplitude branch until the peak drops below ϕ_{hl}.

The predicted hysteresis brought on by the difference between the two tone amplitudes is observed in experiment. For example, I plot the measured lower third IM power generated from an 11×11 rf-SQUID array metamaterial in Fig. 6.13 as a function of pump power (power of the lower tone frequency f_1) and the two-tone center frequency, under three different tone amplitude ratios. For equal tone amplitude, the upward power scan (Fig. 6.13 (a)) and the downward power scan (Fig. 6.13 (d)) result in similar onset power of IM generations at a fixed frequency. Keeping the power of the upper main tone f_2 20 dB less than the power of f_1 (Figs. 6.13 (c) and (f)), however, gives rise to an approximately 15 dBm difference in the onset power of strong IM generation at a tone center frequency of around 16 GHz, depending on the direction of the tone power scan. Figures 6.13 (b) and (e) display the results from upward and downward power scans when there is a 10 dB difference in two tones. The third IM power shows an intermediate level of hysteresis.

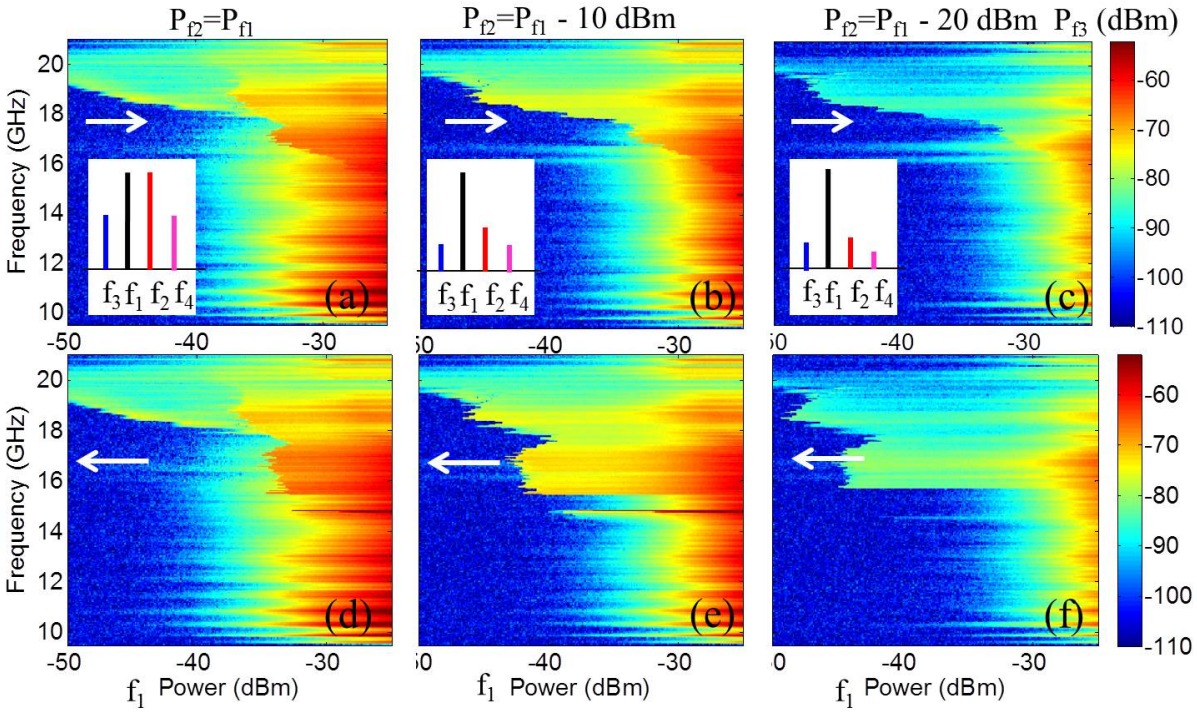

Figure 6.13: The measured lower 3^{rd} IM power generated from an 11×11 rf-SQUID array metamaterial as a function of pump power (power of the lower tone frequency f_1) and two-tone center frequency, at 0 dc flux. Tone power upward scan: (a) The two tones have the same power. (b) The power of f_2 (signal) is 10 dBm lower than the pump f_1. (c) The power of f_2 (signal) is 20 dBm lower than the pump f_1. (d) to (e) plot the same quantities for downward power scan. The spacing between the two tone inputs is 10 MHz. The temperature is 4.6 K.

Chapter 7: Conclusions and Future Work

Rf-SQUID metamaterials combine the advantages of superconducting electronics and nonlinear metamaterials. We have shown in previous sections that the rf-SQUID meta-atom and metamaterial are very nonlinear and tunable when responding to dc/rf magnetic field. The single-tone experiments and simulations show that the SQUID meta-atoms and metamaterials yield large tunability in resonant frequency at low rf flux amplitudes, enabling potential applications in fast tunable digital filters. The broadband and switchable transparency behavior in the rf-SQUID meta-atoms and metamaterials also holds promise for applications in power limiters, digital communication transmitters, gain modulated quantum antennas, and the novel concept of a metamaterial that automatically reduces its scattering cross section to near zero (auto-cloaking). The range, switchability and tunability of the transparency can be accurately evaluated by a Duffing oscillator approximation. Therefore we can design SQUID meta-atoms and metamaterials with controllable and predictable transparency bahavior.

We also studied the multi-tone response of SQUID meta-atoms and metamaterials via the intermodulation experiments. We find that under certain combinations of tone power and frequency, the SQUID shows a sudden onset of the 3^{rd} order IM

generation followed by a near-zero 3^{rd} order IM generation (gap). This phenomenon is a result of the bi-stable properties of rf-SQUIDs. This intrinsic suppression of IM generation may be useful as a mechanism for depressing signal mixing in communication applications. A detailed theoretical model is presented to explain this surprising gap feature in IM generation. The intensity of IM generation sensitively depends on the parameters of the rf-SQUIDs, and can be modulated by dc/rf magnetic field, and temperature, potentially allowing one to design and tune the IM generation to meet various requirements for applications.

These works bring novel physics into nonlinear metamaterial research, and serve to link the fields of quantitative nonlinear dynamics and macroscopic quantum effects to the metamaterials community. It also introduces revolutionary new applications of metamaterials.

In the subsequent parts in this chapter I will summarize the experimental, theoretical, and analytical results obtained in this thesis work, and propose some future works on the SQUID meta-atoms and metamaterials.

7.1 Tunable Transmission (Resonance) of rf-SQUID Meta-atoms and Metamaterials

The rf-SQUID meta-atoms and metamaterials have a resonant frequency tunability of up to 80THz/Gauss via dc flux when the driving rf flux amplitude is low. For intermediate rf flux amplitudes, the rf-SQUID meta-atoms and metamaterials are bistable. The bistability results in lower resonant frequency and a nearly full dis-

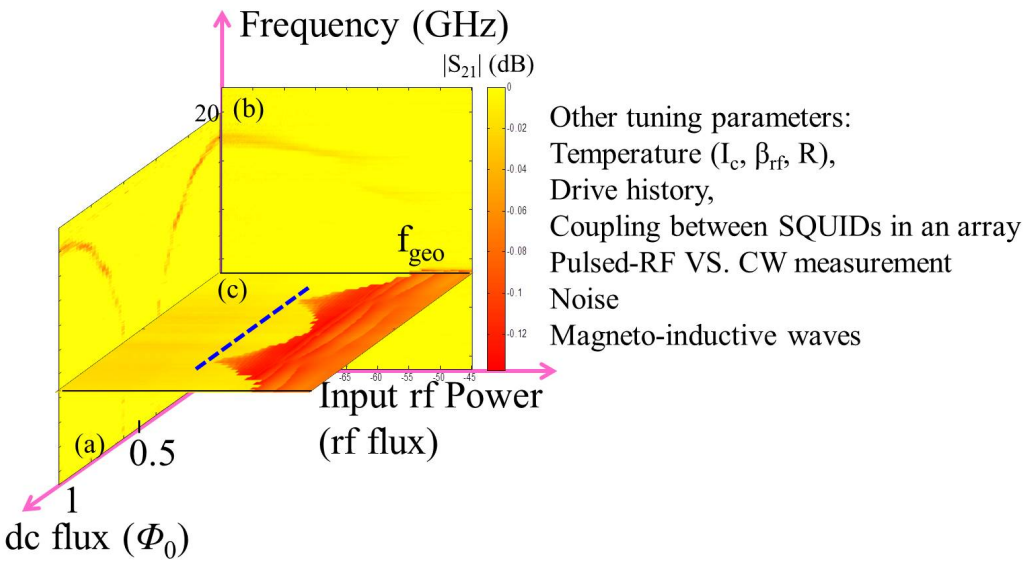

Figure 7.1: The tuning parameter space for SQUID meta-atoms and SQUID metamaterials. The transmission as a function of (a) dc flux and frequency, (b) input rf power and frequency, and (c) dc flux and input rf power.

appearance of resonance absorption (transparency). Such broadband transparency can be switched on and off via drive frequency or amplitude hysteresis, and dc flux. At higher rf amplitudes, the SQUIDs become multistable around the geometrical resonant frequency. The onset rf amplitude for entering the mulstability regime also tunes with dc flux.

There are many things one can use to tune the transmission properties of an rf-SQUID meta-atom or a metamaterial. To obtain a bigger picture based on those properties and link them together, I like to think of transmission being tuned inside a parameter space composed of a dc flux axis, an rf power (rf flux) axis, and a frequency axis, as plotted in Fig. 7.1. Inside the parameter space, every surface corresponds to a unique resonance behavior. I build the parameter space for the single rf-SQUID meta-atom, cut three surfaces, and plot the transmission in colors

for each of the surfaces in this tuning parameter space in Fig. 7.1. Red features denote the low transmission in a resonance.

The surface shown as Fig. 7.1 (a) displays the transmission as a function of dc flux and frequency when the value of input rf flux is extremely low. The resonant frequency in this case tunes smoothly by the dc flux all the way from 19 GHz to 2 GHz at a temperature of 4.6 K. This tunable resonant frequency can be predicted by a simple circuit model which treats the Josephson junction as an effective inductance.

Another cut at the zero dc flux (Fig. 7.1 (b)) shows the transmission in colors as a function of frequency and the input rf power, where the resonance gradually disappears in the intermediate power range, and reappears strongly at the geometrical resonant frequency f_{geo}. The disappearance of the resonance is a result of bistability of the SQUID, and can be analyzed in detail using the Duffing oscillator approximation. Inside the bistability regime, the SQUID can be transparent (weak resonance) or opaque (strong resonance) depending on the drive history.

Then we cut a surface perpendicular to the frequency axis at this geometrical resonant frequency f_{geo}, and observe the transmission as a function of the dc flux and the input rf power (Fig. 7.1 (c)), where the onset of this strong geometrical resonance modulates dramatically with dc flux. The SQUID enters the multistable regime above the critical power. In the multistable regime, the resonant frequency is fixed at the geometrical resonant frequency f_{geo}, but the strength of the resonance depends on the particular state the SQUID is in. Jumping between states generates stair-like transmission as a function of the rf power [59, 63].

We can move the surface (transmission as a function of dc flux and frequency) in Fig. 7.1 (a) along the rf power axis. The resonant frequency at zero dc flux will transit to lower frequencies at higher rf powers, and the strength of the resonance dip would decrease because the SQUID enters the low-amplitude state of the bistable regime. Moreover, as the surface in Fig. 7.1 (a) moves to a point where the rf power value is higher than the lowest critical rf power for the geometrical resonance (labeled by the dashed blue line in Fig. 7.1 (c)), the resonance will be very strong at the geometrical resonant frequency at the dc flux values for low onset rf powers, while staying weak at other dc flux values. An example is shown in Fig. 4.13 and discussed there. The transparency behavior can thus be tuned on and off by dc flux.

Similarly, moving the surface in Fig. 7.1 (b) along the dc flux axis, the transmission as a function of frequency and input rf power will change according to the trend in Fig. 7.1 (a) and Fig. 7.1 (c). For instance the resonant frequency at very low rf flux amplitudes consistently becomes lower as the dc flux changes from 0 to 0.5 Φ_0. At the same time, the onset rf power of the strong geometrical resonance modulates with the dc flux. As a result, the transparency rf power range where the resonance is weak and undetectable is the smallest when the SQUID is driven at 0.25 Φ_0. When the surface in Fig. 7.1 (b) is at a dc flux value near 0.5 Φ_0, the low-rf-flux resonant frequency is below the geometrical resonant frequency f_{geo}. A consequence is that the resonant frequency will increase as the rf flux amplitude increases.

One can also move surface Fig. 7.1 (c) along the frequency axis. This behavior has not been explored in my work yet, and may be interesting to look at in the

future. I can imagine that there will be an onset rf power and an offset rf power for the resonance at any fixed frequency inside the tunable frequency range. The two critical rf powers, and the strengths of the resonance at a fixed frequency can also modulate with dc flux.

The surfaces in the tuning parameter space basically covers all the transmission properties of an rf-SQUID meta-atom or a SQUID metamaterial. Other tuning parameters, such as temperatures, drive history, couplings between meta-atoms in an array, the measurement methods, additive noise and standing waves all modify transmission behaviors inside this space.

In the thesis, the temperature dependence has been discussed in detail, especially for the dc flux tunability of the resonant frequency at low rf powers. The temperature affects the critical current in the Josephson junction, and further the value of β_{rf}. A higher β_{rf} value results in larger resonant frequency tunability via the dc flux (Fig. 4.3), and broadens the rf power range where the SQUID is bistable and shows transparency behavior (Fig. 4.8). Higher temperature also breaks more Cooper-pairs into normal electrons, giving rise to a lower gap resistance in the junction and a lower quality factor of the SQUID.

7.2 Discussion of IM generation in SQUID Meta-atoms and Metamaterials

The rf-SQUID meta-atoms and metamaterials have rich intermodulation generation due to the nonlinearity of the Josephson junctions. Experiment, numerical

simulation, and analytical models all predict a sharp onset followed by a dip in the third order IM output as a function of the tone center frequency. The rf-SQUID array metamaterials show similar unique behaviors as the single rf-SQUID meta-atom. The sharp onset of IM generation comes from a series of asymmetric jumps between two stable states of the rf-SQUID as the drive amplitude modulates during a beat of the input signal. Each state jump creates a transient response appearing as ringing in the time domain. The dynamics can be explained by a dynamical model employing a Hamiltonian analysis with damping.

Three models for IM generation in rf-SQUIDs have been discussed. The solutions to the full numerical nonlinear model contain the most complete information for the response of rf-SQUIDs to two-tone excitation, yet gives little insight into the underlying physics. The steady-state analytical model greatly simplifies the 2^{nd} order nonlinear differential equation to three coupled algebraic equations, and sheds light on the origin of the unique IM features - the state jumps during a beat period cause an abrupt increase in IM products. While it predicts the same level of IM generation as calculated by numerical simulation (Fig. 6.3), the steady-state model lacks the dynamics accompanying each state jump, which can be understood using the nonlinear dynamical model. This model reduces the full nonlinear equation to a complex first order differential equation, and allows for construction of a Hamiltonian for the SQUID. The topology of the Hamiltonian surfaces evolves continuously as the envelope of the drive signal changes. The topology determines the form of the trajectories, $\hat{\delta}(t)$, to be spirals during transitions as the SQUID switches from one stable state to another, resulting in ringing features in $\delta(t)$.

According to these models, we can design SQUID metamaterials to generate either very high or very low IM products in response to multi-tone excitation. The analytical models can also be applied to design other nonlinear systems employing Josephson junctions, such as the Josephson parametric amplifier.

7.3 Future Work

The equations discussed in my thesis focus on the single Josephson junction system. These models can also predict the behaviors of the rf-SQUID array metamaterials assuming that the meta-atoms are identical, not coupled to each other, and subjected to uniform driving conditions (including dc and rf flux, temperature). For a coherent array metamaterial, the tunability of resonant frequency with dc flux, the hysteretic transparency behaviors, the rich IM generation and the gap feature in the IM products are similar to a single rf-SQUID. However, we also see that the arrays under nonuniform dc flux lose the collective tunable resonance (an example is shown in Fig. 4.5).

The effects of coupling and nonuniform dc flux in the SQUID metamaterial are intensively discussed in my colleague's work [68] which focuses on the transmission properties. Her work theoretically suggests that the coupling between SQUIDs would enhance the resonance strengths, increase the resonant frequency, and gives rise to magneto-inductive modes when the SQUID arrays experience non-uniform dc flux. The current experimental-setup only measures the collective response from the whole array, but lacks the local information on each SQUID. Thus the distribution

of amplitudes and phases of the SQUIDs in each magneto-inductive mode cannot be measured directly. A near-future experiment is to use a laser scanning microscope to scan the whole array and measure the microwave response (magnitude and phase) at the location of each SQUID [129].

It would be intriguing to build a metasurface using an array of SQUIDs. This requires a totally different experiment configuration. The incident wave propagates at an angle to the 2D SQUID array metamaterial plane, and we measure the propagation direction of the output electro-magnetic wave. The output propagation direction depends on the angle of the incident wave, and the properties of the metasurface [130]. If one can create a gradient of magnetic field across the 2D array metasurface, the SQUIDs interact with the incident wave differently, and might cause a steering of the original wave propagation. The gradient can be applied by a coil, or by designing on-chip wires around the SQUID meta-atoms so we can change the local magnetic fields by applying current into these wires. Another method is to use non-identical SQUID meta-atoms in an array to create the intrinsic gradual property variation across the whole metasurface. For this experiment, an angle-sensitive setup is needed so we can measure the angle of the output wave as we change the magnetic field gradient or the angle of the incident wave.

All of our SQUIDs are designed to have a less-than-unity β_{rf} to avoid complications brought by the chaotic behavior and the hysteretic dc flux behavior [112]. Now that we have studied in detail the dynamics of non-hysteretic rf-SQUID meta-atoms and metamaterials, it might be worth stepping further and looking at the SQUID design with higher β_{rf} values. I have designed a single rf-SQUID meta-

atom and a SQUID array metamaterial that have the same size, and geometrical resonant frequency as our currently measured single SQUID meta-atom. The only difference is that the areas of the junction is larger so the critical current is higher, resulting in a β_{rf} value of 2.7.

The calculated resonant frequency as a function of the dc flux is shown in Fig. 7.2 for a unity β_{rf} (blue curve) and a larger β_{rf} (red curve). Increasing the β_{rf} value greatly enhances the resonant frequency tunability with the dc flux, however, the sharp tuning resonance feature (nearly vertical as a function of dc flux) below the geometrical resonant frequency may be hard to follow in an experiment. The tuning also depends on the direction of the dc flux scanning. One thing good about the higher β_{rf} value in our experiment is that we can carefully control the temperature and explore the behaviors for β_{rf} values ranging from 0 - 2.7. Higher β_{rf} values also have the benefits of inducing Chimera states in an rf-SQUID array metamaterial [69]. We also plan to deliberately create Chimera states in the SQUID metamaterial and measure them using the laser scanning microscope in the future.

We have not investigated the effects of coupling and nonuniform dc flux on the IM generation in SQUID array metamaterials. In the experiment on an 11×11 array, even when the two input tones are equal in amplitude, there is a hysteretic onset tone power for the strong IM generation at a center tone frequency of around 16 GHz (see Fig. 6.13 (a) and (d)). The upward tone power scan gives a higher onset power for the abrupt increase in IM products as a function of the tone power. The single SQUID meta-atom, however, never shows a measurable hysteretic IM generation. The single junction Eq. 6.2 predicts that the hysteresis is small for

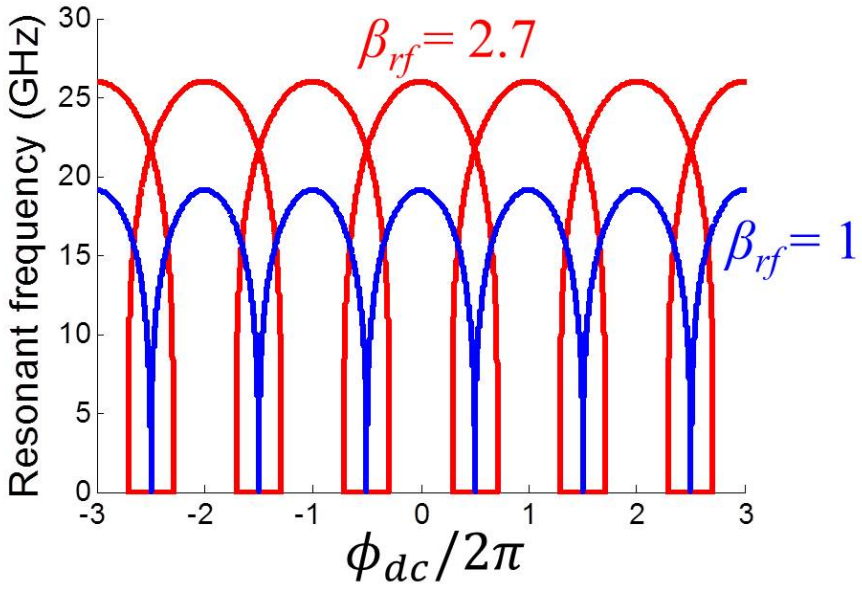

Figure 7.2: The resonant frequency as a function the applied dc flux at very low rf flux amplitude for the single rf-SQUID meta-atom, for $\beta_{rf} = 1$ (blue) and $\beta_{rf} = 2.7$ (red).

the equal tone case due to the zero amplitude of the rf flux drive during every beat period. Apparently the array shows some two-tone response that cannot be explained by the single Josephson junction model. The theoretical model for the IM generation in the future should include the coupling and the non-uniform drive in the SQUID metamaterials.

One interesting topic is whether the sudden onset and the gap feature in the IM generation are affected by putting the SQUIDs in an array, especially when they couple strongly and form magneto-inductive modes where the SQUIDs oscillate at different amplitudes and phases under non-uniform magnetic fields. I think the onset would be less sharp, and the gap would be shallower for the SQUID array because each SQUID has an onset and a gap at a slightly different tone center frequency. However since the cause of the sudden onset and the gap feature is

the intrinsic bistability of the rf-SQUIDs, and this is not altered for SQUIDs in an array. Therefor these phenomena observed should be robust against noise and non-uniformity, consistent with our experimental observation for the SQUID array metamaterials.

The discussed theoretical results for the IM generation in my thesis mainly focus on the bistable regime of the SQUIDs, where the intrinsically suppressed IM generation happens. The multi-stable states results in complex and interesting stair-like features when the two tones center near the geometrical resonant frequency (see Fig. 6.12). I hope to understand these features using the tools of nonlinear dynamics in the multistability regime.

Finally, our current experimental setup has a base temperature of 4.6 K, so the SQUIDs behave classically. Now our lab has the capability for measurements in the mK temperature range. The extreme low temperatures allows one to address discrete quantum energy levels in the SQUID metamaterials, and introduces intriguing quantum phenomena. We are now designing a quantum Josephson junction metamaterial that can be explored utilizing the methods and theories discussed in this thesis.

Appendix A: Pulsed RF Measurement of SQUID Meta-atoms

In the main thesis parts, only the continuous wave (CW) measurement results are considered, where the rf wave is turned on all the time and has the same amplitude over the whole measurement time span. However we have found some cases of discrepancy between the experiment and the simulation. For example, the critical rf power where the single SQUID meta-atom shows strong resonance absorption at the geometrical resonant frequency, or the critical power where the SQUID meta-atom enters the multistability regime, differs by approximately 10 dBm between data and simulation. One hypothesis is that the energy at high powers absorbed by the SQUID is largely confined in the chip due to poor heat transfer between the chip and the foam inside the rectangular waveguide, thus contributing to a local temperature increase in the experiment. According to the discussions in Chap. 2, increasing the temperature gives rise to a lower upper critical rf power.

In a pulsed-rf measurement, the rf wave is turned on for a certain time span t_w, and then turned off for some time, in a periodic manner with a periodicity of t_p. The S-parameters are measured when the pulse is on. The scheme is shown in Fig. A.1. The pulse width is much longer than the fast oscillating rf wave period so that we are sure the SQUIDs are in their steady state response in the pulse. The shortest

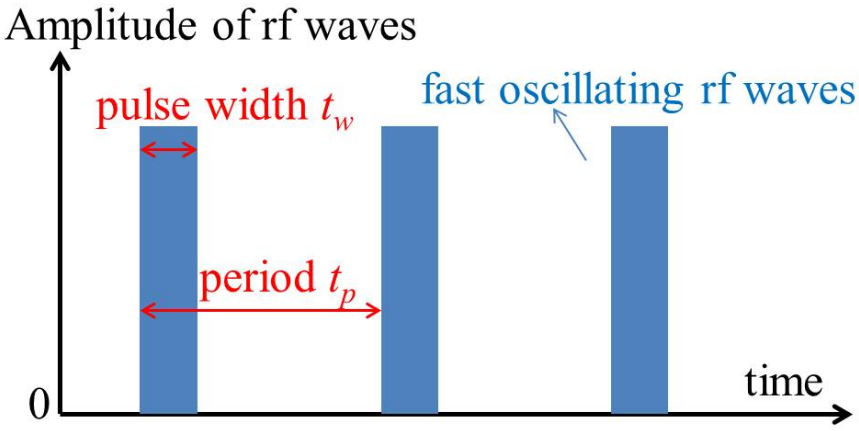

Figure A.1: The scheme of a pulsed-rf measurement.

pulse width in experiment, 2 μs, contains at least 20,000 fast rf oscillation periods. The Duty cycle value is defined here as t_w/t_p, *i.e.* the percentage of a pulse being on in a cycle. In the following discussion I will show how pulsed-rf measurement changes the nonlinear behaviors of the single SQUID meta-atom.

The transmission as a function of driving frequency and rf power for the single rf-SQUID meta-atom at a temperature of 4.6 K and zero dc flux is plotted in Figs. A.2 (a) - (e) for the pulsed rf measurement (pulse width 200 μs and pulse periodicity 1 ms), CW measurement, and numerical simulation, when rf power is scanned from low values to high values as the frequency is fixed. Reducing the duty cycle from 100% to 20% increases the upper critical rf power by 5 dBm, closer to the result in simulation.

The Transparency values (defined in Chapter 4) of the pulsed-rf measurement, the CW measurement, and the simulation are plotted in Fig. A.2 (f) as blue , red, and black curves, respectively. The CW transparency curve shows a slightly higher onset power and a 5 dBm lower upper critical power in the transparency range - the

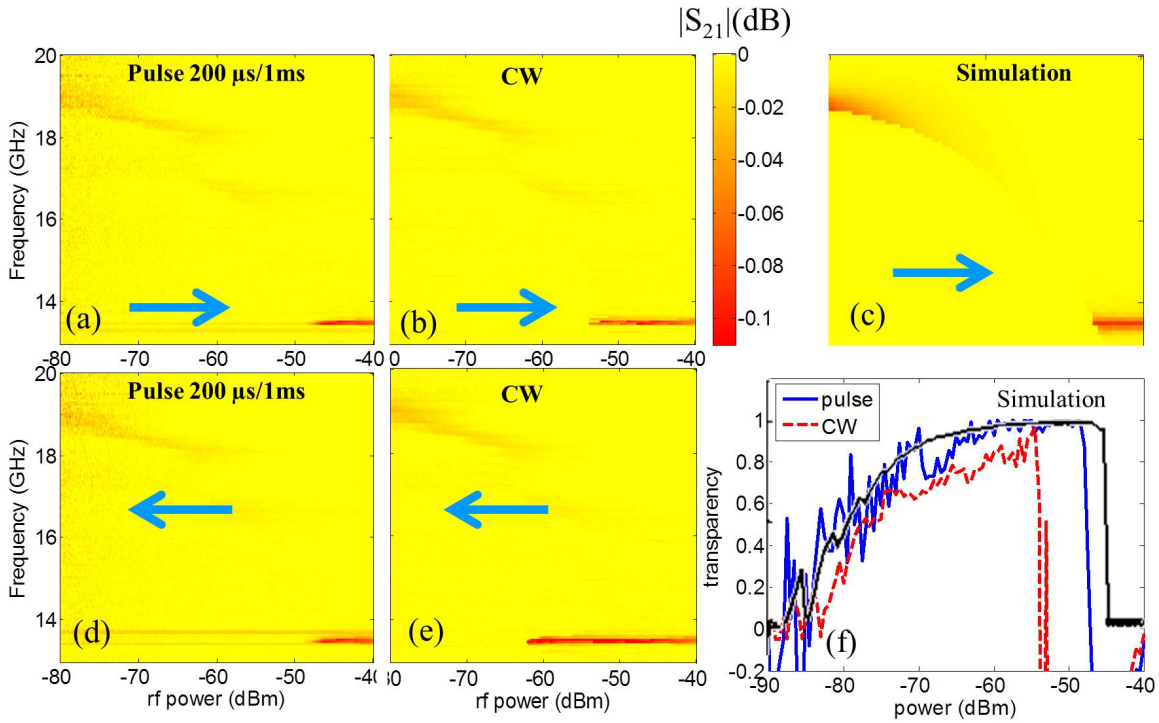

Figure A.2: The transmission of the single rf-SQUID meta-atom as a function of frequency and rf power under zero dc flux of (a) pulsed-rf measurement and (b) CW measurement, and (c) simulation, at a temperature of 4.6 K. (a) - (c) are results of an upward rf power scan. Downward rf power scan results are shown in (d) pulsed-rf measurement and (e) CW measurement. The extracted transparency as a function of rf power from (a) - (c). The pulse has a width of 200 μs and a periodicity of 1 ms (20% duty cycle).

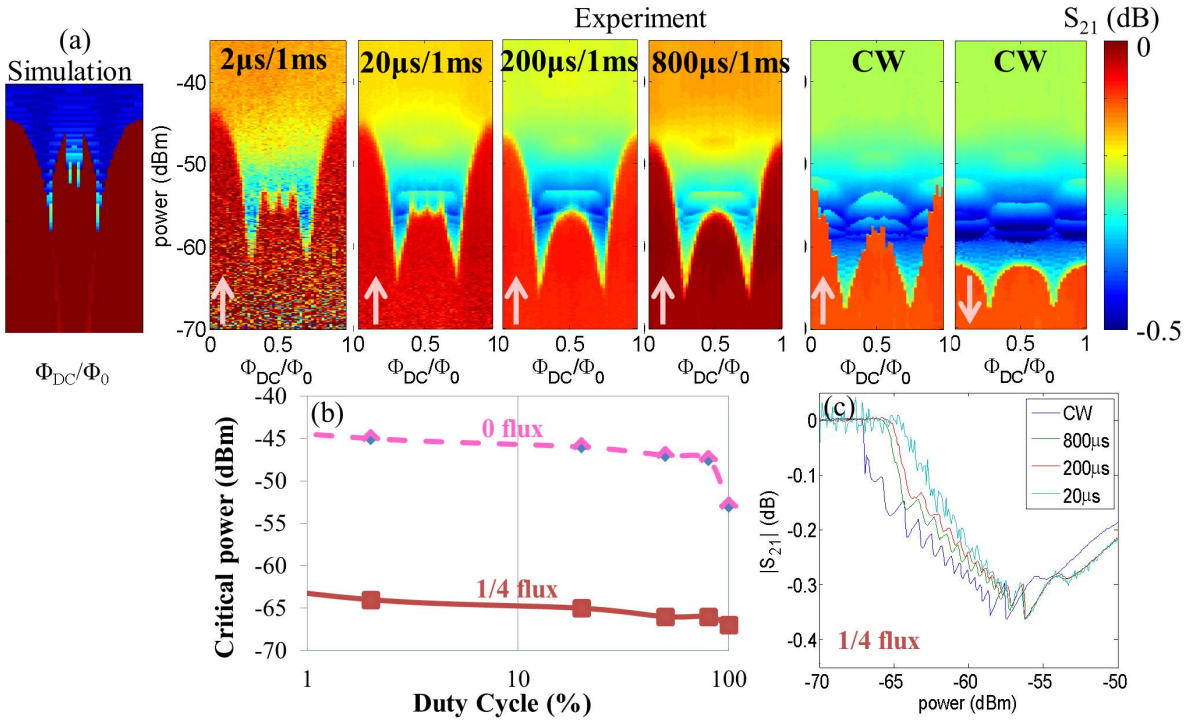

Figure A.3: (a) The transmission as a function of rf flux and dc flux at the geometrical frequency $\omega_{geo}/2\pi$ of simulation, pulsed-rf experiment, and CW experiment for a single rf-SQUID at 4.6 K. (b) The critical power as a function of duty cycle. (c) The power cut at a dc flux value of $0.25\Phi_0$.

same effect brought by increasing temperature. The transparency extracted from the pulsed-rf measurement resembles more of the simulation.

A reversed rf power scan does not change the transmission in the pulsed-rf measurement. However in the CW measurement and simulation, a reversed rf power scan causes a 10 dBm decrease in the upper critical power for the strong resonance at the geometrical resonant frequency 13.52 GHz. This is because during the pulsed-rf measurement all the history in the SQUID meta-atom vanishes inside the time period when the pulse is off.

Since the main difference between the pulsed-rf and CW measurement lies in the onset for the strong resonance at the geometrical resonant frequency, I measure

the transmission as a function of rf power at this frequency, 13.52 GHz, with different pulse widths, and check how the dc flux dependence of this critical power is modified. The results are displayed in Fig. A.3 (a) and compared with the simulated transmission. The strong resonance absorption (blue region) at the geometrical frequency determines the upper critical rf power. The edge between the blue region and the red region denotes the tuning of upper critical rf power by applied dc flux. I extract and plot the critical power as a function of duty cycle in Fig. A.3 (b) for two dc flux values. As the pulse width becomes larger, the critical power gets lower for all dc flux values.

Also, around 0.5 Φ_0 dc flux, there is a "w"-shape feature at the boundary in the simulation, as well as in the pulsed-rf experiment where the pulse width is 2 μs in a periodicity of 1 ms. This feature gradually disappears at higher duty cycles.

The pulsed-rf and CW measurements both have a lowest critical power at around 0.25 Φ_0 dc flux, and highest critical power at 0 dc flux. Above the critical power the SQUID meta-atom enters the multistability regime. Each state has a different amplitude thus presents a different transmission value. As the SQUID meta-atom jumps from one state to another, the transmission shows a step feature. A frequency cut at the 0.25 Φ_0 dc flux value is plotted in Fig. A.3 (c) that clearly reveals these state jumps. This plot demonstrates that the pulse widths also affects the state jumps. References [63] and [59] investigated these state-changes in rf-SQUID meta-atoms and metamaterials induced using very short pulses (ns) near the geometrical resonance frequency at zero dc flux.

Appendix B: The Effect of Noise on Simulations of SQUID Meta-atoms and Metamaterials

Up to this point all simulations ignore the effect of noise, but in actual experiment noise is unavoidable. The noise-free simulations may miss important behaviors that are seen in experiments. Adding noise to the simulation allows one to explore other solutions that are not otherwise accessible. Here I will show some preliminary results of adding noise in the numerical simulation, and see how the noise can affect the transmission of a SQUID meta-atoms.

Noise is simulated as a magnetic flux $f_n(t) = \phi_n(t)/2\pi$ that changes with time. Assuming it is white noise, at each time point a random value within a certain range is assigned to the noise flux by the Python code I wrote. The equation of a SQUID meta-atom with noise becomes:

$$\frac{d^2\delta}{d\tau^2} + \frac{1}{Q}\frac{d\delta}{d\tau} + \delta + \beta_{rf}\sin\delta = (\phi_{dc} + \phi_{rf}\sin\Omega\tau + \phi_n(\tau)) \tag{B.1}$$

Again, $\phi_{dc} = 2\pi\Phi_{dc}/\Phi_0$ and $\phi_{rf} = 2\pi\Phi_{rf}/\Phi_0$ are the applied dimensionless dc flux and rf flux, $\omega_{geo} = 2\pi f_{geo} = 1/\sqrt{LC}$ is the geometrical frequency, $\Omega = \omega/\omega_{geo}$, $\tau = \omega_{geo}t$, $Q = R\sqrt{C/L}$ is the quality factor of the SQUID that reflects the dissipation,

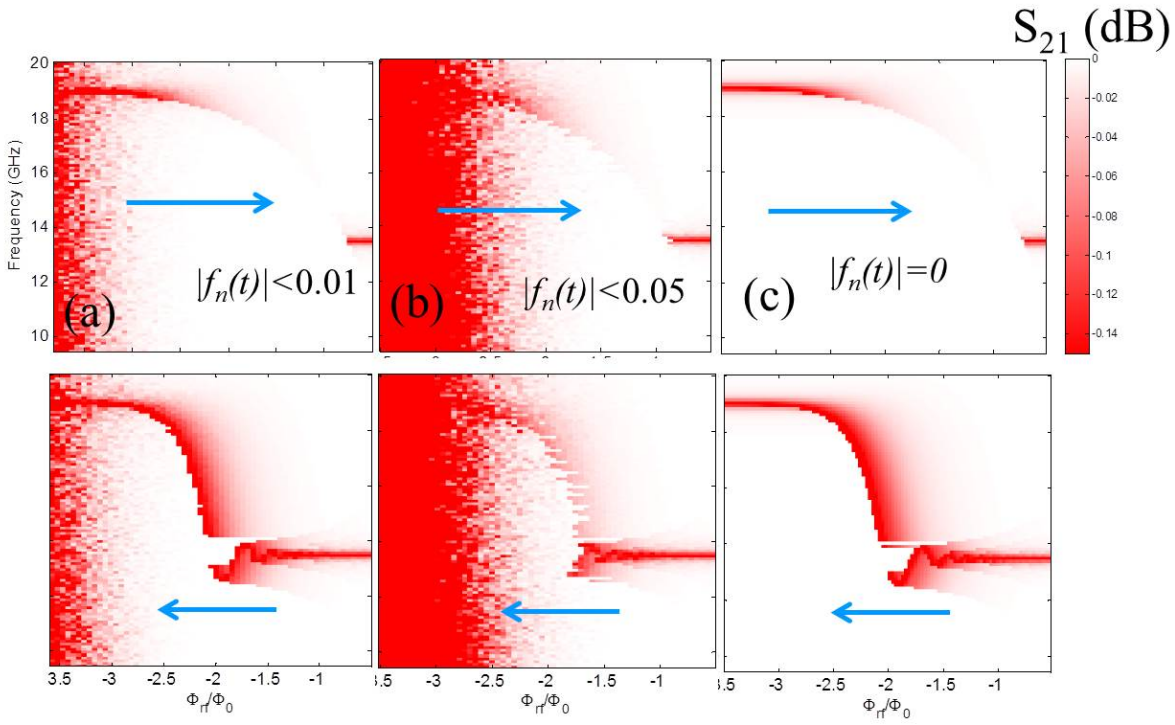

Figure B.1: The transmission of the single rf-SQUID meta-atom as a function of frequency and rf flux under zero dc flux, at noise flux levels of (a) $|f_n(t)|< 0.01$, (b) $|f_n(t)|< 0.01$ and (c) no noise, at a temperature of 4.6 K. The three upper (lower) plots are results of an upward (downward) rf power scan.

and $\beta_{rf} = 2\pi LI_c/\Phi_0$ is the coefficient determining the degree of nonlinearity and tunability in an rf-SQUID. I solve this equation numerically with the same parameter set used for the single rf-SQUID meta-atom to get the gauge-invariant phase $\delta(\tau)$, and further calculate the transmission S_{21} (see Chap. 2 for details).

The simulated transmission as a function of frequency and rf flux under two noise levels is shown in Figs. B.1 (a) and (b). They are compared with results from simulation free of noise Figs. B.1 (c) . The red feature denotes the resonance. At low rf flux amplitude values, the resonance strength is smaller than the noise and thus is lost in the vertical red noise bands at small Φ_{rf}. For a smaller noise level ($|f_n(t)|< 0.01$), the disappearance of resonance in the intermediate rf flux range is

more clear, and the hysteresis in the rf flux scan is larger than the higher noise level case. Also, adding noise reduces the upper critical power for the strong resonance at the geometrical resonant frequency 13.52 GHz. This might explain why the critical power is lower in experiment than in simulations which ignores noise (see Fig. 4.8 (a)).

In conclusion, the reduced range and degree of the broadband transparency seen in the SQUID meta-atoms and metamaterials in experiment can be realized by adding noise in the simulation. The noise also depresses the hysteresis in the bistable regime. However adding noise does not destroy the transparency behavior. It is important to lower the noise level in the experiment for a more robust and larger range broadband transparency.

Appendix C: Detailed Understanding the Gap Feature in IM generation of SQUID Meta-atoms and Metamaterials

In Chap. 6, I discussed the IM generation in SQUID meta-atoms and metamaterials. A prominent IM gap feature is observed both in experiment and in simulations. The extracted amplitudes of the gauge-invariant phase for the two main tones and two third order IM tones are plotted as a function of center frequency in Fig. C.1 (a). The near-zero amplitude of upper third order IM (δ_4) at a tone center frequency of around 17.75 GHz suggests both the real part and the imaginary part of this tone are equal to zero. Chapter 6 mainly shows the result of the amplitude information. In fact, the phase plays an important part in the zero-amplitude IM tone generation.

Figure C.1 (b) - (f) display the extracted δ_1 to δ_4 from $\delta(t)$ calculated by the steady-state model (Eqs. (6.5)-(6.7)) in the complex δ-plane, where the distance to the origin denotes the amplitude, and the angle relative to the positive x-axis ($Re[\delta]$) denotes the phase of each tone δ_i where $i = 1, 2, 3, 4$. As the tone center frequencies changes from 16 to 18.9 GHz (around the gap feature), the amplitudes and phases of the two main tones and the two third order IM tones also vary. Results shown in Fig. C.1 (b) are calculated using the same parameter set as of Fig. C.1 (a), *i.e.*,

the rf power is -65 dBm, the resistance is $R = 1780\Omega$, and the nonlinear quantity β_{rf} is 0.98. The arrows denote the change as the center frequency increases. The two main tones and the two third IM tones are not symmetric about the x-axis.

The effects of various parameter values to the zero-crossing and the asymmetry are explored through analyzing Figs. C.1 (c)-(e) that display the amplitudes and phases of extracted δ_1 to δ_4 under several parameter sets. Increasing the resistance from R to $5R$ (Fig. C.1 (c)) eliminates the asymmetry as well as the zero amplitude point of δ_4. Changing the rf power (Fig. C.1 (d)) and the value of β_{rf} (Fig. C.1 (e)) does not affect the zero-crossing. Comparing Fig. C.1 (b) and (c) one sees that reducing the resistance from $5R$ to R results in asymmetric distortions which causes a counter-clockwise rotation for the two main tone curves, and a clockwise rotation for the two IM tones, in the complex δ-plane. This distortion causes the upper third order IM tone δ_4 to cross the origin (zero-crossing), while δ_3 stays away from the origin.

The resistance value affects the quality factor Q of an rf-SQUID. According to Eq. (6.6) the phase of $\delta(t)$ approaches zero when the resistance (or Q) is very high. This suggests that the existence of the imaginary part of $\delta(t)$ causes the asymmetry between upper and lower main tones and IM tones. To verify this, I plot δ_1 to δ_4 extracted from the real part of $\delta(t)$ only in Fig. C.1 (f). The full $\delta(t)$ and the real part of $\delta(t)$ as a function of time in a beat period are displayed as insets of Figs. C.1 (b) and (f), respectively. All other parameters are the same. The lack of imaginary parts give rise to disappearance of the asymmetry and the zero-crossing, as expected.

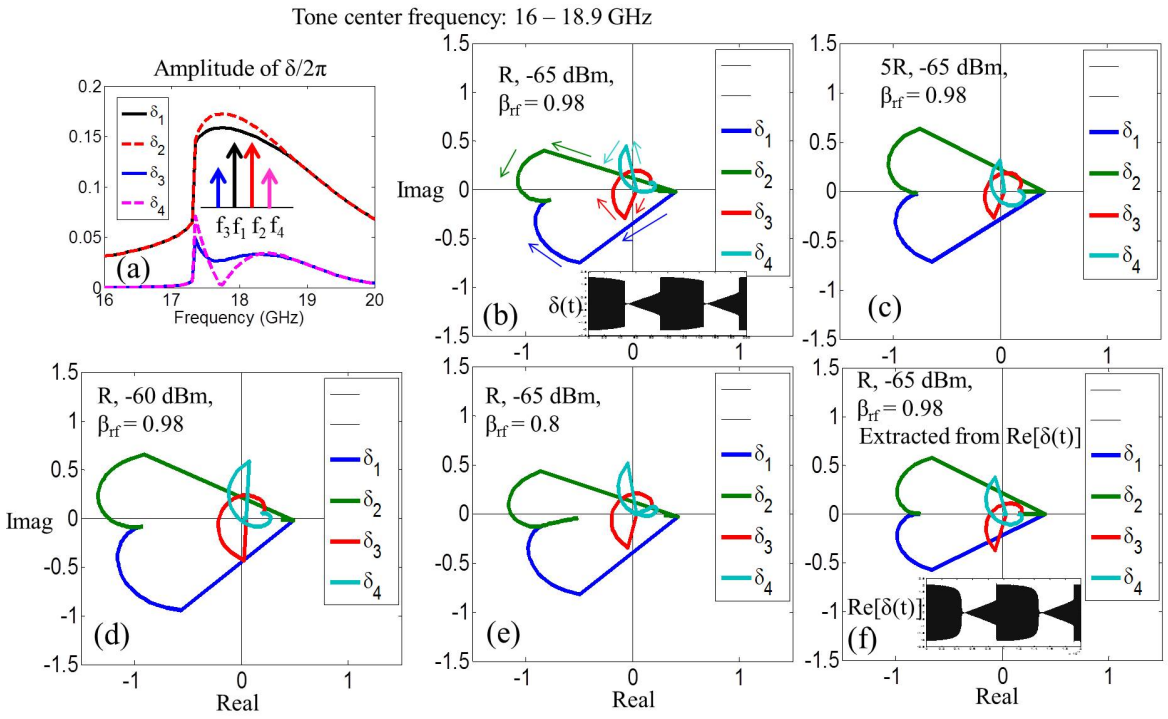

Figure C.1: The lower and upper main tone output δ_1 and δ_2, and third order tones δ_3 and δ_4 for a single rf-SQUID meta-atom calculated with steady-state analytical model. (a) The amplitudes of those four tones at an rf power of -65 dBm, resistance of $R = 1780\Omega$, and the nonlinear quantity β_{rf} of 0.98. (b) to (f) The amplitudes and phase of the four tones plotted in the complex $\delta-$plane under different conditions. The arrows denote the change as the center frequency increases. Insets of (b) and (f) shows the time dependence of full $\delta(t)$ and real part of $\delta(t)$ at the onset tone center frequency 17.35 GHz, respectively. All assume $\phi_{dc} = 0$.

From these analytical results we can predict that the asymmetry in the upper and lower IM tones is related to the loss in the SQUID. Tuning Q with temperature can make one of the IM tones have a "zero-crossing" as a function of the tone center frequency.

Appendix D: Detailed Information on How to Conduct the Experiment

The descriptions on the experimental setup for single-tone and two-tone measurements are summarized in Section 3.2 and Section 6.1, respectively. In this Appendix I would talk about the detailed procedures for a successful measurement.

D.1 Preparation of the Samples

The chips from Hypres Inc. are 5 mm $\times$ 5 mm in size. Each chip has several designs (Fig. 3.2) and we need to dice the chip in order to measure the designs separately. I used one of the dicing saws in the Maryland NanoCenter Fablab with the help of a technician [131]. Note that before the dicing process the chip has to be stabilized on a silicon wafer by wax. The wafer is 3-inch in diameter, or determined by the technician.

D.2 Put Sample in the waveguide

After the sample is diced and cleaned we can put it inside the rectangular waveguide. First of all, the rohacell is cut manually to fit the size of the waveguide

so it can be inserted into the waveguide without moving around. It is better to also cut the rohacell with a length that equals the length of the waveguide plus the distances of the antennas in the waveguide adapters to the ends of the waveguide. In this way, even when the waveguide is positioned vertically the rohacell can still be stabilized. This is extremely important for a uniform and stable dc magnetic field because the position of the solenoid is fixed outside the waveguide (Fig. 3.5). A slit is cut in the middle of the rohacell for the samples to sit in.

D.3 Assembly of Waveguide Holder and Other Components

The waveguide with samples can then be clamped in the E-shape waveguide holder as shown in Fig. 3.5. Two copper bars with screw holes are used to press and stabilize the waveguide in the holder. The coils and the heater are also clamped onto the waveguide holder using two customized copper holders (Fig. 3.5). One end of the thermal straps can be attached to the waveguide holder, or one corner of the bottom waveguide adapter. The other end of the thermal straps is usually screwed tightly onto one of the feedthroughs on the 4K plate.

D.4 Attach to the 4K plate

After all the components are held together, one can feed the top of the waveguide holder through the slit on the top lid of the mu-metal magnetic shielding (Fig. 3.6). Lead one of the coaxial cables and one thermometer into the round-shape opening in the magnetic shielding top lid, before screwing the lid and the waveguide

holder to the 4K plate. Then the thermometer should be attached to the bottom corner of the waveguide as shown in Fig. 3.5. The coaxial cable is connected to the top waveguide adapter. Make sure to adjust the waveguide holder's relative position to the magnetic shielding such that the whole setup stays within the shielding.

Next put the cylindrical mu-metal shielding around the assembled setup, and screw it to the top lid. All the dc wires, thermal straps should go out from the opening of the bottom lid of the magnetic shielding. Make sure that the other coaxial cable goes into the opening of the bottom lid and connect to the bottom waveguide adapter before one closes the bottom lid.

Then, the other ends of the thermal straps are screwed tightly onto one of the feedthroughs on the 4K plate. The dc wires for the heater and the coils are connected to the pins at the ends of the dc wires in the cryostat.

D.5 Microwave Measurement

The transmission and reflection of the rf-SQUID meta-atoms and metamaterials in a rectangular waveguide are measured by the Agilent PNA-X N5242A network analyzer. A source power calibration can be done for an accurate input rf power at one end of the waveguide [132]. The rf-SQUIDs work in low powers so one or two 20 dB attenuators are added at the input. A cryogenic low-noise amplifier and a room-temperature amplifier at the output ensures a detectable signal. The common TRL calibration and the *in situ* broadband cryogenic calibration method developed by my colleague [133] do not apply here due to the amplifiers in the route. In my

experiment, the calibration is usually done by subtracting the data measured above the critical temperature (often at 15 K) from the data collected below the critical temperature of the superconductor niobium (9.2 K).

I usually use the following parameters when setting up the measurement on the network analyzer [132]. Average (point mode) number is 3, the IF bandwidth is 50 Hz, the sweeping points number is around 1001. This combination gives low enough noise while keeps the measurement time not too long. The time for a single sweep is around 50 seconds. If you change the setting parameters and the sweep time varies, make sure to also change the wait time in the Matlab code to be around 3 seconds longer than the sweep time to ensure a complete measurement.

The network analyzer can also measure the intermodulation. Simply change the measurement class to IM sweep [132]. Other parameters are similar to the single-tone experiment.

The Matlab codes for running these experiments can be found in the group backup space under the folder named Daimeng.

D.6 Other Concerns

The typical pump down time for the cryostat is around 10 hours. If the pressure is still high after 10 hours, there is probably a leakage. Common leaks come from the O-ring of the 300 K can. To fix it, clean the O-ring and put the 300 K can back onto the cryostat. If this does not solve the issue, a careful leakage check is needed.

Typical cool down time is 36 hours. I usually wait for 2 days after starting

the compressor before taking the date. For temperature dependent experiment, I wait for an hour after the temperature of the waveguide (where the thermometer locates) reaches the setting value to make sure that the sample reaches the same temperature concerning the thermalization time of the sample. Also note that the temperature increases when using high magnet currents. A better heat sink method should be developed to solve this problem. After the low-temperature experiment, the warm-up process takes more than 2 days after the compressor is turned off. Wait until the temperature is at the room-temperature before one turns off the pump.

More tricks on the experiment of rf-SQUID meta-atoms and metamaterials can be found in Anlage group wiki page.

Bibliography

[1] V. G. Veselago. The electrodynamics of substances with simultaneously negative values of epsilon and mu. *Sov. Phys. Usp.*, 10(4):509–514, 1968.

[2] D. R. Smith, W. J. Padilla, D. C. Vier, S. C. Nemat-Nasser, and S. Schultz. Composite medium with simultaneously negative permeability and permittivity. *Phys. Rev. Lett.*, 84(18):4184–4187, 2000.

[3] R. A. Shelby, D. R. Smith, and S. Schultz. Experimental verification of a negative index of refraction. *Science*, 292(5514):77–79, 2001.

[4] J. B. Pendry, A. J. Holden, W. J. Stewart, and I. Youngs. Extremely low frequency plasmons in metallic mesostructures. *Phys. Rev. Lett.*, 76:4773–4776, Jun 1996.

[5] J. B. Pendry. Negative refraction makes a perfect lens. *Phys. Rev. Lett.*, 85(18):3966–3969, 2000.

[6] Z. Jacob, L. V. Alekseyev, and E. Narimanov. Optical hyperlens: Far-field imaging beyond the diffraction limit. *Opt. Express*, 14(18):8247–8256, 2006.

[7] A. Alu and N. Engheta. Pairing an epsilon-negative slab with a mu-negative slab: Resonance, tunneling and transparency. *IEEE Trans. Antennas Propag.*, 51(10):2558–2571, 2003.

[8] D. Schurig, J. J. Mock, B. J. Justice, S. A. Cummer, J. B. Pendry, A. F. Starr, and D. R. Smith. Metamaterial electromagnetic cloak at microwave frequencies. *Science*, 314(5801):977–980, 2006.

[9] U. Leonhardt. Optical conformal mapping. *Science*, 312(5781):1777–1780, 2006.

[10] J. B. Pendry, D. Schurig, and D. R. Smith. Controlling electromagnetic fields. *Science*, 312(5781):1780–1782, 2006.

[11] N. I. Landy, S. Sajuyigbe, J. J. Mock, D. R. Smith, and W. J. Padilla. Perfect metamaterial absorber. *Phys. Rev. Lett.*, 100(20):7402, 2008.

[12] A. A. Zharov, I. V. Shadrivov, and Y. S. Kivshar. Nonlinear properties of left-handed metamaterials. *Phys. Rev. Lett.*, 91(3):037401, 2003.

[13] E. B. Wikborg, V. K. Semenov, and K. K. Likharev. RSFQ front-end for a software radio receiver. *IEEE Trans. Appl. Supercond.*, 9(2):3615–3618, 1999.

[14] Mikhail Lapine, Ilya V. Shadrivov, and Yuri S. Kivshar. *Colloquium* : Nonlinear metamaterials. *Rev. Mod. Phys.*, 86:1093–1123, Sep 2014.

[15] D. K. Brock, O. A. Mukhanov, and J. Rosa. Superconductor digital RF development for software radio. *IEEE Communications Mag.*, 39(2):174–179, 2001.

[16] Ekaterina Poutrina, Da Huang, and David R Smith. Analysis of nonlinear electromagnetic metamaterials. *New Journal of Physics*, 12(9):093010, 2010.

[17] Ilya V. Shadrivov, Alexander B. Kozyrev, Daniel W. van der Weide, and Yuri S. Kivshar. Tunable transmission and harmonic generation in nonlinear metamaterials. *Applied Physics Letters*, 93(16), 2008.

[18] K. D. Irwin, G. C. Hilton, L. R. Vale, and K. W. Lehnert. Amplification and squeezing of quantum noise with a tunable Josephson metamaterial. *Nat. Phys.*, 4:929 – 931, 12 2008.

[19] Chongmin Lee and Chulhun Seo. Control scheme of harmonics and third-order intermodulation distortion with composite right/left-handed structure for linearity enhancement of power amplifier module. *Microwave and Optical Technology Letters*, 55(7):1497–1500, 2013.

[20] I. Gil, J. Bonache, J. Garcia-Garcia, F. Falcone, and F. Martin. Metamaterials in microstrip technology for filter applications. 1A:668–671, July 2005.

[21] M. Gil, J. Bonache, and F. Martín. Metamaterial filters: A review. *Metamaterials*, 2(4):186 – 197, 2008.

[22] Claire M. Watts, Christian C. Nadell, John Montoya, Sanjay Krishna, and Willie J. Padilla. Frequency-division-multiplexed single-pixel imaging with metamaterials. *Optica*, 3(2):133–138, Feb 2016.

[23] Sungjoon Lim, C. Caloz, and T. Itoh. Metamaterial-based electronically controlled transmission-line structure as a novel leaky-wave antenna with tunable radiation angle and beamwidth. *IEEE Transactions on Microwave Theory and Techniques*, 53(1):161–173, Jan 2005.

[24] R. W. Ziolkowski and A. Erentok. Metamaterial-based efficient electrically small antennas. *IEEE Trans. Antennas Propag.*, 54(7):2113–2130, 2006.

[25] Y. Dong, H. Toyao, and T. Itoh. Design and characterization of miniaturized patch antennas loaded with complementary split-ring resonators. *IEEE Transactions on Antennas and Propagation*, 60(2):772–785, Feb 2012.

[26] Z. Liu, N. Fang, T. Yen, and X. Zhang. Rapid growth of evanescent wave by a silver superlens. *Appl. Phys. Lett.*, 83(25):5184–5186, 2003.

[27] R. Ruppin. Surface polaritons of a left-handed medium. *Phys. Lett. A*, 277:61–64, 2000.

[28] R. Ruppin. Surface polaritons of a left-handed material slab. *J. Phys.: Condens. Matter*, 13:1811–1819, 2001.

[29] F. D. M. Haldane. Electromagnetic surface modes at interfaces with negative refractive index make a 'not-quite-perfect' lens. http://arxiv.org/abs/0206420, 2002.

[30] D. R. Smith, D. Schurig, M. Rosenbluth, S. Schultz, S. A. Ramakrishna, and J. B. Pendry. Limitations on subdiffraction imaging with a negative refractive index slab. *Appl. Phys. Lett.*, 82(10):1506–1508, 2003.

[31] T. Koschny, R. Moussa, and C. M. Soukoulis. Limits on the amplification of evanescent waves of left-handed materials. *J. Opt. Soc. Am. B*, 23(3):485–489, 2006.

[32] J. Dimmock. Losses in left-handed materials. *Opt. Express*, 11(19):2397–2402, 2003.

[33] J. Zhou, T. Koschny, M. Kafesaki, E. N. Economou, J. B. Pendry, and C. M. Soukoulis. Saturation of the magnetic response of split-ring resonators at optical frequencies. *Phys. Rev. Lett.*, 95(22):223902, 2005.

[34] A. Ishikawa, T. Tanaka, and S. Kawata. Negative magnetic permeability in the visible light region. *Phys. Rev. Lett.*, 95(23):237401, 2005.

[35] Y. A. Urzhumov and G. Shvets. Optical magnetism and negative refraction in plasmonic metamaterials. *Solid State Commun.*, 146(5/6):208–220, 2008.

[36] R. W. Ziolkowski and A. D. Kipple. Application of double negative materials to increase the power radiated by electrically small antennas. *IEEE Trans. Antennas Propag.*, 51(10):2626–2640, 2003.

[37] S. M. Anlage. The physics and applications of superconducting metamaterials. *J. Opt.*, 13(2):024001, 2011.

[38] Philipp Jung, Alexey V Ustinov, and Steven M Anlage. Progress in superconducting metamaterials. *Superconductor Science and Technology*, 27(7):073001, 2014.

[39] M. Ricci, N. Orloff, and S. M. Anlage. Superconducting metamaterials. *Appl. Phys. Lett.*, 87(3):034102, 2005.

[40] M. C. Ricci and S. M. Anlage. Single superconducting split-ring resonator electrodynamics. *Appl. Phys. Lett.*, 88(26):264102, 2006.

[41] J. Q. Gu, R. Singh, Z. Tian, W. Cao, Q. R. Xing, M. X. He, J. W. Zhang, J. G. Han, H. T. Chen, and W. L. Zhang. Terahertz superconductor metamaterial. *Appl. Phys. Lett.*, 97(7):071102, 2010.

[42] V. A. Fedotov, A. Tsiatmas, J. H. Shi, R. Buckingham, P. de Groot, Y. Chen, S. Wang, and N. I. Zheludev. Temperature control of Fano resonances and transmission in superconducting metamaterials. *Opt. Express*, 18(9):9015–9019, 2010.

[43] H. Chen, H. Yang, R. Singh, J. F. O'Hara, A. K. Azad, S. A. Trugman, Q. X. Jia, and A. J. Taylor. Tuning the resonance in high-temperature superconducting terahertz metamaterials. *Phys. Rev. Lett.*, 105(24):247402, 2010.

[44] J. Wu, B. Jin, Y. Xue, C. Zhang, H. Dai, L. Zhang, C. Cao, L. Kang, W. Xu, J. Chen, and P. Wu. Tuning of superconducting niobium nitride terahertz metamaterials. *Opt. Express*, 19(13):12021–12026, 2011.

[45] C. Kurter, P. Tassin, A. P. Zhuravel, L. Zhang, T. Koschny, A. V. Ustinov, C. M. Soukoulis, and S. M. Anlage. Switching nonlinearity in a superconductor-enhanced metamaterial. *Appl. Phys. Lett.*, 100(12):121906–3, 2012.

[46] V. Savinov, V. A. Fedotov, S. M. Anlage, P. A. J. de Groot, and N. I. Zheludev. Modulating sub-THz radiation with current in superconducting metamaterial. *Phys. Rev. Lett.*, 109(24):243904, 2012.

[47] M. C. Ricci, H. Xu, R. Prozorov, A. P. Zhuravel, A. V. Ustinov, and S. M. Anlage. Tunability of superconducting metamaterials. *IEEE Trans. Appl. Supercond.*, 17(2):918–921, 2007.

[48] B. Jin, C. Zhang, S. Engelbrecht, A. Pimenov, J. Wu, Q. Xu, C. Cao, J. Chen, W. Xu, L. Kang, and P. Wu. Low loss and magnetic field-tunable superconducting terahertz metamaterial. *Opt. Express*, 18(16):17504–17509, 2010.

[49] A. P. Zhuravel, S. M. Anlage, and A. V. Ustinov. Microwave current imaging in passive HTS components by low-temperature laser scanning microscopy (LTLSM). *J. Supercond. Novel Magn.*, 19(7-8):625–632, 2006.

[50] A. P. Zhuravel, A. G. Sivakov, O. G. Turutanov, A. N. Omelyanchouk, S. M. Anlage, A. Lukashenko, A. V. Ustinov, and D. Abraimov. Laser scanning microscopy of HTS films and devices (review article). *Low Temp. Phys.*, 32(6):592–607, 2006.

[51] C. Kurter, A. P. Zhuravel, J. Abrahams, C. L. Bennett, A. V. Ustinov, and S. M. Anlage. Superconducting RF metamaterials made with magnetically active planar spirals. *IEEE Trans. Appl. Supercond.*, 21(3):709–712, 2011.

[52] C. Kurter, A. P. Zhuravel, A. V. Ustinov, and S. M. Anlage. Microscopic examination of hot spots giving rise to nonlinearity in superconducting resonators. *Phys. Rev. B*, 84(10):104515, 2011.

[53] A. P. Zhuravel, C. Kurter, A. V. Ustinov, and S. M. Anlage. Unconventional rf photoresponse from a superconducting spiral resonator. *Phys. Rev. B*, 85(13):134535, 2012.

[54] M. Tinkham. *Introduction to Superconductivity*. McGraw-Hill, New York, 2nd edition edition, 1996.

[55] T. P. Orlando and K. A. Delin. *Foundations of Applied Superconductivity*. Addison-Wesley, Reading, MA, 1991.

[56] K. K. Likharev. *Dynamics of Josephson Junctions and Circuits*. Gordon and Breach, New York, 1986.

[57] C. G. Du, H. Y. Chen, and S. Q. Li. Quantum left-handed metamaterial from superconducting quantum-interference devices. *Phys. Rev. B*, 74(11):113105, 2006.

[58] Andrei I. Maimistov and Ildar R. Gabitov. Nonlinear response of a thin metamaterial film containing josephson junctions. *Optics Communications*, 283(8):1633 – 1639, 2010.

[59] Philipp Jung. *Nonlinear Effects in Superconducting Quantum Interference Meta-atoms*. PhD thesis, Karlsruher Institut fr Technologie (KIT), http://www.ksp.kit.edu/download/1000043835, 10 2014.

[60] P. Jung, S. Butz, S. V. Shitov, and A. V. Ustinov. Low-loss tunable metamaterials using superconducting circuits with Josephson junctions. *Appl. Phys. Lett.*, 102(6):062601–4, 2013.

[61] S. Butz, P. Jung, L. V. Filippenko, V. P. Koshelets, and A. V. Ustinov. A one-dimensional tunable magnetic metamaterial. *Opt. Express*, 21(19):22540–22548, 2013.

[62] M. Trepanier, Daimeng Zhang, Oleg Mukhanov, and Steven M. Anlage. Realization and modeling of metamaterials made of rf superconducting quantum-interference devices. *Phys. Rev. X*, 3:041029, Dec 2013.

[63] P. Jung, M.and Fistul M. V.and Leppäkangas J. Butz, S.and Marthaler, V. P. Koshelets, and A. V. Ustinov. Multistability and switching in a superconducting metamaterial. *Nat. Comms.*, 5:4730, 2014.

[64] Daimeng Zhang, Melissa Trepanier, Oleg Mukhanov, and Steven M. Anlage. Tunable broadband transparency of macroscopic quantum superconducting metamaterials. *Phys. Rev. X*, 5:041045, Dec 2015.

[65] N. Lazarides and G. P. Tsironis. RF superconducting quantum interference device metamaterials. *Appl. Phys. Lett.*, 90(16):163501, 2007.

[66] N. Lazarides and G. P. Tsironis. Multistability and self-organization in disordered SQUID metamaterials. *Supercond. Sci. Technol.*, 26:084006, 2013.

[67] G.P. Tsironis, N. Lazarides, and I. Margaris. Wide-band tuneability, nonlinear transmission, and dynamic multistability in squid metamaterials. *Applied Physics A*, 117(2):579–588, 2014.

[68] Melissa Trepanier. *Tunable nonlinear superconducting metamaterials: Experiment and simulation*. PhD thesis, University of Maryland, College Park, http://drum.lib.umd.edu/handle/1903/17290, 2016.

[69] J. Hizanidis, N. Lazarides, and G. P. Tsironis. Chimeras in locally coupled SQUIDs: Lions, goats and snakes. http://arxiv.org/abs/1604.08160, 2016.

[70] O. A. Mukhanov, D. Kirichenko, I. V. Vernik, T. V. Filippov, A. Kirichenko, R. Webber, V. Dotsenko, A. Talalaevskii, J. C. Tang, A. Sahu, P. Shevchenko, R. Miller, S. B. Kaplan, S. Sarwana, and D. Gupta. Superconductor digital-RF receiver systems. *IEICE Trans. Electron.*, E91-C(3):306–317, 2008.

[71] O. Mukhanov, G. Prokopenko, and R. Romanofsky. Quantum sensitivity: Superconducting quantum interference filter-based microwave receivers. *IEEE Microwave Magazine*, 15(6):57–65, Sept 2014.

[72] José Carlos Pedro and Nuno Borges Carvalho. *Intermodulation distortion in microwave and wireless circuits*. Artech House, 2002.

[73] Z.Y. Shen. *High-temperature Superconducting Microwave Circuits*. Artech House Antennas and Propagation Library. Artech House, 1994.

[74] Muhammad Taher Abuelma'atti. Harmonic and intermodulation performance of Josephson junctions. *International Journal of Infrared and Millimeter Waves*, 14(6):1299–1310, 1993.

[75] Balam A. Willemsen, T. Dahm, and D. J. Scalapino. Microwave intermodulation in thin film high-T_c superconducting microstrip hairpin resonators: Experiment and theory. *Applied Physics Letters*, 71(26):3898–3900, 1997.

[76] T. Dahm and D. J. Scalapino. Intermodulation and quality factor of high-T_c superconducting microstrip structures. *Journal of Applied Physics*, 82(1):464–468, 1997.

[77] J. McDonald, J. R. Clem, and D. E. Oates. Critical-state model for intermodulation distortion in a superconducting microwave resonator. *Journal of Applied Physics*, 83(10):5307–5312, 1998.

[78] R. B. Hammond, E. R. Soares, Balam A. Willemsen, T. Dahm, D. J. Scalapino, and J. R. Schrieffer. Intrinsic limits on the Q and intermodulation of low power high temperature superconducting microstrip resonators. *Journal of Applied Physics*, 84(10):5662–5667, 1998.

[79] G. Benz, T. A. Scherer, M. Neuhaus, and W. Jutzi. Quality factor and intermodulation product of superconducting coplanar wave guides with slots in a DC magnetic field. *IEEE Transactions on Applied Superconductivity*, 9(2):3046–3049, June 1999.

[80] S. K. Remillard, Huai ren Yi, and A. Abdelmonem. Three-tone intermodulation distortion generated by superconducting bandpass filters. *IEEE Transactions on Applied Superconductivity*, 13(3):3797–3802, Sept 2003.

[81] J. Mateu, C. Collado, O. Menéndez, and J. M. O'Callaghan. A general approach for the calculation of intermodulation distortion in cavities with superconducting endplates. *Applied Physics Letters*, 82(1):97–99, 2003.

[82] J. Mateu, J. C. Booth, C. Collado, and J. M. O'Callaghan. Intermodulation distortion in coupled-resonator filters with nonuniformly distributed nonlinear properties - use in HTS IMD compensation. *IEEE Transactions on Microwave Theory and Techniques*, 55(4):616–624, April 2007.

[83] J. Mateu, C. Collado, N. Orloff, J. C. Booth, E. Rocas, A. Padilla, and J. M. O'Callaghan. Third-order intermodulation distortion and harmonic generation in mismatched weakly nonlinear transmission lines. *IEEE Transactions on Microwave Theory and Techniques*, 57(1):10–18, Jan 2009.

[84] E. Rocas, C. Collado, N. D. Orloff, J. Mateu, A. Padilla, J. M. O'Callaghan, and J. C. Booth. Passive intermodulation due to self-heating in printed transmission lines. *IEEE Transactions on Microwave Theory and Techniques*, 59(2):311–322, Feb 2011.

[85] Erik A. Tholén, Adem Ergül, David Schaeffer, and David B. Haviland. Gain, noise and intermodulation in a nonlinear superconducting resonator. *EPJ Quantum Technology*, 1(1):1–10, 2014.

[86] D. E. Oates and P. P. Nguyen. Microwave power dependence of yba[sub 2]cu[sub 3]o[sub 7] thin-film Josephson edge junctions. *Appl. Phys. Lett.*, 68(5):705–707, 2001.

[87] D. E. Oates, S. H. Park, M. A. Hein, P. J. Hirst, and R. G. Humphreys. Intermodulation distortion and third-harmonic generation in YBCO films of varying oxygen content. *IEEE Transactions on Applied Superconductivity*, 13(2):311–314, June 2003.

[88] A. P. Zhuravel, A. V. Ustinov, D. Abraimov, and S. M. Anlage. Imaging local sources of intermodulation in superconducting microwave devices. *IEEE Transactions on Applied Superconductivity*, 13(2):340–343, June 2003.

[89] H. Xin, D. E. Oates, G. Dresselhaus, and M. S. Dresselhaus. Third-order intermodulation distortion in $YBa_2Cu_3O_{7-\delta}$ grain boundaries. *Phys. Rev. B*, 65:214533, Jun 2002.

[90] Balam A. Willemsen, K. E. Kihlstrom, T. Dahm, D. J. Scalapino, B. Gowe, D. A. Bonn, and W. N. Hardy. Microwave loss and intermodulation in $Tl_2Ba_2CaCu_2O_y$ thin films. *Phys. Rev. B*, 58:6650–6654, Sep 1998.

[91] Ling Hao, J. Gallop, A. Purnell, L. Cohen, and S. Thiess. Non-linear microwave response of HTS thin films: a comparison of intermodulation and conventional measurements. *IEEE Transactions on Applied Superconductivity*, 11(1):3411–3414, Mar 2001.

[92] A V Velichko. Origin of the deviation of intermodulation distortion in high-T_c thin films from the classical 3:1 scaling. *Superconductor Science and Technology*, 17(1):1, 2004.

[93] D. E. Oates, S. H. Park, D. Agassi, G. Koren, and K. Irgmaier. Temperature dependence of intermodulation distortion in YBCO: understanding nonlinearity. *IEEE Transactions on Applied Superconductivity*, 15(2):3589–3595, June 2005.

[94] D. E. Oates, Y. D. Agassi, and B. H. Moeckly. Intermodulation distortion and nonlinearity in MgB_2: Experiment and theory. *IEEE Transactions on Applied Superconductivity*, 17(2):2871–2874, June 2007.

[95] H. W. Jang, K. J. Choi, C. M. Folkman, D. E. Oates, and C. B. Eom. Intermodulation distortion in epitaxial Y-Ba-Cu-O thick films and multilayers. *IEEE Transactions on Applied Superconductivity*, 19(3):2855–2858, June 2009.

[96] Y. D. Agassi, D. E. Oates, and B. H. Moeckly. Evidence for non-s-wave symmetry of the π gap in MgB_2 from intermodulation distortion measurements. *Phys. Rev. B*, 80:174522, Nov 2009.

[97] Evan K. Pease, Bradley J. Dober, and S. K. Remillard. Synchronous measurement of even and odd order intermodulation distortion at the resonant frequency of a superconducting resonator. *Review of Scientific Instruments*, 81(2), 2010.

[98] Y.D. Agassi and D.E. Oates. Intermodulation distortion and surface resistance in impurity-doped YBCO and MgB_2. *Physica C: Superconductivity and its Applications*, 506:119 – 132, 2014.

[99] B. Abdo, O. Suchoi, E. Segev, O. Shtempluck, M. Blencowe, and E. Buks. Intermodulation and parametric amplification in a superconducting stripline resonator integrated with a dc-SQUID. *EPL (Europhysics Letters)*, 85(6):68001, 2009.

[100] Baleegh Abdo, Eran Segev, Oleg Shtempluck, and Eyal Buks. Intermodulation gain in nonlinear NbN superconducting microwave resonators. *Applied Physics Letters*, 88(2), 2006.

[101] R. Vijay, M. H. Devoret, and I. Siddiqi. Invited review article: The josephson bifurcation amplifier. *Review of Scientific Instruments*, 80(11):–, 2009.

[102] O. Yaakobi, L. Friedland, C. Macklin, and I. Siddiqi. Parametric amplification in josephson junction embedded transmission lines. *Phys. Rev. B*, 87:144301, Apr 2013.

[103] T. Dahm and D. J. Scalapino. Theory of microwave intermodulation in a high-T_c superconducting microstrip resonator. *Applied Physics Letters*, 69(27):4248–4250, 1996.

[104] T. C. L. Gerhard Sollner, Jay P. Sage, and Daniel E. Oates. Microwave intermodulation products and excess critical current in $YBa_2Cu_3O_{7-x}$ Josephson junctions. *Applied Physics Letters*, 68(7):1003–1005, 1996.

[105] T. Dahm and D. J. Scalapino. Theory of intermodulation in a superconducting microstrip resonator. *Journal of Applied Physics*, 81(4):2002–2009, 1997.

[106] Balam A. Willemsen, K. E. Kihlstrom, and T. Dahm. Unusual power dependence of two-tone intermodulation in high-T_c superconducting microwave resonators. *Applied Physics Letters*, 74(5):753–755, 1999.

[107] T. Dahm, D. J. Scalapino, and B. A. Willemsen. Phenomenological theory of intermodulation in HTS resonators and filters. *Journal of Superconductivity*, 12(2):339–351, 1999.

[108] T. Dahm, D. J. Scalapino, and Balam A. Willemsen. Microwave intermodulation of a superconducting disk resonator. *Journal of Applied Physics*, 86(7):4055–4057, 1999.

[109] Wensheng Hu, A. S. Thanawalla, B. J. Feenstra, F. C. Wellstood, and Steven M. Anlage. Imaging of microwave intermodulation fields in a superconducting microstrip resonator. *Applied Physics Letters*, 75(18):2824–2826, 1999.

[110] E. A. Vopilkin, A. E. Parafin, and A. N. Reznik. Intermodulation in a microwave resonator with a high-temperature superconductor. *Technical Physics*, 45(2):214–220, 2000.

[111] Carsten Hutter, Daniel Platz, E. A. Tholén, T. H. Hansson, and D. B. Haviland. Reconstructing nonlinearities with intermodulation spectroscopy. *Phys. Rev. Lett.*, 104:050801, Feb 2010.

[112] R. K. Ritala and M. M. Salomaa. Chaotic dynamics of periodically driven rf superconducting quantum interference devices. *Phys. Rev. B*, 29:6143–6154, Jun 1984.

[113] M. Trepanier, Daimeng Zhang, Oleg Mukhanov, P. Jung, S. Butz, A. V. Ustinov, and Steven. M. Anlage. Meta-atom interactions and coherent response in superconducting macroscopic quantum metamaterials. manuscript in preparation.

[114] D. R. Smith and J. B. Pendry. Homogenization of metamaterials by field averaging. *J. Opt. Soc. Am. B*, 23(3):391–403, 2006.

[115] C. G. Du, H. Y. Chen, and S. Q. Li. Stable and bistable SQUID metamaterials. *J. Phys.: Condens. Matter*, 20(34):345220, 2008.

[116] Whiteley Research. http://www.wrcad.com/xic.html.

[117] Hypres Inc. http://www.hypres.com/foundry/niobium-process/#The+Niobium+Process.

[118] B. Chesca. Theory of RF SQUIDs operating in the presence of large thermal fluctations. *J. Low Temp. Phys.*, 110(516):963–1001, 1998.

[119] Ali A. Babaei Brojeny and John R. Clem. Magnetic-field and current-density distributions in thin-film superconducting rings and disks. *Phys. Rev. B*, 68:174514, Nov 2003.

[120] N. Bluzer and D. K. Fork. Inductance of a superconducting corbino ring. *IEEE Transactions on Magnetics*, 28(5):2051–2055, Sep 1992.

[121] Evonik Industries. www.rohacell.com.

[122] Coax Company Ltd. http://www.coax.co.jp.

[123] Lev S. Bishop, Eran Ginossar, and S. M. Girvin. Response of the strongly driven jaynes-cummings oscillator. *Phys. Rev. Lett.*, 105:100505, Sep 2010.

[124] O.A. Mukhanov. Energy-efficient single flux quantum technology. *IEEE Transactions on Applied Superconductivity*, 21(3):760–769, June 2011.

[125] L. D. Landau and E. M. Lifshitz. *Mechanics: Volume 1 (Course of Theoretical Physics S)*. Butterworth-Heinemann, 3rd edition, 1976.

[126] Daimeng Zhang, Melissa Trepanier, Thomas Antonsen, Edward Ott, and Steven M. Anlage. Intermodulation in nonlinear SQUID metamaterials: Experiment and theory. http://arxiv.org/abs/1606.09234, 2016.

[127] Whiteley Research. http://www.wrcad.com/.

[128] S. Doyle. Lumped element kinetic inductance detectors. *Ph.D. thesis, University of Cardiff, Cardiff, UK*, 2008.

[129] A. S. Averkin, A. P. Zhuravel, P. Jung, N. Maleeva, V. P. Koshelets, L. V. Filippenko, A. Karpov, and A. V. Ustinov. Imaging coherent response of superconducting metasurface. *IEEE Transactions on Applied Superconductivity*, 26(3):1–3, April 2016.

[130] Nanfang Yu and Federico Capasso. Flat optics with designer metasurfaces. *Nat. Mater.*, 13(2):139–150, 2014.

[131] Maryland NanoCenter Fablab. https://www.nanocenter.umd.edu/equipment/.

[132] Keysight Technologies. http://na.support.keysight.com/pna/help/latest/help.htm.

[133] Jen-Hao Yeh and Steven M. Anlage. In situ broadband cryogenic calibration for two-port superconducting microwave resonators. *Review of Scientific Instruments*, 84(3), 2013.

DAIMENG (DIAMOND) ZHANG

■ dmchang@umd.edu ■ https://www.linkedin.com/in/daimengzhang

EDUCATION

Ph.D. in Electrical and Computer Engineering (Advisor: Steven Anlage), 2011.08-2016.08
University of Maryland – College Park (UMCP), United States.

B. S. in Electronic Science & Technology, 2007.09-2011.06
Huazhong University of Science & Technology (HUST), Wuhan, China.

SELECTED AWARDS & HONORS

President of Women in Electrical and Computer Engineering (WECE), UMCP 2015 – 2016
The Clark School's Future Faculty Fellowship, UMCP 2014
PhD Fellowship of Electrical and Computer Engineering, UMCP 2011 – 2012
Best Undergraduate Research Achievement Award in Hubei Province, China (1 out of 1200) 2010 – 2011
Star of HUST Volunteer (0.5 %, for students contributing the most significantly to volunteer works) 2008 – 2009
National Scholarship (1%, the most honorable scholarship for Chinese Undergraduates) 2007-2008, 2008 – 2009

PUBLICATIONS

- Daimeng Zhang, M. Trepanier, Thomas Antonsen, Edward Ott, and Steven M. Anlage, *Intermodulation in Nonlinear SQUID Metamaterials: Experiment and Theory*, arXiv:1606.09234 (2016).
- Daimeng Zhang, M. Trepanier, Oleg Mukhanov, and Steven M. Anlage, *Tunable Broadband Transparency of Macroscopic Quantum Superconducting Metamaterials*, Phys. Rev. X. ***5,*** 041045 (2015).
  (**Press release**: Microwave Journal & http://cmns.umd.edu/news-events/features/3357)
- M. Trepanier*, Daimeng Zhang*, O. Mukhanov, and S. M. Anlage, *Realization and modeling of rf superconducting quantum interference device metamaterials*, Phys. Rev. X. ***3,*** 041029 (2013). (* Equal Contribution)
- D. Zhang, Z. Li, J. F. Zhong, L. Miao and J. J. Jiang, *Electronic properties of edge-functionalized zigzag graphene nanoribbons on SiO_2 substrate*, Nanotechnology ***22,*** 265702 (2011).

RESEARCH EXPERIENCES

Research Assistant, Anlage Research Lab, Physics Department, UMCP, USA 2012.05 – present
Advisor: Steven Anlage

Project Leader of a Nation Sponsored Innovation Program, HUST, Wuhan, China 2009.10 – 2011.05
Advisor: Daoli Zhang

Research Internship, Institute of Physics, Chinese Academy of Sciences, Beijing, China 2010.07–2010.08
Advisor: Hongjun Gao

Group Leader, project "Electronic Properties of GNRs on Substrate", HUST, Wuhan, China 2009.12–2010.12
Advisor: Ling Miao

RESEARCH HIGHLIGHTS

- **Intermodulation Generations (Two-Tone Responses) of RF SQUID Metamaterials:**
  D. Zhang, M. Trepanier, T. Antonsen, E. Ott, and S. M. Anlage, arXiv:1606.09234 (2016).

(1) We measure Intermodulation (IM) generation of a single RF-SQUID and arrays of RF-SQUIDs over a broad range of tone frequencies and tone powers. A unique sharp onset followed by a reduced IM region (gap) near the resonance is observed which differs from other nonlinear devices.
(2) We study the behaviors employing methods in nonlinear dynamics community. The sharp onset and the gap of IM are due to sudden state jumps during a beat of the two-tone sum input signal.
(3) The IM amplification is measured and analyzed. The ratio between two tone amplitudes modifies the multi-tone hysteresis behavior in RF SQUIDs.
(4) The IM can be manipulated with dc flux, tone powers, center frequencies, frequency difference between two tones, temperatures, and so on.

- **Tunable Broadband Transparency of Macroscopic Quantum Superconducting Metamaterials:**
  D. Zhang, M. Trepanier, O. Mukhanov, and S. M. Anlage, Phys. Rev. X. ***5,*** 041045 (2015).

(1) The SQUID metamaterial shows a nearly 100% disappearance of resonance absorption with manipulation of the drive amplitude, tiny amounts of dc magnetic field, and both magnetic and driving frequency history.
(2) The transparency is due to the intrinsic bi-stability of SQUIDs, and thus is self-induced, quite robust against disorder,

hysteretic, and switchable.

(3) Experiment, numerical simulation, and analytical solutions are in detailed agreement. The phenomenon can be understood in quantitative detail using the tools of nonlinear dynamics.

(4) This work introduces revolutionary new applications of metamaterials, such as self-induced power limiting, and the novel concept of a metamaterial that automatically reduces its scattering cross section to near zero (auto-cloaking). Co-author Oleg Mukhanov (Hypres Inc.) sees this metamaterial as an enabler for several new applications in low-dissipation computing and quantum computing.

- **Realization and Modeling of RF Superconducting Quantum Interference Device (RF SQUID) Metamaterials:**
  M. Trepanier*, D. Zhang*, O. Mukhanov, and S. M. Anlage, Phys. Rev. X. ***3,*** 041029 (2013). (* Equal Contribution)

(1) We have prepared meta-atoms based on radio-frequency superconducting quantum-interference devices (rf SQUIDs) and examined their tunability with dc magnetic field, rf current, and temperature.

(2) This work brings new physics to metamaterials research: it results from a combination of two macroscopic quantum effects into a single meta-atom: magnetic flux quantization and the Josephson effect.

(3) A dc magnetic field tunability of 80 THz/Gauss at 12 GHz is observed, a total tunability of 56% is achieved, enabling application such as a fast tunable digital filter.

(4) Excellent agreement between the data and a nonlinear dynamical model of SQUIDs.

- **Electronic properties of edge-functionalized zigzag graphene nanoribbons on SiO_2 substrate:**
  D. Zhang, Z. Li, J. F. Zhong, L. Miao and J. J. Jiang, Nanotechnology ***22,*** 265702 (2011)

(1) Based on first-principles calculations, electronic properties of edge-functionalized zigzag graphene nanoribbons (ZGNRs) on SiO2 substrate are presented. Metallic or semiconducting properties of ZGNRs are revealed due to various interactions between edge-hydrogenated ZGNRs and different SiO_2(0001) surfaces.

(2) Bivalent functional groups decorating ZGNRs serve as the bridge between active edges of ZGNRs and SiO2. These functional groups stabilize ZGNRs on the substrate, as well as modify the edge states of ZGNRs and further affect their electronic properties. Bandgaps are opened owing to edge state destruction and distorted lattice in ZGNRs.

CONFERENCE PRESENTATIONS

2016.03 APS March Meeting (Oral Presentation), Baltimore, MD,
"*Multi-tone response of Nonlinear rf-SQUID metamaterials*".

2015.03 APS March Meeting (Oral Presentation), San Antonio, TX,
"*Broadband Tunable Transparency in rf SQUID Metamaterial*".

2014.08 8th International Congress on Advanced Electromagnetic Materials in Microwaves and Optics – Metamaterials, Copenhagen, Denmark (Oral Presentation),
"*Extremely Nonlinear RF-SQUID Metamaterial*".

2014.05 Applied Superconductivity Conference (Poster Presentation), Charlotte, NC,
"*Time-Sensitive Dynamics of RF SQUID Metamaterials*".

2014.03 APS March Meeting (Oral Presentation), Denver, CO,
"*Extremely nonlinear and switchable SQUID metamaterial*".

2013.03 APS March Meeting (Oral Presentation), Baltimore, MD,
"*Measurement of a SQUID metamaterial*".

TEACHING EXPERIENCE

Co-Teacher, ENEE313 Introduction on Device Physics, UMCP 2015.09 – 2015.12

Lab Assistant, ENEE486 Optoelectronics Lab, UMCP 2011.09 – 2011.12